

Miniature Fiber-Optic Sensors for High-Temperature Harsh Environments

Yizheng Zhu

Dissertation submitted to the Faculty of
Virginia Polytechnic Institute and State University
In partial fulfillment of the requirements for the degree of

Doctor of Philosophy
in
Electrical Engineering

Dr. Anbo Wang, Chairman
Dr. Ira Jacobs
Dr. Gary R. Pickrell
Dr. James R. Heflin
Dr. Yong Xu

May 3rd, 2007
Blacksburg, Virginia

Keywords: fiber-optic sensor, pressure sensor, temperature sensor,
white-light interferometry, miniature.

Abstract

Dissertation title: Miniature Fiber-Optic Sensors for High-Temperature Harsh Environments

Yizheng Zhu

Measurement of physical parameters in harsh environments (high pressure, high temperature, highly corrosive, high electromagnetic interference) is often desired in a variety of areas, such as aerospace, automobile, energy, military systems, and industrial processes. Pressure and temperature are among the most important of these parameters. A typical example is pressure monitoring in jet engine compressors to help detect and control undesirable air flow instabilities, namely rotating stall and surge. However, the temperatures inside a compressor could reach beyond 600°C for today's large engines. Current fiber-optic sensor can operate up to about 300°C and even the most widely employed semiconductor sensors are limited below 500°C.

The objective of this research is to push the limit of fiber-optic sensing technology in harsh environment applications for both pressure and temperature measurements by developing novel sensing structures, fabrication techniques, and signal processing algorithms. An all-fused-silica pressure sensor has been demonstrated which is fabricated on the tip of a fiber with a diameter no larger than 125µm. The sensor was able to function beyond the current limit and operate into the 600~700 °C range. Also a temperature sensor has been developed using sapphire fibers and wafers for ultra-high temperature measurement as high as 1600 °C. This effort will generate more understanding regarding sapphire fiber's high temperature properties and could possibly lead to novel designs of pressure sensor for beyond 1000 °C. Both sensors have been field tested in real-world harsh environments and demonstrated to be reliably and robust.

In this dissertation, the design, fabrication, and testing of the sensors are discussed in detail. The system and signal processing techniques are presented. The plan and direction for future work are also suggested with an aim of further pushing the operating limit of fiber-optic sensors.

Acknowledgements

This entire work would not be possible without the constant support and encouragement from Dr. Anbo Wang, who offered me the career-changing opportunity to pursue my Ph.D. at Center for Photonics Technology (CPT) and helped me build up research skills and confidence over the course of six years through numerous productive and illuminating discussions on research, career and personal life. I would like to express my sincerest appreciation to him for all the advising and mentoring. He provides everyone at CPT sufficient freedom to pursue their own research interests and offers great flexibility as well to do so in their own style. Both students and CPT benefit so much under his leadership. I am also grateful to all the committee members, Dr. Ira Jacobs, Dr. Gary Pickrell, Dr. James Heflin, Dr. Yong Xu, for their unreserved help in this research.

There is a long list of former and current CPT students I would like to thank for their technical support in lab and friendship in life. In particular, my gratitude goes to Ming Han, Xiaopei Chen, Bo Dong, Fabian Shen, Zhengyu Huang, Juncheng Xu, Yan Zhang and Yongxin Wang. Work and life always became easier and more fun with them around, helping and sharing. I am especially indebted to Dr. Kristie Cooper, with whom I have been worked on a number of proposals and projects and gained invaluable experience, and Debbie Collins, our grants administrator, for her always timely and patient assistance with countless paperwork and projects.

Table of Contents

<i>CHAPTER 1</i>	Introduction.....	1
1.1	Scope.....	1
1.2	Pressure Sensors.....	3
1.3	Temperature Sensors.....	5
1.4	References.....	6
<i>CHAPTER 2</i>	Signal Processing in Spectral-Domain White-Light Interferometric Sensing Systems...	8
2.1	Principle of White-light Interferometry	8
2.2	Cavity Length Determination	11
2.2.1	Demodulation by Fringe Spacing	11
2.2.2	Demodulation by Fringe Tracing.....	13
2.3	Determination of Peak and Valley Positions	14
2.3.1	Centroid Algorithm.....	14
2.3.2	Curve Fitting	14
2.4	Other Techniques in Signal Processing	14
2.4.1	Noise Reduction and Digital Filtering	15
2.4.2	Sensor Multiplexing.....	15
2.4.3	Spectrum Normalization	17
2.5	References.....	18
<i>CHAPTER 3</i>	Ultra Miniature Fiber-Tip Pressure Sensor.....	20
3.1	Background in high-temperature fiber-optic pressure sensing	21
3.2	Sensor Fabrication	23
3.2.1	Fiber micro-machining Techniques	23
3.2.2	Fabrication Steps.....	26
3.3	Theoretical Analysis of Sensor Signals	32
3.3.1	Spectrum	32
3.3.2	Sensitivity	35
3.3.3	Dynamic Pressure Response	36
3.3.4	Size advantages.....	39
3.4	Laboratory Performance Test	41
3.4.1	Test Setup.....	41
3.4.2	Signal Demodulation	42
3.4.3	High Temperature Static Pressure Test Results.....	44
3.5	Dynamic Pressure Field Test	51
3.5.1	Self-calibrated interferometric intensity-based (SCIIB) system [10]	52
3.5.2	Sensor packaging	53
3.5.3	Test Result	55
3.6	Future work: Discussion and preliminary results	58

3.6.1	Temperature compensation:.....	58
3.6.2	Biomedical Application	65
3.7	Conclusion and Discussion.....	70
3.8	References.....	71
<i>CHAPTER 4</i> Sapphire-Wafer-Based Temperature Sensor.....		73
4.1	Background of high-temperature temperature sensing.....	74
4.2	Sensor Fabrication	75
4.2.1	Materials	75
4.2.2	Fabrication	76
4.2.3	Fusion splice	77
4.3	Interrogation System and signal processing	79
4.3.1	White-light based interrogation system	79
4.3.2	Signal Processing.....	79
4.4	Laboratory Test Results	82
4.5	First Field test results	83
4.5.1	System Design	84
4.5.2	Calibration.....	86
4.5.3	System Installation.....	88
4.5.4	Results.....	88
4.6	Surface-mount sapphire-wafer-based temperature sensor	89
4.7	Conclusion	94
4.8	References.....	94
<i>CHAPTER 5</i> Summary		96

List of Tables and Figures

Table 1-1. Current status of pressure and temperature sensing technologies	3
Figure 2-1. Typical schematic of white-light interferometric systems	9
Figure 2-2. White-light system consisting of a tunable laser source and a photodetector.....	10
Figure 2-3. Basic structure of Fabry-Perot interferometer.....	10
Figure 2-4. Spectrum of a pressure sensor multiplexed with a temperature sensor	16
Figure 2-5. Fast Fourier Transform (FFT) of the multiplexed spectrum.....	16
Figure 3-1. Conventional structure of a fiber-optic pressure sensor.....	21
Figure 3-2. (a) SM-SM splicing; (b) SM-MM splicing	23
Figure 3-3. (a) SM-Capillary tube splicing under special condition; (b) Under regular condition	24
Figure 3-4. (a) Cleaved fiber; (b) Precision cleaving; (c) Cleaving under microscope	25
Figure 3-5. MM fibers etched in 50% HF for 5 minutes.	26
Figure 3-6. Fiber tip sensor etch barrier layer.....	27
Figure 3-7. Fiber tip sensor cavity formation process	27
Figure 3-8. Fiber tip sensor diaphragm fabrication process	28
Figure 3-9. Sensor fabrication process.....	29
Figure 3-10. Cavity generation	29
Figure 3-11. Diaphragm fabrication	30
Figure 3-12. Photos. (a) Cavity edge; (b) Cavity bottom; (c) Diaphragm.....	31
Figure 3-13. Tip sensor as compared to a dime	31
Figure 3-14. Using capillary tube for cavity fabrication.....	32
Figure 3-15. Photolithography processes for pit fabrication	32
Figure 3-16. Reflections in a miniature tip sensor.....	33
Figure 3-17. Output spectrum of sensor 1 at room temperature and pressure.....	35
Figure 3-18. Theoretical sensitivity for the sensor.	36
Figure 3-19. A single degree-of-freedom vibration system.....	37
Figure 3-20. Frequency response of the diaphragm.....	38
Figure 3-21. System setup for high-temperature static pressure test.....	41
Figure 3-22. Sensor spectra at 13.7, 40, 70, and 100psi	42
Figure 3-23. Cavity length simulation: actual value L vs. calculated value L _{calc}	43
Figure 3-24. Sensor 1 testing results at different temperatures.	45
Figure 3-25. Sensor 2 testing results at different temperatures.	45
Figure 3-26. Sensitivity vs. temperature.....	46
Figure 3-27. System resolution test.....	46
Figure 3-28. Relative repeatability of the sensors at different temperatures.....	48
Figure 3-29. Creep of sensor 1 at constant pressure and temperature.....	48
Figure 3-30. Airgap vs. temperature for both sensors.....	51

Figure 3-31. Schematic diagram of the SCIIB system (left); simulated wideband and narrowband signals (right).	53
Figure 3-32. Schematic (top) and photo (bottom) of sensor packaging	54
Figure 3-33. Photos of engine with sensors mounted	55
Figure 3-34. Sensor packaging on the side wall	55
Figure 3-35. Mini-sensor output vs. Kulite sensor output. (top) Time domain signal; (bottom) FFT spectrum	56
Table 3-1. Frequencies and amplitudes of output harmonics	57
Figure 3-36. Scheme of sensor multiplexing	59
Figure 3-37. Spectra of temperature sensors sT1 and sT2	61
Figure 3-38. Spectrum of pressure sensor sP	61
Figure 3-39. High reflection T sensor + P sensor	62
Figure 3-40. Low reflection sT2 + sP	62
Figure 3-41. FFT of high reflection T + P	63
Figure 3-42. FFT of low reflection T + P	63
Figure 3-43. Spectra of temperature sensors	64
Figure 3-44. Spectrum of pressure sensor	64
Figure 3-45. Insertion of fiber pressure sensor through a 24 gauge intravenous catheter (left); close-up of fiber protruding from catheter tip (right).	67
Figure 3-46. Sensor signal with and without a Ti coating, full spectrum (left); spectral range of interest (right)	70
Figure 4-1. Wafer-based interferometric sensing structure	75
Figure 4-2. Sensor head structure	76
Figure 4-3. Fusion splice between silica fiber and sapphire fiber	77
Figure 4-4. Reflected power vs. number of arcs	78
Figure 4-5. Schematic of the sensor and the system	79
Figure 4-6. Sensor spectrum at different temperature	80
Figure 4-7. FFT of spectrum	81
Figure 4-8. Optical thickness vs. temperature for three tests	82
Figure 4-9. Temperature difference between sensor and thermocouple	83
Figure 4-10. Design of coal gasifier temperature monitoring system	84
Figure 4-11. Schematic of sensing probe design	85
Figure 4-12. Probe mounting position	86
Figure 4-13. Left: photo of sensors; Right: sensor test setup	86
Figure 4-14. Temperature responses (left) and normalized temperature response (right)	87
Figure 4-15. Installed probe and housing (left); optical interrogators (middle); and signal processing unit (right).	88
Figure 4-16. 72-day temperature results	89
Figure 4-17. Sensor head structure	89
Figure 4-18. Sensor spectrum	90
Figure 4-19. Temperature response	91
Figure 4-20. Sensor resolution at room temperature	94

CHAPTER 1

Introduction

The field of fiber optic sensing has seen rapid growth in the past three decades since its first developments in the mid 1970s[1][2]. Its principles and applications are extremely diversified, with numerous mechanisms demonstrated for the measurement of a variety of physical parameters, such as temperature, pressure, strain, electromagnetic (EM) field, flow, vibration, and chemicals. It has also become attractive for biomedical and biochemical detection. Fiber optic sensors are well known for their intrinsic immunity to EM interference, electrical passivity, high resolution and large dynamic range, and play important role where electronic/semiconductor sensors cannot apply, such as electrical hostile, high temperature or highly corrosive environments.

1.1 Scope

Temperature and pressure sensing for these harsh environments has long been one of the focuses in fiber optic sensing, and also the subject of this dissertation. Specifically, the research objective is to push the limit of fiber-optic sensing technology for temperature and pressure measurement in harsh environments by developing novel sensing structures, fabrication techniques and signal processing algorithms, to offer sensing capability far beyond current technologies.

The selection of sensing materials is essential as the capability and limitation of a fiber-optic sensor are often determined by the materials it involves. A variety of sensing materials are

available, including fused silica, which the majority of fibers are made of, silicon, doped glasses, polymers, silicon carbide (SiC), and some crystals. The first selection requirement is obvious, namely all materials should be able to survive high-temperature and retain reasonably good optical and mechanical properties. The second criterion is based on the fact that sensors constructed out of uniform materials have better survivability and reliability over large temperature range, than those made of a combination of materials which often suffer from thermal expansion mismatch, severely comprising sensors' high-temperature performance, especially for those which contain hermetically sealed structures. Therefore materials chosen for the sensors are necessarily to have close thermal properties or in ideal case to be uniform. Given this, and the fact that the material has to be available in fiber, fused silica and sapphire (Al_2O_3 , single crystal alumina) are then decided the materials of choice for the high-temperature application.

Both materials have excellent optical, thermal and mechanical properties even at elevated temperatures. The major difference is that fused silica fibers operates only to about 1000 °C due to dopant diffusion and degraded mechanical properties[3], while crystalline sapphire can survive far beyond that threshold and hence receives great attentions for ultra-high temperature environments. In fact, the majority of the already proposed fiber-optic temperature and pressure sensors for high-temperature environments are based on these two materials.

Table 1-1 lists the current status of the development of pressure and temperature sensors, roughly divided into two categories by 1000 °C. Below that are high-temperature applications involving mostly silica-fiber-based sensors. Beyond that are ultra-high temperature applications, mostly dominated by single crystal materials such as sapphire. Sensors are therefore categorized into four group based on these two dimensions, temperature and function.

Apparently sensors for ultra-high temperature are more complicated to design than those for relatively low temperature use. In the dimension of functions, it is generally true that the development of pressure sensors presents more difficulties than temperature sensors, because the

former category often rely on structural deformation for detection and hence impose strict requirements on materials' mechanical properties. This is particularly critical in high-temperature. In Table 1-1, red/yellow/green texts indicate high/medium/low difficulty in sensor design. Except for silica-fiber-based temperature sensing where numerous structures have been proposed (Category 1), the other three categories are relatively much less developed. Current fiber-optic pressure sensors are able to operate only to 200~300 °C, and only very few technologies have been demonstrated for temperature sensing beyond 1000 °C.

The research started with silica-based pressure sensor to push the limit of current technology (Category 2), then move on to sapphire-fiber-based temperature sensors (Category 3), and based on these initial efforts, look for potentials to design sensing structures for ultra-high-temperature pressure measurement (Category 4).

In the following two sections, we will look in more detail at the current state of art of pressure and temperature sensing technologies for high-temperature applications.

Table 1-1. Current status of pressure and temperature sensing technologies

	Temperature	Pressure
Ultra-high T > 1000 °C (Sapphire)	3 A few technologies demonstrated	4 No technology available
High T < 1000 °C (Silica)	1 Well developed	2 No technology available
		Current sensors < 300 °C

1.2 Pressure Sensors

High-temperature pressure sensing is highly desired in industries such as automotive and aerospace. For example, in a jet engine, pressure measurements inside the compressor would

greatly help to detect and control surge and stall to improve performance and efficiency. However, the temperature there can reach as high as 600°C for today's large engines. Such harsh environment applications impose great challenges on both the design and materials of the sensors and packaging, and generate a rising need for high-temperature pressure sensors.

Traditional semiconductor pressure sensors are usually limited to below 150°C if used without extra cooling mechanism. These sensors are micromachined on a silicon diaphragm with piezoresistors diffused into them, and would fail at high temperature due to increased p-n junction leakage. Improved version uses silicon on insulator (SOI) structures to isolate the piezoresistors from the silicon diaphragm by a layer of silicon dioxide and is functional up to about 500°C when silicon starts to creep[4][5].

Other high-temperature materials have also been explored to build pressure sensors, nearly all of which inherit the diaphragm-based design and employ either piezoresistive or capacitive detection. Among these materials, silicon carbide (SiC) has received more attention as a long-recognized high-temperature semiconductor material for micro-electro- mechanical systems (MEMS). Okojie *et. al.* proposed a α (6H)-SiC pressure sensor functional up to 500°C[5]. Berg *et. al.* demonstrated the operation of a β -SiC pressure sensor in a combustion engine to about 300°C[6]. Du *et. al.* reported 400°C test results of a capacitive sensor using β -SiC diaphragm as well. Ceramic[7], sapphire[8], and diamond[9] materials also have the potentials for high-temperature pressure sensing.

Compared to these electronic sensors, fiber-optic sensors are known for their immunity to electromagnetic interference (EMI), electrical passivity, high resolution and high accuracy. Fiber-optic pressure sensors employing various techniques have been investigated extensively, yet very few of them have been designed for high-temperature operation. Pulliam *et. al.* proposed a SiC diaphragm-based interferometric pressure sensor promising to operate at high temperatures[10]. The key factor limiting fiber-optic pressure sensors' high-temperature capability is that their sensor head assemblies usually involve various materials other than fibers'

fused silica, including silicon, low softening point glass (e.g. pyrex), polymer, epoxy or other adhesives. The thermal expansion mismatch between these materials can cause stress and degrade the structure's mechanical strength and stability at elevated temperatures. In addition, the common use of low temperature materials (especially polymers and adhesives) will significantly affect the sensors' accuracy and repeatability.

Since fiber is made of fused silica which is an excellent optical material with high softening point, a fiber sensor constructed completely using fused silica would have great potential to operate at high temperatures. However, the high softening point also makes fused silica difficult to bond, especially when hermetic sealing is required for pressure sensing. In Chapter 3, we introduce the design and fabrication of an all-fused-silica sensor which overcomes this bonding difficulty. Detailed laboratory experiments demonstrated its high-temperature capability. Its reliability and robustness were further verified in a jet engine field test at Virginia Tech.

1.3 Temperature Sensors

While silica-fiber-based temperature sensors usually cannot exceed 1000°C[3], single-crystal optical fibers have received extensive attention, owing to their compact structures and excellent mechanical and optical properties at elevated temperature. Radiation-based temperature sensors using sapphire fibers as a lightpipe to collect and transmit blackbody radiation have long been developed [11][12] and are currently the choice of sensor in semiconductor industries for monitoring of rapid thermal processing. Tong *et al.* demonstrated the operation of such a sensor up to 2300°C using zirconia single-crystal fiber[13]. In fluorescence-based sensors, a doped fiber is excited by a pulsed laser to generate fluorescence whose decay time is temperature-dependent and used as the measurand. The use of silica fibers limits most sensors of this type to relatively low temperature. Kennedy and Djeu reported a maximum operating temperature of 1600°C by a Yb-doped single crystal YAG optical fiber[14]. Fiber-optic Fabry-Perot (FP) interferometric sensors have the advantages of high accuracy, high resolution and simple configuration. Various

principles based on this structure have been demonstrated for high-temperature sensing. Wang *et al.* proposed both intrinsic[3][15] and extrinsic[16] FP temperature sensors using sapphire fiber. In Chapter 4, we introduce a sapphire-fiber-based interferometric sensor which is easy to fabricate and ranks as one of the smallest temperature sensors available. Laboratory results demonstrated its excellent temperature response and repeatability. Over the past two years, two field test efforts were carried out in collaboration with Tampa Electric Corp. (TECO). A complete sensing system, including sensor probe, optical interrogator, and digital signal processing unit, was installed in TECO's Polk Power Station in Florida. Two probes, one original and another improved version, were installed in the plant's 250-megawatt coal gasifier. Details are presented in Chapter 4.

Chapter 5 introduces the design, fabrication and tests of an improved sapphire-fiber temperature sensor. The characterization of this sensor could provide insight into the development of other high-temperature sensing structure such as strain and pressure.

1.4 References

- [1] V. Vali, and R. W. Shorthill, "Fiber ring interferometers," *Appl. Opt.*, vol. 15, 1099, 1976.
- [2] A. J. Rogers, "Optical methods for measurement of voltage and current at high voltage," *Opt. Laser Technol.*, 273, 1977.
- [3] A. Wang, S. Gollapudi, K. A. Murphey, R. G. May, and R. O. Claus, "Sapphire-fiber-based intrinsic Fabry-Perot interferometer," *Opt. Lett.*, **17**, 1021-1223 (1992)
- [4] A. D. Kurtz, A. A. Ned, S. Goodman, and A. H. Epstein, "Latest ruggedized high temperature piezoresistive transducers," presented at the NASA 2003 Propulsion Measurement Sensor Development Workshop, Huntsville, Alabama, May 13-15, 2003.
- [5] R. S. Okojie, A. A. Ned, and A. D. Kurtz, "Operation of $\alpha(6H)$ -SiC pressure sensor at 500°C," *Sens. Actuators A*, vol. 66, no. 1-3, pp. 200-204, 1998.
- [6] J. von Berg, R. Ziermann, W. Reichert, E. Obermeier, M. Eickhoff, G. Krotz, U. Thoma, C. Cavalloni, and J. P. Nendza, "Measurement of the cylinder pressure in combustion engines

- with a piezoresistive β -SiC-on-SOI pressure sensor,” in *Proc. High Temperature Electronics Conference*, Albuquerque, NM, 1998, pp. 245-249.
- [7] M. A. Fonseca, J. M. English, M. von Arx, and M. G. Allen, “Wireless micromachined ceramic pressure sensor for high-temperature application,” *J. Microelectromechanical Syst.*, vol. 11, no. 4, pp. 337-343, 2002.
- [8] M. Soeda, T. Kataoka, Y. Ishikura, S. Kimura, T. Masuda, Y. Yoshikawa, and M. Nagata, “Sapphire-based capacitive pressure sensor for high temperature and harsh environment application,” in *Proc. of IEEE Sensors*, 2002, vol. 2, pp. 950-953.
- [9] K. C. Holmes, J. L. Davidson, W. P. Kang, and A. L. Sternberg, “Diamond microelectromechanical sensors for pressure and accelerating sensing,” in *Proc. Microelectromechanical Systems Conference*, 2001, pp. 45-49.
- [10] W. Pulliam, P. Russler, R. Mlcak, K. Murphy, and C. Kozikowski, “Micromachined, SiC fiber optic pressure sensors for high-temperature aerospace applications,” in *Proc. SPIE Industrial Sensing Systems*, 2000, pp. 21-30.
- [11] R. R. Dils, “High-temperature optical fiber thermometer,” *J. Appl. Phys.*, **54**, 1198-1201 (1983)
- [12] R. R. Dils, J. Geist, and M. L. Reilly, “Measurement of the silver freezing point with an optical fiber thermometer: Proof of concept,” *J. Appl. Phys.*, **59**, 1005-1012 (1986)
- [13] L. Tong, Y. Shen, L. Ye, and Z. Ding, “A zirconia single-crystal fiber-optic sensor for contact measurement of temperatures above 2000°C,” *Meas. Sci. Technol.* **10**, 607-611 (1999)
- [14] J. L. Kennedy, and N. Djeu, “Operation of Yb:YAG fiber-optic temperature sensor up to 1600°C,” *Sensors Actuators A* **100**, 1870191 (2002)
- [15] A. Wang, S. Gollapudi, R. G. May, K. A. Murphey, and R. O. Claus, “Advances in sapphire-fiber-based intrinsic interferometric sensors,” *Opt. Lett.* **17**, 1544-1546 (1992)
- [16] A. Wang, S. Gollapudi, R. G. May, K. A. Murphey, and R. O. Claus, “Sapphire optical fiber-based interferometer for high temperature environmental applications,” *Smart Mater. Struct.* **4**, 147-151 (1995)

CHAPTER 2

Signal Processing in Spectral-Domain White-Light Interferometric Sensing Systems

Interferometric sensors constitute one major category in fiber-optic sensors with high resolution and large dynamic range [1]. These sensors are various types of interferometers which generate multiple beams of light to interference with each other. A variety of interrogating systems have been proposed, some of which used semiconductor fiber lasers as the light source. Many others employed low coherent, broadband sources, such as light emitting diode (LED), halogen lamp, multimode fiber laser, or tunable single-mode fiber laser, and commonly referred to as white-light interferometry. In this chapter, we introduce the principles of white-light interferometry and specifically focus on the spectral-domain interferometric systems, which have received great attentions and proven to be very effective in the past ten years, and was adopted for this research. Also discussed are the basic white-light signal processing and newly developed algorithms.

2.1 Principle of White-light Interferometry

A typical white-light interferometric system is shown in Figure 2-1.

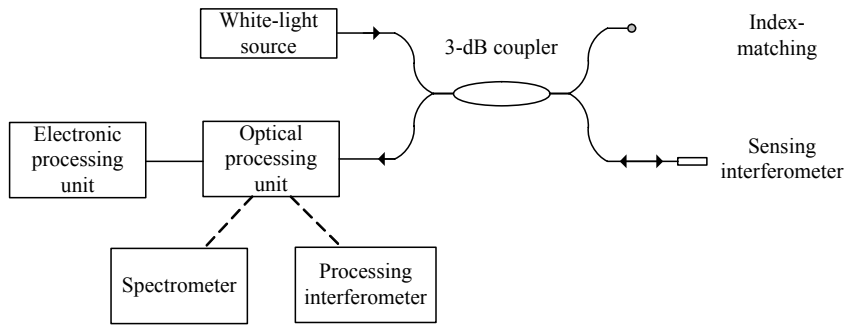


Figure 2-1. Typical schematic of white-light interferometric systems

Light emitted from a broadband source travels through a 3-dB directional coupler to the sensing interferometer, which senses the environmental physical changes, encodes the information into the incoming light by modifying its properties (e.g. intensity, spectrum, phase, polarization, etc), and reflects it back to the processing unit for detection. Another end of the coupler is index-matched to reduce reflection.

Two types of optical processing units are commonly seen. One is a second interferometer to demodulate the change of the sensing interferometer. Many systems based on this configuration have been proposed for measurement of displacement, temperature, pressure, vibration, etc. Another more straightforward processing is to use a spectrometer to retrieve the spectrum of the reflected broadband light. Direct spectral analysis can then resolve the environmental physical change. Although in the early years of fiber-optic sensor development the former method received greater attention because of the relatively low cost, the additional processing unit makes the system more complicated and less accurate. With the emergence of low-cost miniature spectrometers, the latter approach is receiving more attentions and shown to be very effective, accurate, and robust, particular promising for real-world industrial applications. Since this Ph.D. research is based on the spectrometer-based system, we will only be discussing this second technique and its related issues.

Besides the combination of white-light source and spectrometer, another equivalent system employs a tunable laser source and a photodetector (PD) for spectrum capture, as shown in Figure 2-2.

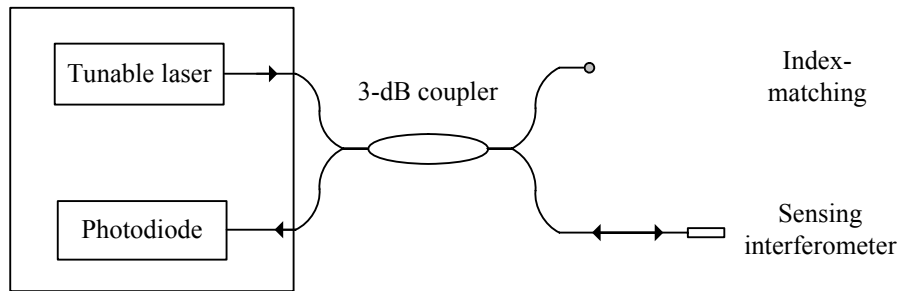


Figure 2-2. White-light system consisting of a tunable laser source and a photodetector.

The tunable laser and the PD can be either separate components with synchronization interface in between, or integrated together as a single piece of instrument, functioning essentially as a spectrometer with broadband source. One of our white-light systems, Micron Optics' si720 Component Testing System (CTS), is such an instrument and a powerful experimental tool in Chapter 3.

As mentioned earlier, the spectrum is comprised of interference signal from the sensing interferometer, which could be of Michelson, Mach-Zehnder (MZ), or Fabry-Perot (FP) type. The FP interferometer (FPI) is the choice for our sensor development because of its simplicity and compactness.

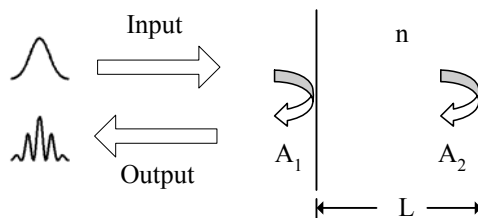


Figure 2-3. Basic structure of Fabry-Perot interferometer

A basic FPI is shown in Figure 2-3, comprising two reflective surfaces separated by a cavity of length L and refractive index n . For low-finesse (usually low surface reflection) FPI which is the case for most sensors, input light generates two reflections at the two surfaces with amplitudes of A_1 and A_2 , respectively, which will interfere with each other to produce a total reflected light intensity as the following.

$$\begin{aligned}
 I(\lambda) &= \left| A_1 + A_2 \exp\left(-j \cdot 2\pi \cdot \frac{2nL}{\lambda}\right) \right|^2 \\
 &= A_1^2 + A_2^2 + 2A_1A_2 \cos\left(\frac{4\pi nL}{\lambda}\right)
 \end{aligned} \tag{2-1}$$

It is clear that the reflected sensor spectrum is modulated by the FP cavity as a cosine function. When the two reflections are in-phase, they will add to each other to produce an interfering maxima (peak), or otherwise, an interfering minima (valley).

The change in environmental parameter, such as pressure and temperature variation, will modify the cavity length L and in turn affect $I(\lambda)$. Therefore by analyzing $I(\lambda)$ to demodulate L , these environmental changes could be obtained. This is the basic principle of spectral-domain white-light interferometry for Fabry-Perot sensors.

2.2 Cavity Length Determination

How to determine cavity length L accurately is essential to the system performance. In this section, two algorithms are discussed, namely, fringe-spacing demodulation and fringe-tracing demodulation.

2.2.1 Demodulation by Fringe Spacing

Equation (2-1) shows that the spectrum of a FPI is periodic. Therefore the cavity length L can be determined from its period, often calculated by the distance between adjacent peaks and/or

valleys[2]. For example, let λ_1 and λ_2 denote the positions of adjacent peaks #1 and #2, and they should satisfy the following in-phase condition

$$\frac{4\pi nL}{\lambda_1} = 2\pi \cdot N \quad \text{and} \quad \frac{4\pi nL}{\lambda_2} = 2\pi \cdot (N-1) \quad (2-2)$$

where N is the fringe order for peak #1. Removing N by subtraction, we have

$$\frac{2nL}{\lambda_1} - \frac{2nL}{\lambda_2} = 1 \quad \Rightarrow \quad L = \frac{\lambda_2 \lambda_1}{2n(\lambda_2 - \lambda_1)} \quad (2-3)$$

Apparently, this technique is to calculate the phase difference between two specific spectral points, in this case, two adjacent peaks. Therefore it is a relative phase demodulation.

Now we analyze the error performance of this method. By taking differential of Eq. (2-3), we have

$$\begin{aligned} \Delta L &= \frac{\lambda_2^2}{2n(\lambda_2 - \lambda_1)^2} \Delta \lambda_1 - \frac{\lambda_1^2}{2n(\lambda_2 - \lambda_1)^2} \Delta \lambda_2 \\ &\approx \frac{\lambda_1 \lambda_2}{2n(\lambda_2 - \lambda_1)^2} (\Delta \lambda_1 - \Delta \lambda_2) \\ &= \frac{L}{(\lambda_2 - \lambda_1)} (\Delta \lambda_1 - \Delta \lambda_2) \end{aligned} \quad (2-4)$$

or

$$\frac{\Delta L}{L} \approx \frac{\Delta \lambda_1 - \Delta \lambda_2}{\lambda_2 - \lambda_1} \quad (2-5)$$

where the approximation is made because λ_1 and λ_2 are usually close and approximately equal. It is also reasonable to assume that $\Delta \lambda_1$ and $\Delta \lambda_2$, the errors in determining the peak positions, are independent and the same, denoted as $\Delta \lambda$. Then Eq. (2-5) becomes

$$\frac{\Delta L}{L} = \sqrt{2} \frac{\Delta \lambda}{\lambda_2 - \lambda_1} \quad (2-6)$$

It is clear that the relative error in determining L is inversely proportional to the spacing between λ_1 and λ_2 , or the period of the spectrum.

2.2.2 Demodulation by Fringe Tracing

Rather than calculating the relative phase difference as in the previous section, this method uses the absolute phase information to determine L [3], as Eq. (2-2) can be directly transformed into

$$L = \frac{N}{2n} \lambda_1 \quad (2-7)$$

This only requires the knowledge about the position of one peak or one valley and its fringe order, instead of a second position. N can be pre-determined from the spectrum and kept fixed throughout experiment, meaning that a specific peak or valley is monitored and giving the name “fringe-tracing”.

As compared to the previous one, the advantage of this method is its higher resolution. Its relative error $\Delta L/L$ is simply

$$\frac{\Delta L}{L} = \frac{\Delta \lambda}{\lambda_1} \quad (2-8)$$

Compared with Eq. (2-6), the gain of the resolution is

$$\eta = \frac{(\Delta L / L)_{rel}}{(\Delta L / L)_{abs}} = \frac{\sqrt{2} \lambda_1}{(\lambda_1 - \lambda_2)} \quad (2-9)$$

For example, assume $n = 1$, $L = 20\mu\text{m}$, there will be peaks at 800.0 nm and 816.3 nm in a near infra-red (NIR) spectrometer for $N = 50$ and 51. And η approximately equals to 70. The Center

for Photonics Technology (CPT) has been developing this technique for years. Excellent accuracy and resolution have been demonstrated in both laboratory and field tests.

2.3 Determination of Peak and Valley Positions

Both demodulating methods require accurate determination of peak and/or valley positions. Centroid algorithm was widely applied in temporal-domain white-light systems for central fringe identification [4], and also proven very effective in spectral-domain systems [5].

2.3.1 Centroid Algorithm

Around a peak or a valley, all data points have information about its position, not only the maximum or minimum point. Usually the closer the value of a data point to the maximum or the minimum, the closer its position to the peak or valley position. Therefore its value, to some extent, stands for the possibility of its position being the peak or valley position. By taking the weighted average of these data points, i.e., calculating the centroid, the peak/valley position can be obtained as the following:

$$\lambda_{peak/valley} = \frac{\sum I_i \lambda_i}{\sum I_i} \quad (2-10)$$

where λ_i and I_i are the position and intensity of the i th pixel, respectively. The centroid algorithm is relatively simple but computationally very effective.

2.3.2 Curve Fitting

In this research, we adopt another effective approach, namely parabolic fitting, as all of these peaks and valleys are symmetric and can be approximated by a parabolic for points local to the peaks or valleys.

2.4 Other Techniques in Signal Processing

The original sensor spectrum retrieved from spectrometer is usually noisy and not an ideal cosine function for systems employing LED as light source. Before applying either centroid or parabolic fit algorithms, a series of other processing may have to be taken. As today's personal computers are getting increasingly powerful, techniques which used to be computationally prohibitive, such as digital filtering, can now be implemented very fast.

2.4.1 Noise Reduction and Digital Filtering

Although both centroid and parabolic fitting algorithms have high noise tolerance, additional noise suppression is still necessary to further improve resolution. Boxcar smoothing is simple to use but limited to small averaging window when processing high density fringes, where the number of pixels within each fringe is reduced and large window could smooth the entire fringes out. Therefore its noise-reduction performance is quite limited. In our research, digital filters are instead used to get cleaner signal by removing the noise outside the signal band.

2.4.2 Sensor Multiplexing

Digital filtering is also useful to separate spectra of multiplexed sensor. Figure 2-4 shows the example of a multiplexed spectrum of a pressure sensor and a temperature sensor, acquired by si720 CTS. The fabrication of the pressure sensor will be described in Chapter 3, which also briefly introduces its multiplex with the temperature sensor.

In Figure 2-4, the slowly-varying profile is the interference from the short-cavity ($\sim 30 \mu\text{m}$) pressure sensor while the ripple on it is caused by the temperature sensor which has a much longer cavity length of about $750 \mu\text{m}$. As shown in Figure 2-5, the two sensors are clearly separated on the fast Fourier transform (FFT) and filtering can extract each signal conveniently.

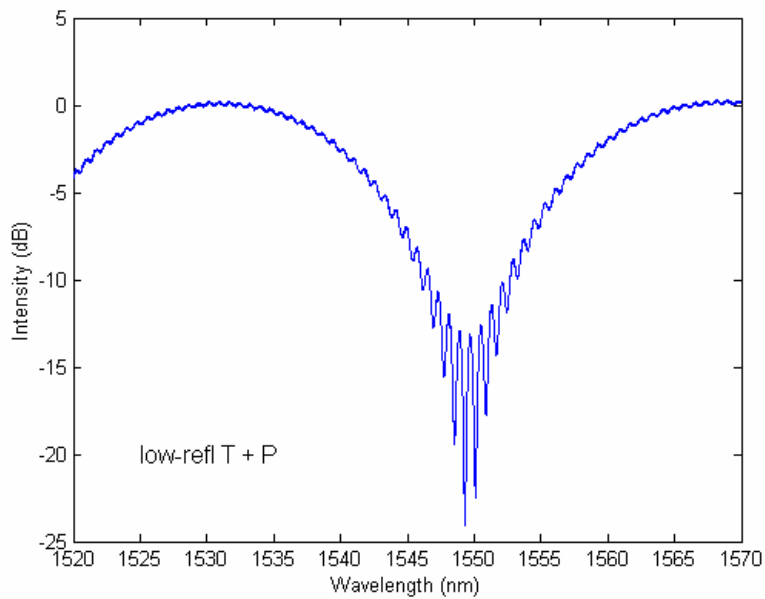


Figure 2-4. Spectrum of a pressure sensor multiplexed with a temperature sensor

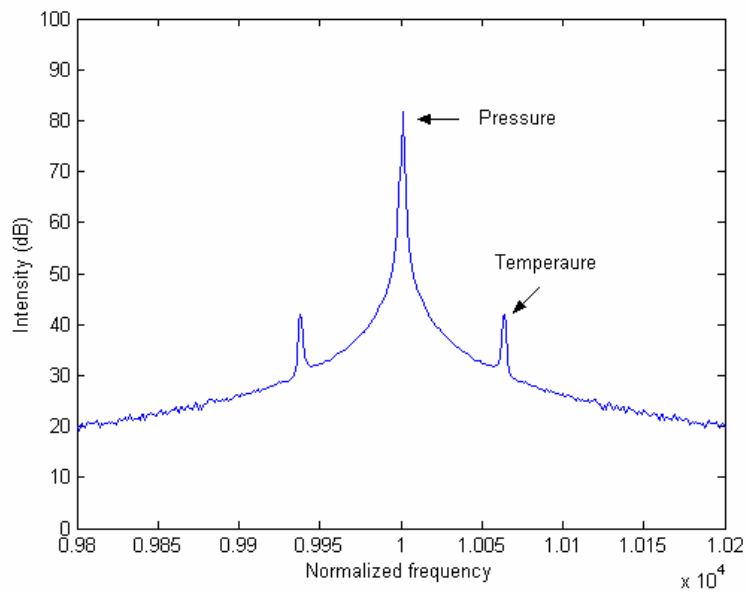


Figure 2-5. Fast Fourier Transform (FFT) of the multiplexed spectrum

2.4.3 Spectrum Normalization

CTS has a built-in tunable laser source and automatically compensates for its power variation at different wavelengths, leaving no need to normalize the spectrum in Figure 2-4 and 2-5.

However, a majority of white-light systems employ light emitting diode (LED) as light source. The resulting sensor spectrum will bear the profile of the LED, which, however, needs to be removed (normalization) before other algorithms can be applied to calculate cavity length. Such a spectrum can be written as

$$I(\lambda) = I_{LED}(\lambda) \left[A_1^2 + A_2^2 + 2A_1A_2 \cos\left(\frac{4\pi nL}{\lambda}\right) \right] \quad (2-11)$$

One simple approach is to save the LED spectrum beforehand and use it to normalize the sensor spectrum later. An immediate problem would result from the source drift, which will affect the sensor's repeatability and accuracy.

Although for short-cavity FPI sensors this remains as the best approach, a new processing algorithm has been developed in this research which can apply to long-cavity (dense fringes) sensors with better performance.

Since the long-cavity sensing signal is usually at higher frequency compared to the slowly-varying source profile $I_{LED}(\lambda)$, it can be extracted by filtering, similar to the sensor multiplexing in the previous section, leaving only the term $2A_1A_2I_{LED}(\lambda)\cos\left(\frac{4\pi nL}{\lambda}\right)$. This term is then further processed by Hilbert transform to extract the envelope.

It is well-known that [6]: if a modulation signal $m(t)$ is low-pass and the carrier $\cos(t)$ is at higher frequency and their spectra do not overlap, then the Hilbert transform of their product $p(t)$ follows

$$\begin{aligned}
H[p(t)] &= H[m(t) \cos(t)] \\
&= m(t)H[\cos(t)] \\
&= m(t) \sin(t)
\end{aligned} \tag{2-12}$$

where $H(\cdot)$ denotes the Hilbert transform. Therefore $m(t)$ can be extracted as follows

$$m(t) = (p^2(t) + H^2[p(t)])^{1/2} \tag{2-13}$$

Then $\cos(t)$ is then obtained by normalization. In our case, $m(t)$ is $2A_1A_2I_{LED}(\lambda)$. We choose the cavity length large enough to move the cosine term away from the $I_{LED}(\lambda)$ spectrum to higher frequency and therefore they practically have no overlap. Therefore $2A_1A_2I_{LED}(\lambda)$ can be extracted and normalization results $\cos(\frac{4\pi nL}{\lambda})$, from which L can be determined.

2.5 References

- [1] K. T. V. Grattan, and B. T. Meggitt, *Optical fiber sensor technology* (Chapman & Hall, 1995).
- [2] V. Bhatia, M. B. Sen, K. A. Murphy, and R. O. Claus, "Wavelength-tracked white light interferometry for highly sensitive strain and temperature measurements," *Elect. Lett.*, vol. 32, pp. 247-249.
- [3] E. Cibula, D. Donlagic, and C. Stropnik, "Miniature fiber optic pressure sensor for medical applications," in *Proc. of IEEE Sensors 2002, First IEEE Int. Conf. on Sensors*, Piscataway, NJ, 2002, vol. 1, pp.711-714.
- [4] S. Chen, K. T. V. Grattan, A. W. Palmer, and B. T. Meggitt, "Digital processing techniques for electronically scanned optical fibre white light interferometry", *Appl. Opt.*, pp. 6003, 1992.

- [5] B. Qi, G. R. Pickrell, J. Xu, P. Zhang, Y. Duan, W. Peng, Z. Huang, W. Huo, H. Xiao, R. G. May, and A. Wang, "Novel data processing techniques for dispersive white light interferometer," *Opt. Eng.*, **42**, 3165-3171 (2003)
- [6] W. Tranter, K. Shanmugan, T. Rappaport, and K. Kosbar, *Principles of Communication Systems Simulation with Wireless Applications* (Prentice Hall, 2003).

CHAPTER 3

Ultra Miniature Fiber-Tip Pressure Sensor

The design of high-temperature pressure sensor has remained as one of the most challenging in fiber-optic sensing, details of which has been discussed in Chapter 1. Any advancement in this field would potentially open up a wide spectrum of industrial applications. This chapter introduces a novel ultra-miniature (125 μ m in diameter) pressure sensor fabricated on the tip of a fiber through a series of fiber micro-machining processes. Its high-temperature performance has been demonstrated in both laboratory tests and field trials, exceeding the current capability of not only fiber-optic sensors, but electronic sensors as well.

This chapter is organized as follows. Section 3.1 introduces the background and the inception of sensor concept, followed by fabrication procedures in Section 3.2. Various aspects of sensor signal are analyzed in Section 3.3, which helps improve sensor design and fabrication. Sensor's in-lab performance is explored thoroughly in Section 3.4. The testing went further to include a jet engine field test, as presented in Section 3.5. Because of its extremely small size, the sensor also draws considerable interests for biomedical applications. Section 3.6 addresses issues and concerns in this area. Summary can be found in section 3.7.

3.1 Background in high-temperature fiber-optic pressure sensing

The most common structure of a conventional fiber-optic pressure sensor is illustrated in Figure 3-1 (a). Almost always Fabry-Perot based, it consists of a fiber, a bulky base with a recessed cavity, and a diaphragm on the top, all of which are held together by adhesives. Ambient pressure variation will deflect the diaphragm to change the cavity length, i.e., the distance from the diaphragm to the fiber end.

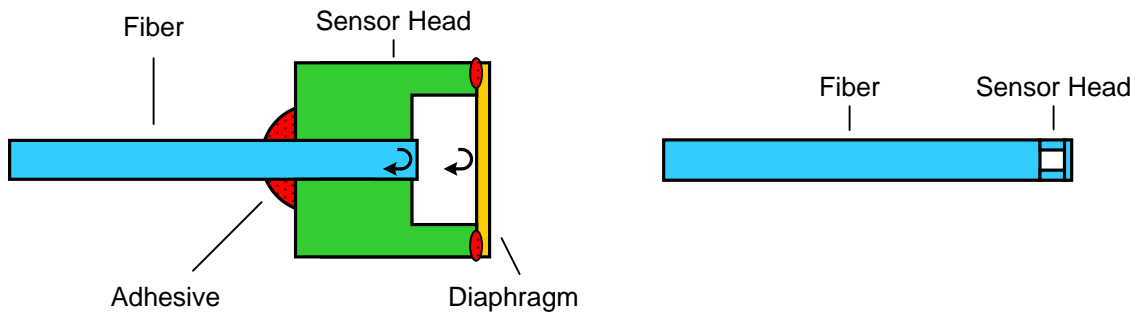


Figure 3-1. Conventional structure of a fiber-optic pressure sensor

Such a configuration suffers three major temperature-limiting difficulties:

D1). Low-temperature adhesives, which are often of Epoxy-type and usable up to at most 300°C. These materials exhibit inelastic response to pressure and stress, therefore severely impair sensor's repeatability.

D2). Low-temperature materials. Besides fiber's fused silica, other frequently used materials include doped glass (e.g. Borosilicate glass), silicon, metal, or even polymer. Mechanical properties of these materials deteriorate quickly at elevated temperature. For instance, borosilicate glass, with a softening point around 800°C, can only operate at a much lower temperature with reasonable mechanical strength due to material creep.

D3). Thermal expansion mismatch. With various materials involved, the structure could fail by stress caused by mismatching thermal expansions.

These difficulties need to be carefully addressed before attempting for technology breakthrough. The concept of the novel sensor design begins with solving the above difficulties, as stated in the following:

- S1). Adhesive-free, directly bonding the sensing parts together. This will remove D1.
- S2). Single material. Since glass fiber is inevitable, we then choose fused silica as the only material for the entire structure. This will address D3.
- S3). High-temperature material. Fused silica, whose softening point is around 1600°C, has a reasonable chance to reach beyond current technologies. This will hopefully solve D2.

The resulting design, an all-fused-silica pressure sensor, will eliminate the thermal expansion mismatch and avoids any adhesives, therefore expected to be functional at high temperature. It would be of a better design if the entire structure, including the Fabry-Perot cavity and the diaphragm, can be made with fiber size, as in Figure 3-1 (b). Its light weight and small size will bring minimal impact to the measured system. In addition, investigating the performance of this sensor would produce knowledge about the upper temperature limit a fused-silica-fiber based pressure sensors can reach.

Although fused silica has excellent optical, mechanical and thermal properties, it was rarely the choice for high-temperature sensing diaphragms mainly because of the bonding difficulties, which used to require adhesives. To reduce this sensing concept into practice, the keys rely on

- (a) how to achieve adhesive-free bonding of fused silica at fiber size.
- (b) how fused silica will perform at high temperature

In the rest of this chapter, we will have in-depth discussion on these topics.

3.2 Sensor Fabrication

3.2.1 Fiber micro-machining Techniques

Fabrication of sensors on the tip of a fiber involves various micro-machining processes to generate micro-scale fiber structures [1-3]. In this research, we developed a combination of the following three techniques to reach our goals, as discussed in the following sections (a), (b) and (c).

(a). Special fusion splicing

Today's fusion splicing of optical fibers is done automatically on sophisticatedly designed fusion splicers which aligns two stripped and cleaved fibers and melts them with an electric arc while pushing them together to make the joint. State-of-the-art fusion splicers allow the tuning of many of parameters. The most important would be the arc duration, its power, the distance between fibers before arcing, and the amount they are pushed together. In a regular splicing, arc power and duration are set sufficiently large to completely melt the fibers. Surface tension will then let the melted glass flow to produce a joint smooth and uniform as the rest of the fiber, as illustrated in Figure 3-2 (a). A good splicing point is usually indiscernible for same types of fibers, e.g. singlemode fiber to singlemode fiber, while between different fibers, as the SM to MM fiber splicing in Figure 3-2 (b), the joint is usually clear.

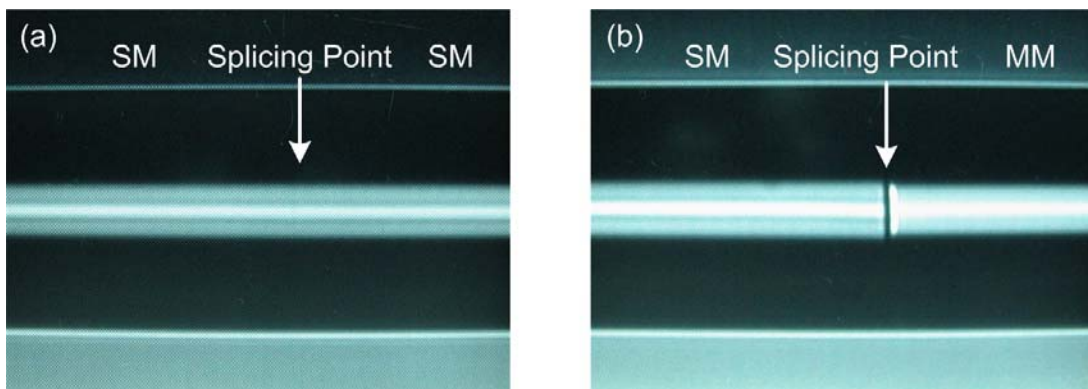


Figure 3-2. (a) SM-SM splicing; (b) SM-MM splicing

On the contrary to regular fusion splicing, special splicing situations involve specialty fibers (e.g. holey fiber, photonics crystal fiber and hollow fiber) with micro-scale structures and often requires much lower arc power and duration in order not to overheat and collapse these structures. Figure 3-3 displays a good splicing under controlled conditions between a singlemode fiber and a silica capillary tube whose hollow core extends to the splicing point, as compared to the collapsed core under regular conditions.

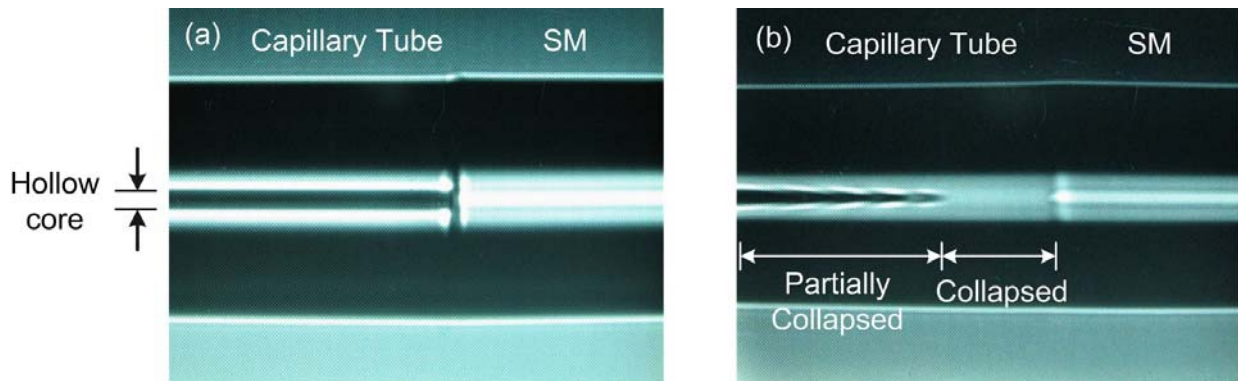


Figure 3-3. (a) SM-Capillary tube splicing under special condition; (b) Under regular condition

However, insufficient arc power or duration will compromise splicing strength for subsequent handling and processing. Fine-tuning these splicing parameters is therefore critical to achieve both strong connection and structural integrity.

Besides splicing, fusion splicer is capable of performing other fabrication functions as well, such as fiber-tip ball lens and fiber tapers. By controlling the 3-D motion of fibers and the arc characteristics, one could possibly generate a range of other structures.

(b). Precision cleaving

Probably the most performed operation on optical fibers, cleaving offers a clean breakage of fiber, mainly to facilitate successful splicing. It starts by introducing a microscopic fracture to the fiber, e.g. a lateral surface scratch by sharp alloy blade. Then proper tension is applied to let the

fracture propagate through the fiber and create a flat endface. Figure 3-4 shows the endview of a cleaved fiber. For purpose of splicing, there is no exact control on where the fiber is to be cleaved. In our sensor fabrication, however, it has to be precisely controlled to produce features with designed dimension. Figure 3-4 (b) shows a singlemode fiber with two other different fibers spliced and cleaved on top of it. Such cleaving is currently carried out manually under an Olympus 40× microscope with Fujikura CT40B precision cleaver, as shown in Figure 3-4 (c).

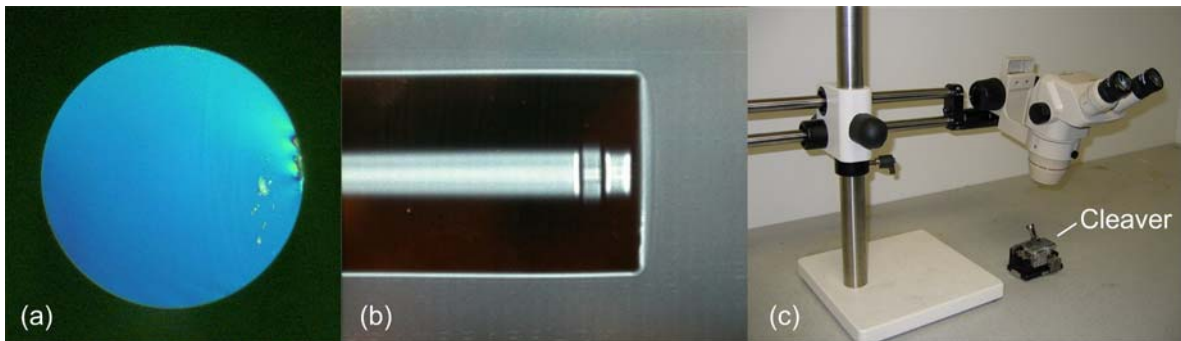


Figure 3-4. (a) Cleaved fiber; (b) Precision cleaving; (c) Cleaving under microscope

For better position control, the ideal setup would include CCD camera and appropriate lens to display highly magnified fiber image on a scaled monitor. Fiber can be adjusted by linear stages to position cleaving point precisely, permitting a potential micron or even sub-micron precision.

c). Wet chemical etching

Chemical etching is a basic lithographical process where fused silica can be removed by reaction with hydrofluoric acid (HF) to form a particular pattern defined by a mask. In our sensor fabrication, instead of using a mask, we exploit the fact that doped and undoped fused silica have different etching rates in buffered HF (BHF)[4][5]. For a germanium (Ge) -doped multimode (MM) fiber, its core (doped) is etched much faster than cladding (undoped), as shown in Figure 3-5, where graded-index MM fibers with 62.5 μm and 50 μm core were immersed in 50% HF for 5 minutes. The cores were removed while the cladding was almost intact, leaving a hollow-core

structure which will form the basis for Fabry-Perot cavity fabrication. The parabolic etching profile reflects different etching rates as a result of the graded dopant distribution.

In 50% HF, the center of the 62.5 μm fiber core will be etched at a rate of about 17 $\mu\text{m}/\text{min}$ while the undoped fused silica has a much slower rate of 1 $\mu\text{m}/\text{min}$.

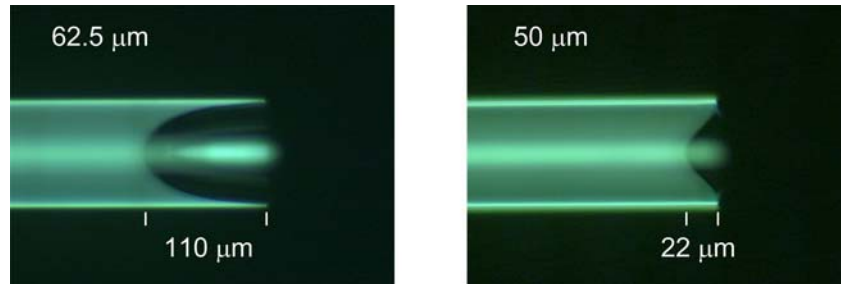


Figure 3-5. MM fibers etched in 50% HF for 5 minutes.

3.2.2 Fabrication Steps

The fabrication involved three types of silica fibers: telecommunication-grade singlemode (SM) fiber, 62.5/125 μm graded-index MM fiber and 105/125 μm step-index MM fiber. The 62.5 μm fiber is Ge-doped in the core and undoped in the cladding, while the 105/125 μm fiber has an undoped core and fluorine-doped cladding that can be quickly etched off and serves no actual use here. The ideal replacement for 105 μm fiber would be a 125 μm pure fused silica rod. The etchant is 50%wt HF. Fiber splicing, cleaving and etching, together with these fibers, can be combined in a number of ways to create the miniature structure in Fig. 3-1 (b). In the following we introduce two basic procedures.

a) Procedure One

Step 1:

First a piece of SM fiber is prepared by cleaving it. Since its core is Ge-doped, it is necessary to protect it from later exposure to HF that will create curved surface and reduce the reflectivity

significantly. To serve this purpose, a 10~20 μm layer of etch barrier is made by splicing a 105 μm fiber to the SM fiber and then cleaving it, as shown in Figure 3-6. The low etching rate will allow this layer to retain a very flat surface during cavity etching. This step can be skipped where signal to noise ratio is of less concern.

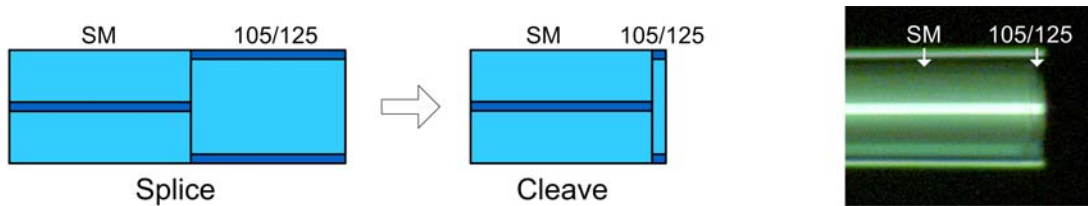


Figure 3-6. Fiber tip sensor etch barrier layer

Step 2:

Next, the fiber assembly is spliced to a 62.5 μm -core MM fiber and cleaved. The length of the MM fiber left is controlled to be desired cavity length. The assembly is then immersed in HF for a certain period of time, usually 1-2 min, determined by cavity length and core etching rate. A slight over-etch is required to ensure the center of the cavity bottom is clearly open to allow efficient light transmission. Figure 3-7 illustrates this step. The inclined side wall is a result of the graded-index profile which leaves some residue of the 62.5 μm core around the cavity bottom. They can be removed by use of step-index MM fibers. The structure is now ready for diaphragm bonding.

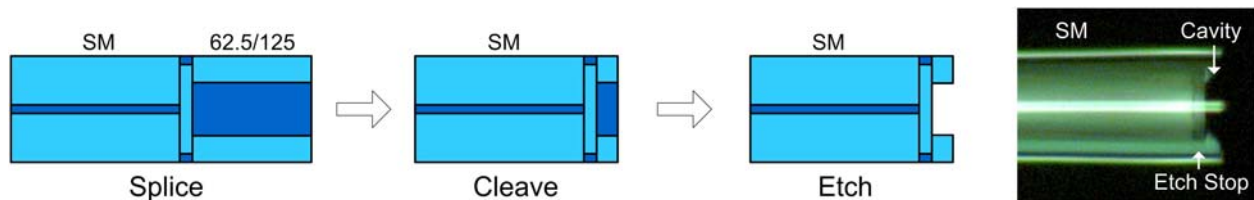


Figure 3-7. Fiber tip sensor cavity formation process

Step 3:

As shown in Figure 3-8, a 105 μm fiber is spliced with the cavity and cleaved, leaving a diaphragm on top of it. To improve sensitivity, the diaphragm can be further etched to reduce its thickness. The splice here is low-power short-duration special splicing, and the pre-fusion power and duration are carefully chosen to minimize the amount of trapped air inside the cavity. This is essential to reduce temperature cross-sensitivity.

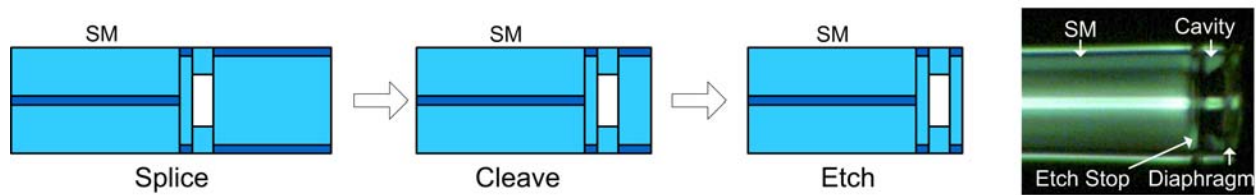


Figure 3-8. Fiber tip sensor diaphragm fabrication process

The final structure is primarily composed of undoped fused silica.

Although this procedure is simple, it is difficult to reach very thin thickness and very high sensitivity. Due to the non-smooth fiber surface at the splicing point resulting from the low-power arc, as well as the existence of the cavity, the 105 μm fiber has to be cleaved some distance away from the diaphragm-cavity splicing point, usually 20~25 μm , to avoid breakage. On one hand, this relatively thick layer of undoped silica will take longer to be etched down. On the other hand, the maximum etching time is determined by the thickness of the cavity wall. This dilemma limits the fabrication flexibility and makes it difficult to achieve very high sensitivity. Therefore another procedure was developed to address this issue.

b) Procedure Two

Step 1.

The first step, as in Figure 3-9, is to prepare a thin layer of undoped fused silica on the end of a doped fiber, achieved by fusion splicing the 105 μm and 62.5 μm fiber and cleaving on the 105 μm

side. Standard splicing parameters were used. This thin layer usually can be made about 10 μ m-thick or less, serving two purposes in the following steps.

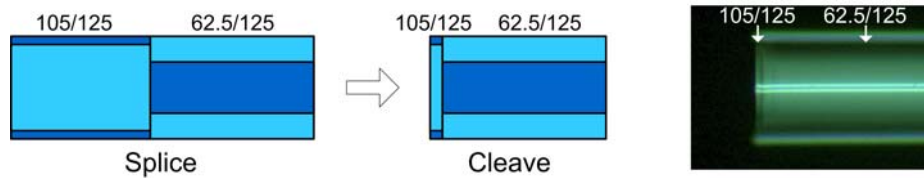


Figure 3-9. Sensor fabrication process

Step 2:

The second step, as in Figure 3-10, produces a cavity on the SM fiber tip. A complete assembly from step 1 is spliced with the SM fiber using standard parameters. The 62.5 μ m fiber is then cleaved to a certain length, followed by etching to remove the core and generate the cavity. As in the previous method, this thin layer of fused silica serves as an etch stop. Figure 3-12 shows photos of the cavity bottom and edge after etch.

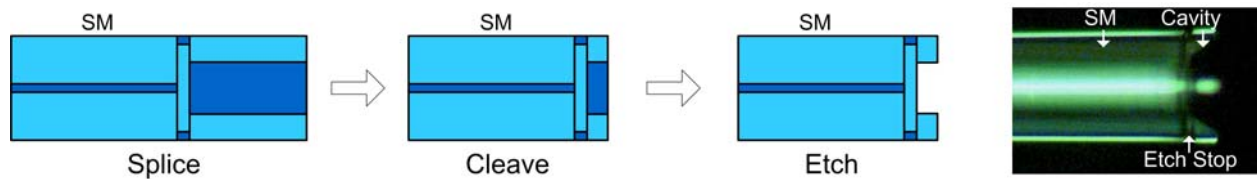


Figure 3-10. Cavity generation

Step 3:

The final step, as in Figure 3-11, is to generate a diaphragm to seal the cavity. Again, one complete assembly from step 1 is spliced to the cavity produced in step 2 using special splicing parameters. Then the 62.5 μ m fiber is again cleaved and etched, exposing the thin layer of fused silica, which in this step serves as the diaphragm. This diaphragm can be further etched to adjust its thickness and the sensor's sensitivity. Figure 3-12 (c) shows a photo of a very thin diaphragm

fabricated this way, where the concentric color rings are the interference of the two diaphragm surfaces under illumination of visible light, indicating a submicron thickness. The increasing fringe density from center to perimeter reveals a slightly concave surface as a result of the graded doping profile in the 62.5 μm fiber core whose center reaches the diaphragm first.

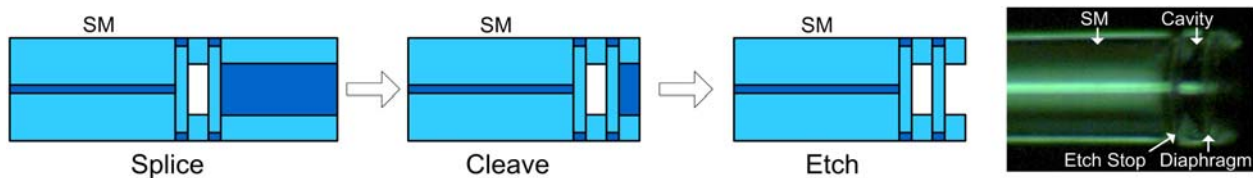


Figure 3-11. Diaphragm fabrication

This new process is a significant improvement over the former design. Instead of closely cleaving near the cavity, it pre-fabricates the diaphragm in the first step where the standard splicing produces a smooth surface at the splicing point allowing cleaving less than 10 μm away with high quality (Figure 3-9). In the final step, the 62.5 μm fiber serves just as a sacrificial layer to support this thin diaphragm during splicing but is removed later. Therefore neither the length nor the quality of the final cleave of this 62.5 μm fiber (Figure 3-11) is critical. After a quick etching (usually 1~2 minutes), the sacrificial layer (62.5 μm core) is removed to expose the high-quality thin diaphragm. Then relatively shorter etching could further reduce its thickness. This way, the diaphragm deflection is an order of magnitude more sensitive than before, improved from tenths of nm/psi (1psi = 6.89 $\times 10^3$ Pa) to a few nm/psi or even higher. The diaphragm shown in Figure 3-12 (c) responds to pressure with about 20nm/psi. In addition, this process offers the potential for batch processing in the first step by depositing silica dioxide to form the thin layer, making it possible to produce even thinner diaphragm and higher quality. Figure 3-13 compares a tip sensor with a dime.

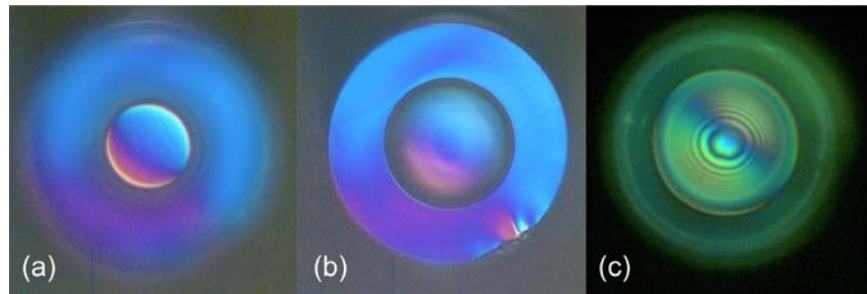


Figure 3-12. Photos. (a) Cavity edge; (b) Cavity bottom; (c) Diaphragm.

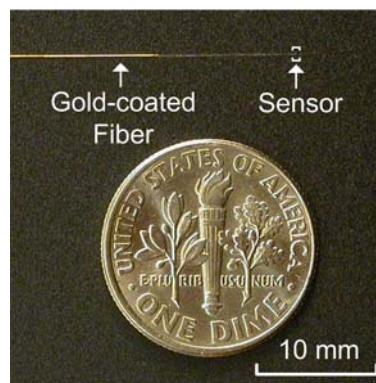


Figure 3-13. Tip sensor as compared to a dime

c). Improvement

The methods and results presented above are based on available materials and not necessarily the only or best approaches. To make great improvement, we can replace the 105 μm fiber by 125 μm pure fused silica rod, use step-index 62.5 μm fiber with larger dopant concentration, or fabricate the thin layer by deposition.

Other alternatives include using hollow core fiber to produce cavity directly with no need for etching or etch barrier, as shown in Figure 3-14. It can also be fabricated through traditional

photolithography by coating the fiber end with photoresist, using another fiber to deliver UV light for pattern definition and exposure, developing the photoresist and etching (Figure 3-15).

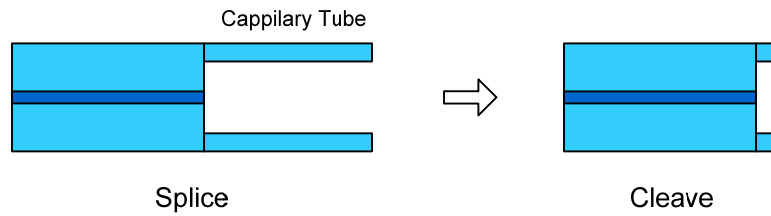


Figure 3-14. Using capillary tube for cavity fabrication

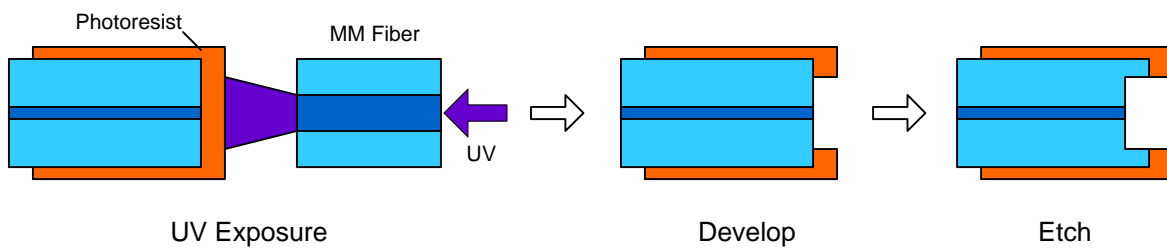


Figure 3-15. Photolithography processes for pit fabrication

3.3 Theoretical Analysis of Sensor Signals

3.3.1 Spectrum

In this extrinsic Fabry-Perot (FP) interferometric sensor, light launched into the SM fiber will generate three reflections, one from the bottom of the cavity (E_1), and the inner (E_2) and outer (E_3) surfaces of the diaphragm, as shown in Figure 3-16.

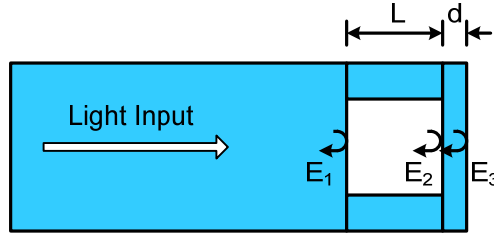


Figure 3-16. Reflections in a miniature tip sensor

The total reflected intensity can be written as

$$\begin{aligned}
 I(\lambda) &= |E_1 + E_2 + E_3|^2 \\
 &= \left| A_1 + A_2 \exp\left(-\frac{j4\pi L}{\lambda} + j\pi\right) + A_3 \exp\left(-\frac{j4\pi(L+nd)}{\lambda}\right) \right|^2 \\
 &= A_1^2 + A_2^2 + A_3^2 - 2A_1A_2 \cos\left(\frac{4\pi L}{\lambda}\right) \\
 &\quad - 2A_2A_3 \cos\left(\frac{4\pi nd}{\lambda}\right) \\
 &\quad + 2A_3A_1 \cos\left(\frac{4\pi(L+nd)}{\lambda}\right)
 \end{aligned} \tag{3-1}$$

where A_1 , A_2 , and A_3 are the amplitudes of E_1 , E_2 , and E_3 , respectively; L is the cavity length, d is the diaphragm thickness, n is the refractive index of fused silica, and λ is wavelength. E_2 has an extra phase shift of π at the air–silica interface.

Unlike the basic two-beam interference mentioned in Chapter 2, E_3 can either strengthen or cancel E_2 depending on the diaphragm thickness, hence modulating the entire spectrum with a slowly varying envelope, as discussed in the following.

If the optical thickness of the diaphragm, nd , satisfies

$$2nd = N\lambda + \frac{\lambda}{2}, \quad N = 0, 1, 2, \dots \tag{3-2}$$

E_2 and E_3 will have a phase difference of

$$\frac{4\pi nd}{\lambda} + \pi = (2N + 2)\pi, \quad N = 0, 1, 2, \dots \quad (3-3)$$

and therefore add in phase and interfere constructively. Then Eq. (3-1) becomes

$$I(\lambda) = A_1^2 + (A_2 + A_3)^2 - 2A_1(A_2 + A_3) \cos\left(\frac{4\pi L}{\lambda}\right) \quad (3-4)$$

with a maxima of

$$\begin{aligned} I_{\max}^+ &= A_1^2 + (A_2 + A_3)^2 + 2A_1(A_2 + A_3) \\ &= (A_1 + A_2 + A_3)^2 \end{aligned} \quad (3-5)$$

Similarly, when

$$2nd = N\lambda \Rightarrow \frac{4\pi nd}{\lambda} = (2N + 1)\pi, \quad N = 0, 1, 2, \dots \quad (3-6)$$

E_2 and E_3 will be out of phase and cancel each other to reduce the total reflected energy, with a maximum power of only

$$\begin{aligned} I_{\max}^- &= A_1^2 + (A_2 - A_3)^2 + 2A_1(A_2 - A_3) \\ &= (A_1 + A_2 - A_3)^2 \end{aligned} \quad (3-7)$$

Although not absolutely required, the in-phase case is preferred for higher signal power and achieved by monitoring the signal strength during etching. Eq. (3-2) or (3-3) then produces a series of ‘optimal’ diaphragm thickness d_{opt} . For instance, if $\lambda=1.55 \mu\text{m}$, and $n = 1.444$, d_{opt} is determined to be $1.879 \mu\text{m}$ for $N = 3$.

Figure 3-17 plots the spectrum of a sensor at room temperature and pressure from 1320~1700 nm with its maximum power located around 1550nm and its minimum around 1370nm, clearly showing the modulation by E3. The spectrum is fitted using Eq. (3-1) with $A_1 = 0.495$, $A_2 = 0.371$, $A_3 = 0.158$, $L = 16.343 \mu\text{m}$, and $d = 1.883 \mu\text{m}$, very close to the optimal thickness calculated above.

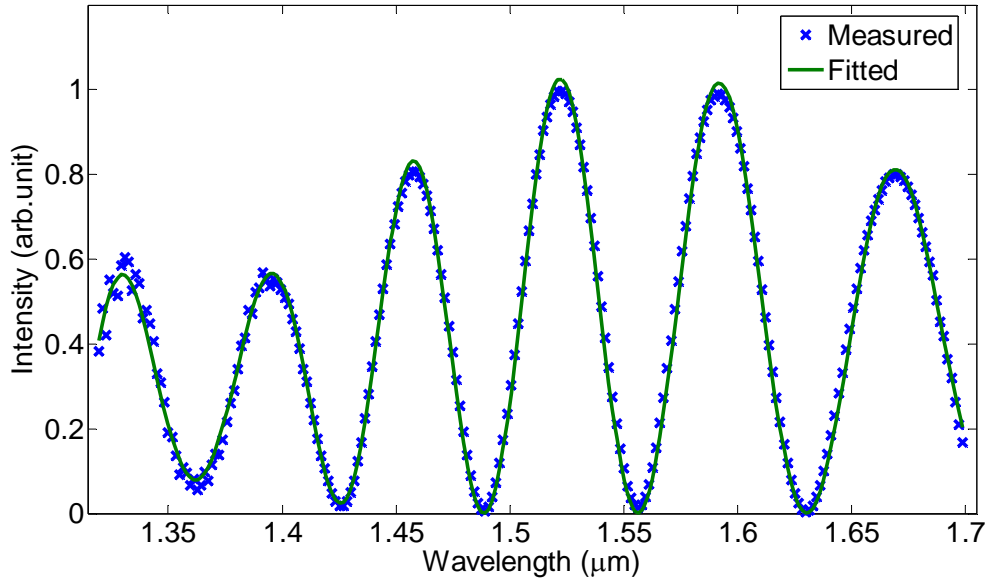


Figure 3-17. Output spectrum of sensor 1 at room temperature and pressure.

3.3.2 Sensitivity

When ambient pressure varies, the diaphragm will deflect and the cavity length L will change according to [6]

$$\begin{aligned} \Delta L &= \frac{3(1-\nu)R^4}{16Ed^3} \Delta p \\ &\triangleq S_p \Delta p \end{aligned} \quad (3-8)$$

where ν and E are Poisson's ratio and Young's modulus of fused silica, respectively; R is the radius of the diaphragm, d is the diaphragm thickness, Δp is the ambient pressure change, and S_p

is defined as the sensor's pressure sensitivity. For a diaphragm with given material and dimension, S_p is constant which results in Δp linearly dependent on ΔL . Figure 3-18 shows the change in S_p with d , given $E = 73\text{GPa}$, $\nu = 0.17$, and R is estimated to be $33\mu\text{m}$, a slightly larger value than the radius of the core due to etching. S_p increases quickly to a few nm/psi when d decreases below $2\mu\text{m}$. The solid circles are the theoretical sensitivity at the 'optimal' thickness derived by Eq. (3-2) for 1550nm .

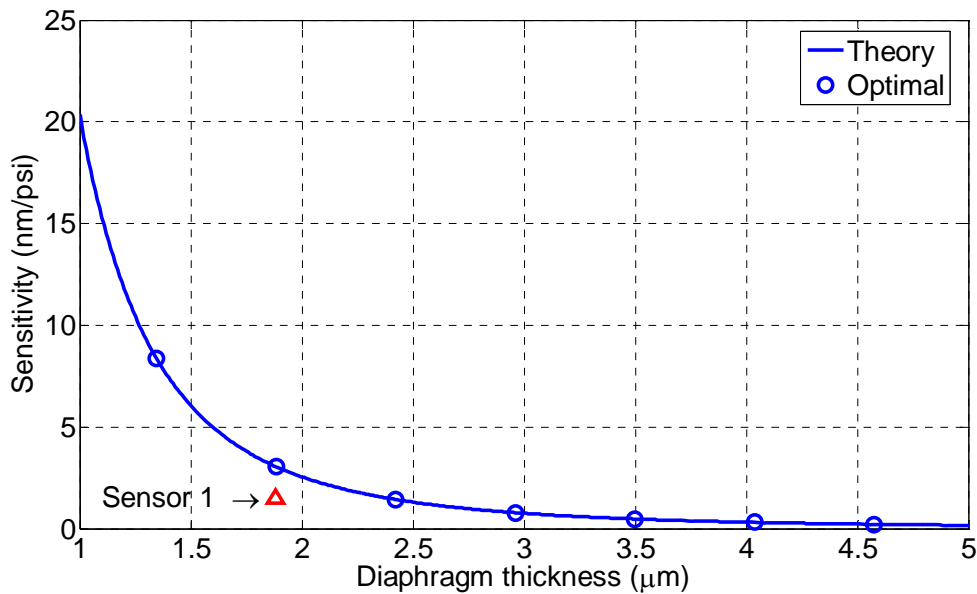


Figure 3-18. Theoretical sensitivity for the sensor.

For sensor 1's $1.883\mu\text{m}$ diaphragm, its measured sensitivity, $1.49\text{nm}/\text{psi}$ as marked by the triangle in Figure 3-18, is about half the theoretical value of $3.05\text{nm}/\text{psi}$. The error partially comes from the parameter accuracy in calculation. Another contribution may be from the concave diaphragm surface mentioned above, which has an average thickness larger than its center where light beam mainly focuses, thus reducing the sensitivity according to Eq. 3-8.

3.3.3 Dynamic Pressure Response

Previous section discusses sensor's response to static or slow-varying pressure change. There are also important applications where dynamic or high-frequency variation is of more interests. How the sensor vibrates under such pressure would be critical to meet design requirement.

Many vibration systems, including our case of a circular diaphragm clamped at edge, can be modeled as a single degree-of-freedom system, as in Fig 3.19 [7]. It consists of a mass m attached to a fixed support by a spring k and a viscous damper c . This quite simplified model could still provide helpful insights into the fundamental behavior of the system.

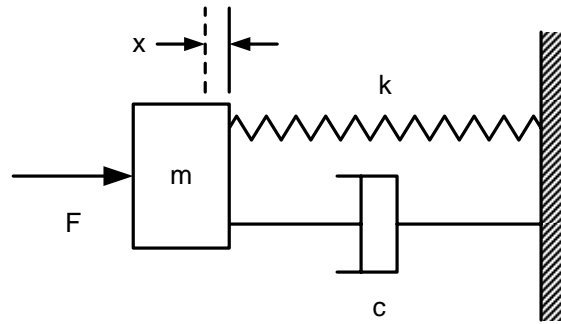


Figure 3-19. A single degree-of-freedom vibration system

The displacement of the mass, x , under a harmonic excitation $F = F_0 \sin \omega t$ can be described by the following differential equation [7]

$$m\ddot{x} + c\dot{x} + kx = F_0 \sin \omega t \quad (3-9)$$

Its solution can be written as

$$\frac{x}{F_0/k} = \frac{\sin(\omega t - \theta)}{\sqrt{(1 - \omega^2/\omega_n^2)^2 + (2\zeta\omega/\omega_n)^2}} = R_d \sin(\omega t - \theta) \quad (3-10)$$

where $\omega_n = \sqrt{\frac{k}{m}}$ is the angular natural frequency of the system (frequency $f_n = \omega_n/2\pi$),

$\zeta = \frac{c}{2m\omega_n}$ is a normalized damping factor determined only by the structure (the clamped

diaphragm in our case), $\theta = \tan^{-1}\left(\frac{2\zeta\omega/\omega_n}{1 - \omega^2/\omega_n^2}\right)$ is the phase response of the system.

Therefore a single-frequency excitation at ω would only cause response at the same frequency. R_d is a dimensionless response factor which describes the system's amplitude response to the excitation. It is also called magnitude transfer function or magnitude frequency response of the system. Typical R_d are shown in Figure 3-20 for $\zeta = 0.05, 0.1, \text{ and } 0.3$. It remains a constant value of unity at low frequency, reaches resonant peak around ω_n , and decreases to zero at higher frequency. For most diaphragm-based pressure sensors, they usually operate at frequencies below one fifth of ω_n , where R_d is often considered a constant. In other words, sensor's sensitivity will remain the same at frequencies low enough compared to its natural frequency, implying that sensor calibration using static pressure will be sufficient even for dynamic measurement.

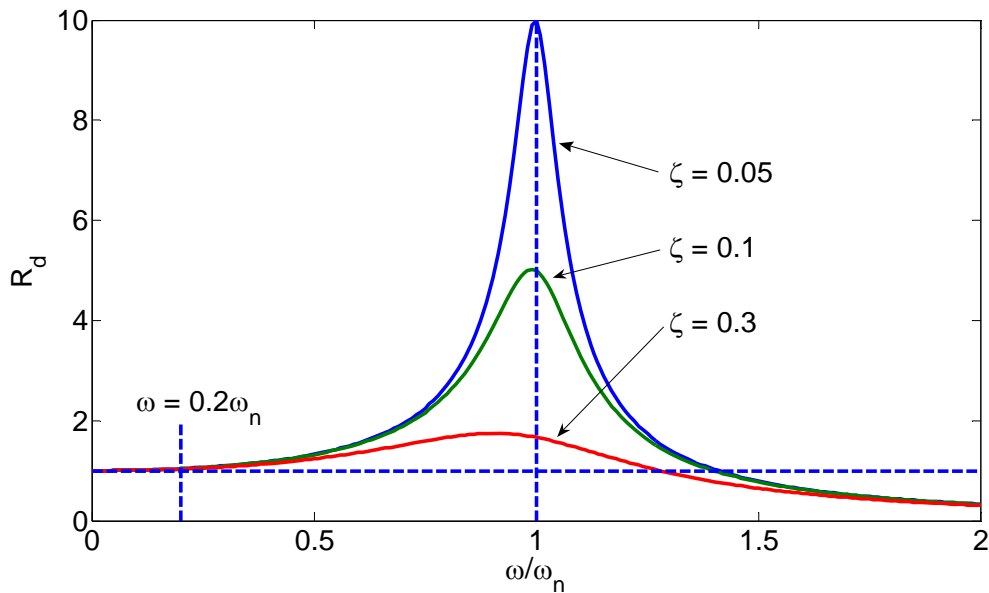


Figure 3-20. Frequency response of the diaphragm

For the diaphragm in our sensor, the angular natural frequency of its fundamental mode is determined as [6],

$$\omega_n = \frac{10.21h}{R^2} \left[\frac{E}{12\rho(1-\nu^2)} \right]^{1/2} \quad (3-11)$$

where d and R are the thickness the radius of the diaphragm, respectively, E and ν are the Young's modulus and Poisson's ratio of the material, respectively, and ρ is material density.

For the silica diaphragm, assume $E = 73\text{GPa}$, $\nu = 0.17$, $\rho = 2.2\text{ g/cm}^3$, $d = 2\mu\text{m}$, $R = 33\mu\text{m}$ (a little larger than the radius of the core due to etching), we have $\omega_n = 31.6 \times 10^6\text{ rad/sec}$, or $f_n = \omega_n/2\pi = 5\text{ MHz}$. Therefore the sensor can operate up to 1 MHz with no need for special dynamic calibration.

3.3.4 Size advantages

As discussed in the previous section, large resonant frequency is desired for larger dynamic range. In this regard, miniature sensor has an advantage over its large-size counterpart, i.e., given the same sensitivity, a smaller sensor has a higher ω_n to cover wider frequency range, as discussed below.

From Eq. (3-8) the sensor sensitivity is

$$\begin{aligned} S_p &\triangleq \frac{3(1-\nu)R^4}{16Ed^3} \\ &= k_1 \frac{R^4}{d^3} \end{aligned} \quad (3-12)$$

where k_1 is a proportional coefficient. Consider the case where the diaphragm shrinks in size with R reduced to αR and d to βd ($\alpha, \beta < 1$). Its sensitivity will change to

$$\begin{aligned} S_p' &= k_1 \frac{\alpha^4 R^4}{\beta^3 d^3} \\ &= \frac{\alpha^4}{\beta^3} S_p \end{aligned} \quad (3-13)$$

To keep the sensitivity unchanged, $S'_p = S_p$, we need $\beta = \alpha^{\frac{4}{3}}$. Now consider resonant frequency, from Eq. (3-11), we have

$$\begin{aligned} f_{mn} &= \frac{\sigma_{mn} h}{2\pi R^2} \left[\frac{gE}{12(1-\mu^2)} \right]^{\frac{1}{2}} \\ &= k_2 \frac{h}{R^2} \end{aligned} \quad (3-14)$$

where k_2 is a proportional coefficient.

For the smaller diaphragm, we have

$$\begin{aligned} f'_{mn} &= k_2 \frac{\beta h}{\alpha^2 R^2} \\ &= k_2 \frac{h}{\alpha^{\frac{2}{3}} R^2} \quad (\because \beta = \alpha^{\frac{4}{3}}) \\ &> f_{mn} \quad (\because \alpha < 1) \end{aligned} \quad (3-15)$$

Since $\alpha < 1$, f'_n is increased by $\alpha^{-2/3}$.

For example, assume $2R = 1$ mm and $d = 100$ μm for a regular sized pressure sensor. For a miniature sensor with the same sensitivity, $2R$ reduces to 62.5 μm , $\alpha = 1/16$ and f_{mn} is increased by a factor of $\alpha^{-2/3} = 6.35$ which is quite significant. At the same time, $\beta = \alpha^{4/3} = 1/40$, i.e., for an original 100 μm -thick diaphragm, the final thickness will be reduced to 2.5 μm which is quite feasible.

3.4 Laboratory Performance Test

3.4.1 Test Setup

To investigate the sensor's high temperature capability, spectrum detection was used to study how the cavity length responds to static pressure change at different temperatures. Details of the principle are given in Chapter 2.

Figure 3-21 shows the laboratory test setup. The spectrometer is a Micron Optics si720 high resolution Component Testing System (CTS), which has a built-in tunable laser source and a detector, sweeping at 5Hz from 1520nm to 1570nm with a resolution of 2.5pm to interrogate the sensor through a circulator. The sensor was sealed in a mullite (aluminum silicate, $3Al_2O_3 \cdot 2SiO_2$, a high-temperature refractory material) tube and pressurized by a pressure calibrator (Pressure Systems, Inc., 9035). The sensor end of the tube was placed in a furnace (Thermolyne 48000) together with a K-type thermocouple for temperature reference. A computer controls the pressure calibrator and retrieves spectrum and temperature data from CTS and a temperature gauge (OMEGA Dpi32-C24).

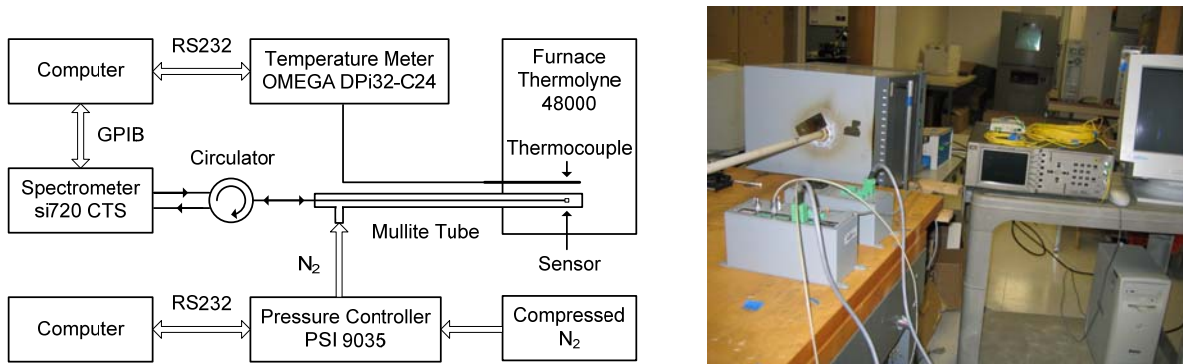


Figure 3-21. System setup for high-temperature static pressure test.

3.4.2 Signal Demodulation

Figure 3-22 plots the sensor spectrum under various pressures in logarithmic scale. Increasing the pressure reduces the cavity length L , hence blue-shifting the spectra.

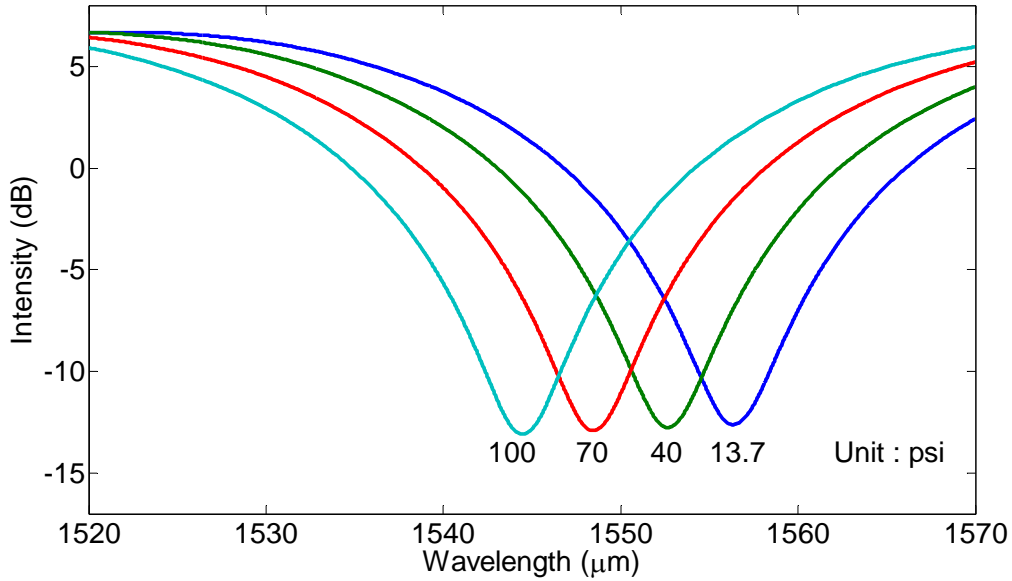


Figure 3-22. Sensor spectra at 13.7, 40, 70, and 100psi

Reversely calculating L would demodulate pressure. Curve-fitting the entire spectrum to obtain L as described previously is operable but computationally ineffective and very sensitive to initial conditions, therefore impractical for real-time signal demodulation. Tracing the interfering minima (valley) or maxima (peak) of the spectrum, as discussed in Chapter 2, is instead a very effective approach [8]. If the position of a valley, λ_v , has been determined, the cavity length can be calculated as

$$\frac{4\pi L_{calc}}{\lambda_v} + \pi = 2N\pi \Rightarrow L_{calc} = \frac{(2N-1)}{4} \lambda_v \quad (3-16)$$

where N is the fringe order (integer for interference minima and half-integer for interference maxima). With N pre-determined from the spectrum, L_{calc} is proportional to λ_v . In the algorithm,

a low-pass filter is first used for noise reduction and then a local parabolic curve-fitting around the valley determines λ_v with high resolution.

Eq. (3-16) is accurate only for two-beam interference, while in this sensor E_3 modulates the spectrum and L_{calc} is not necessarily equal to the actual cavity length L . However, due to the thin diaphragm thickness, the envelope is slow-varying and the spectrum is only slightly modulated. In addition, satisfaction of the optimal thickness condition of Eq. (3-2), which is the case for sensor 1, will make the envelope even flatter at the wavelength of interest. These will reduce the error in using L_{calc} as an estimator of L .

To examine more closely how E_3 would deviate L_{calc} from L , the previously generated fitting values for Figure 3-17 were used to produce simulated sensor spectra. Varying L while fixing A_1 , A_2 , A_3 , and d simulates the case where the sensor is under changing pressure. Then the valley-tracing algorithm was applied to these spectra to determine L_{calc} . The difference between L_{calc} and L is plotted in Figure 3-23. For a 300nm change in L (or equivalently 200psi change in pressure), L_{calc} lies within $\pm 8\text{nm}$, confirmed as an excellent estimator of L .

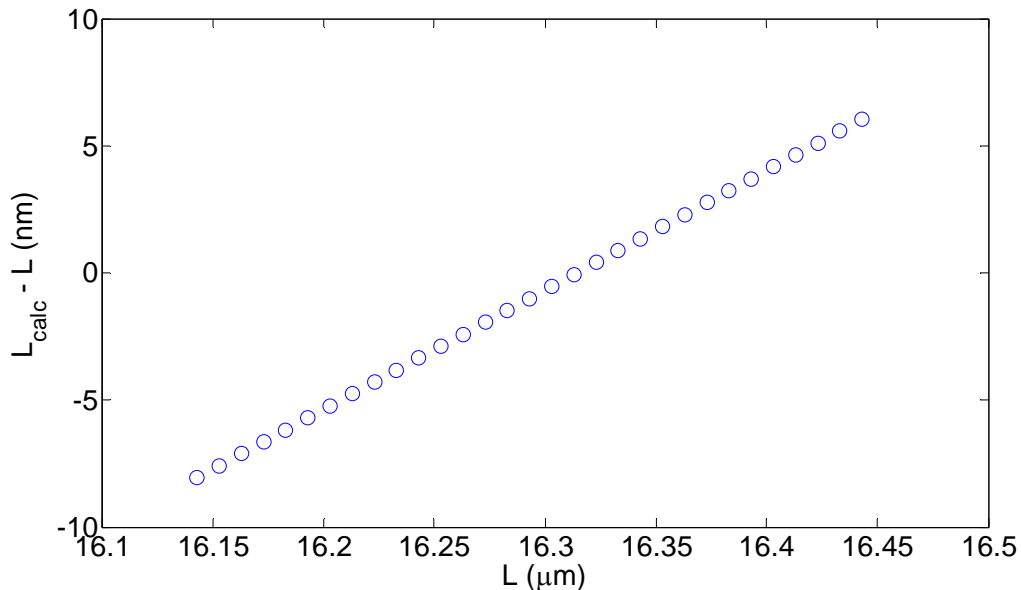


Figure 3-23. Cavity length simulation: actual value L vs. calculated value L_{calc}

In all the following discussions, if not otherwise mentioned, the cavity length will refer to L_{calc} .

3.4.3 High Temperature Static Pressure Test Results

Sensor 1 was tested at 24°C, 308°C, 412°C, 513°C, 562°C, and 611°C, with decreasing temperature increment, intending for a closer study on the sensor's high-temperature performance and the operation limit of fused silica diaphragm. At each temperature, the sensor was tested from 15psi to 30psi with a step of 0.5psi for three cycles. The full scale cavity length change was 23.4nm.

For comparison, sensor 2 with a thicker diaphragm (4.114 μm) and lower sensitivity (0.17nm/psi) was also tested, but at two more temperatures, 661°C and 710°C. The applied pressure was from 20psi to 160psi in steps of 10psi, also for three cycles. The full range diaphragm deflection was 23.8nm, almost the same as sensor 1.

a) Pressure Response

Figure 3-24 shows the pressure test results for sensor 1 at all temperatures with all three cycles of data plotted together. For temperatures up to 561°C, the results of the three cycles almost perfectly overlap each other while the 611°C results are less repeatable due to the drift caused by creep. Sensor 2 exhibited similar curves, as shown in Figure 3-25. The results demonstrate the sensor's operability up to the 600~700°C range.

b) Sensitivity

Pressure response at each temperature was linear-fitted for both sensors. The slopes represent sensor's sensitivity S_p , which is plotted against temperature in Figure 3-26. It reveals a 5.9% decrease from 24°C to 611°C for sensor 1, and 6.6% from 24°C to 710°C for sensor 2. This is the result of a slightly growing Young's modulus and Poisson's ratio of fused silica with rising temperature, as reported by Fukuhara et. al. [9] and reflected through Eq. (3-8).

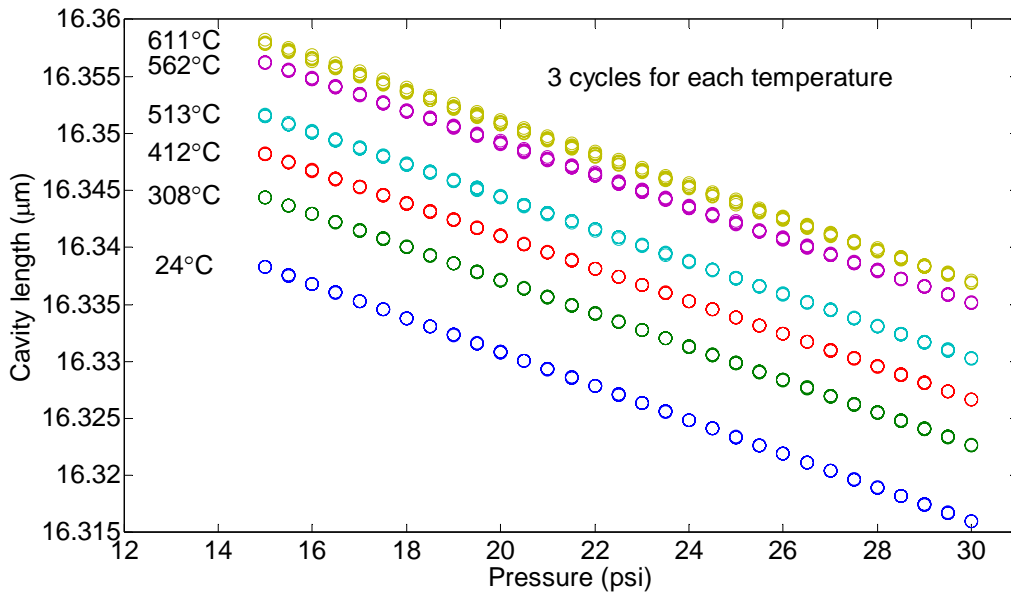


Figure 3-24. Sensor 1 testing results at different temperatures.

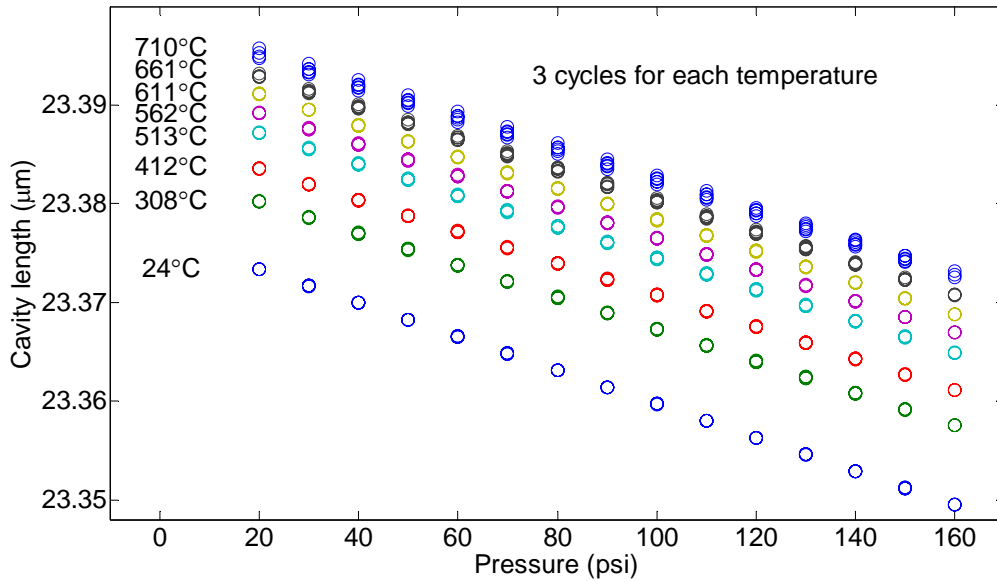


Figure 3-25. Sensor 2 testing results at different temperatures.

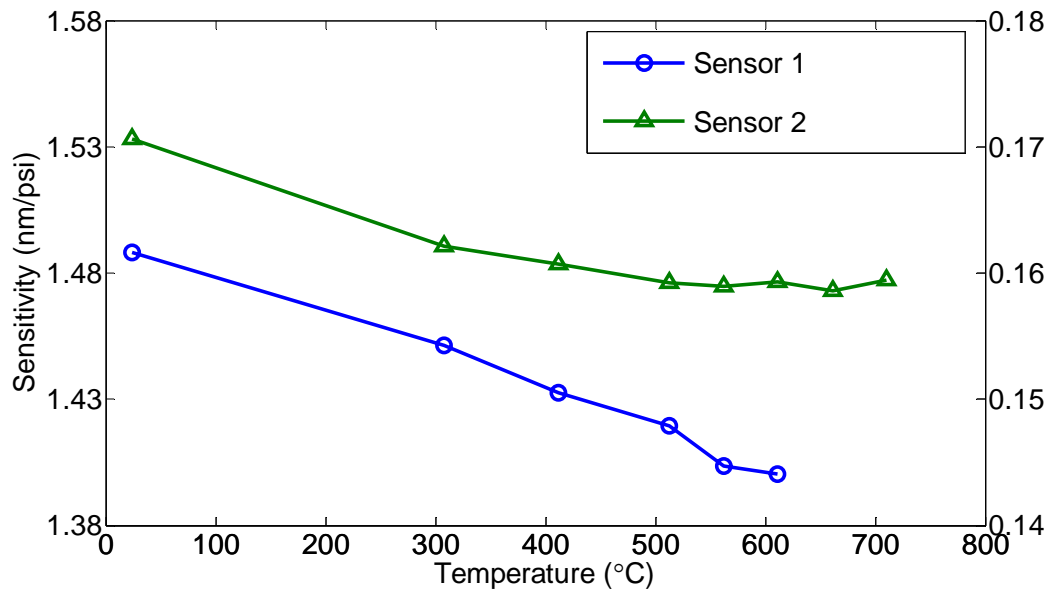


Figure 3-26. Sensitivity vs. temperature.

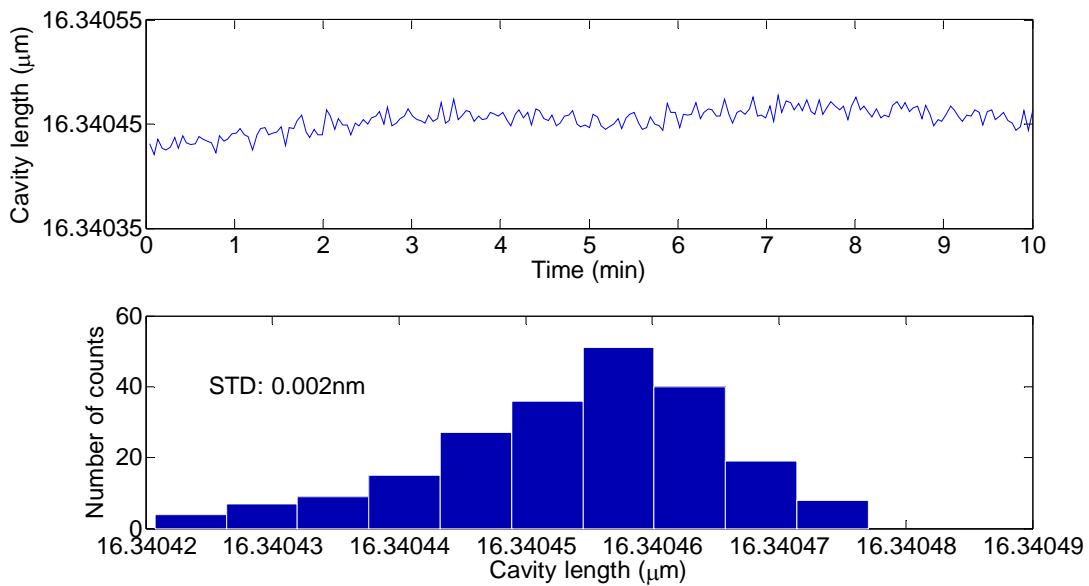


Figure 3-27. System resolution test.

c) Resolution

Figure 3-27 shows the short-term system stability test, recording cavity length for 5min at room temperature (RT) with a standard deviation of only 0.002nm. This means, for the 1.49nm/psi sensitivity of sensor 1, the system is able to resolve a pressure change of about $0.002\text{nm}/1.49\text{nm/psi} = 0.0013\text{psi}$. This is an excellent resolution resulted by the high performance of both the algorithm and the CTS.

d) Repeatability

On Figure 3-24 and 3-25, it is clear that at low temperature, data in different testing cycles repeats very well, while they become less repeatable at higher temperatures. The sensor repeatability was estimated as follows. At each temperature, the deviation of the measured cavity length from the linear fit, ε , was calculated for all data points in the three rounds. The ratio of the average deviation, ε_{avg} , to the full scale cavity length change ΔL_{FS} , $\varepsilon_{\text{avg}}/\Delta L_{\text{FS}}$, is defined as the relative repeatability and plotted in Figure 3-28, which shows a deteriorating repeatability, from 0.10% at 24°C to 0.62% at 611°C for sensor 1 and from 0.06% at 24°C to 1.40% at 710°C for sensor 2. This is the result of increasing material creep at higher temperature and will be discussed later.

For sensor 2, the deviation starts increasing significantly at around 600°C, about 50°C higher than for sensor 1. Although this is not much, it may be an indication that the thicker diaphragm exhibits less creep than a thinner one when subject to the same amount of deflection. In general, we conclude that all-fused-silica sensors can operate up to 600-700 °C range with reasonable performance. This is already 150~250 °C higher than current technologies.

e) Material creep

Material creep is the major factor limiting the sensor's high temperature repeatability. Figure 3-29 shows the creep test of sensor 1 at 611°C when pressurized by a step change from ambient pressure (13.7psi) to 50psi for 10min and then back to ambient pressure. At 50psi, the cavity underwent a 1nm drift, about 1.8% Full Scale, in an exponential-like manner. When released, the

sensor slowly returned to its original position, although the time constant is increased. This indicates it is a recoverable creep.

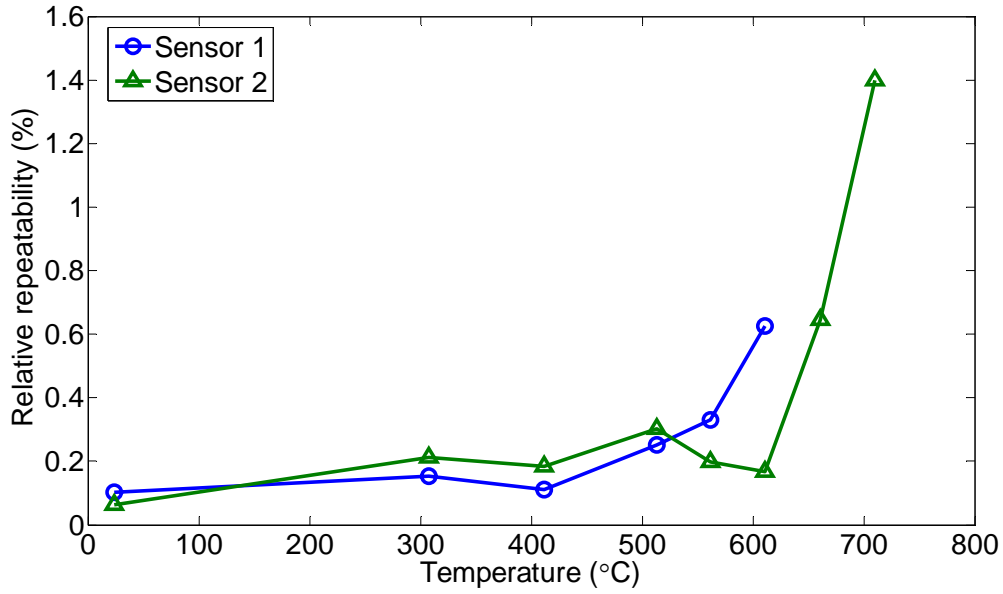


Figure 3-28. Relative repeatability of the sensors at different temperatures.

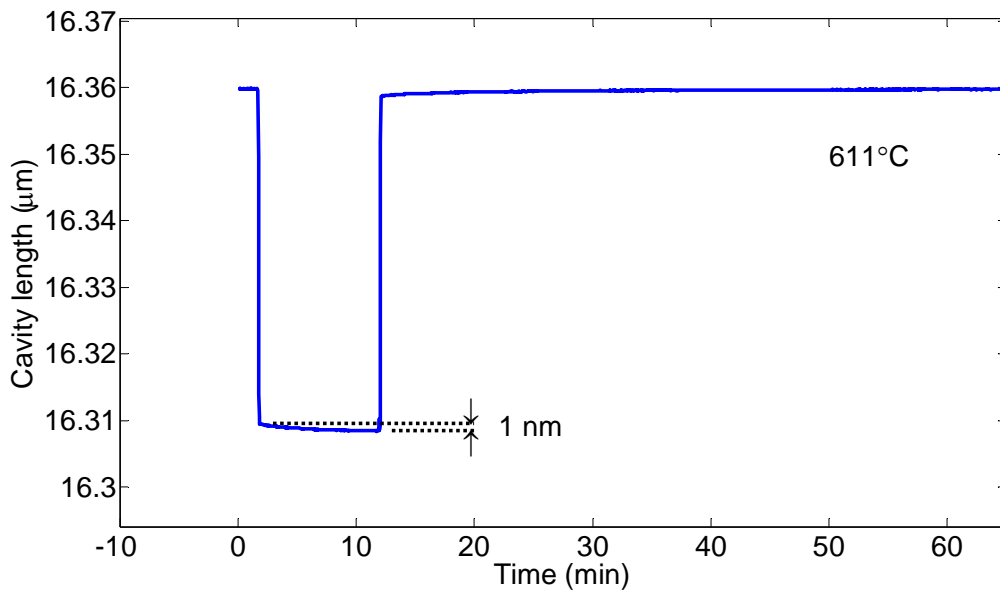


Figure 3-29. Creep of sensor 1 at constant pressure and temperature.

Creep is a complex function of temperature, pressure, duration and, in the sensor case, possibly the diaphragm thickness as well. Even at the same temperature, the same sensor would experience a smaller cavity length change when subjected to a lower load or shorter period of time. Therefore, for different applications the sensor parameters can be optimized for the best performance. The most important of these parameters will most likely include the thickness of the diaphragm and the sensitivity of the sensor.

f) Temperature cross-sensitivity

Like other high-temperature pressure sensors, this sensor also exhibits temperature dependence. We already learned that the sensitivity is dependent on temperature. A second aspect, evident in Figure 3-24 and 3-25, is the drift of sensor's zero-point due to thermal dependence of cavity length.

Two factors were found to contribute to the cavity length increment with temperature. One is the thermal expansion of the cavity material and the other is the pressure change of the residual gas trapped inside the cavity during fabrication, denoted by ΔL_{mat} and ΔL_P , respectively, both of which increase as temperature rises. The total temperature-induced cavity length change is

$$\begin{aligned}\Delta L_T &= \Delta L_{mat} + \Delta L_P \\ &= \alpha L \Delta T + S_p \Delta p_{in}\end{aligned}\tag{3-17}$$

where α is the coefficient of thermal expansion (CTE) of fused silica, L is the cavity length, ΔT is the temperature change, S_p is the sensor's pressure sensitivity and Δp_{in} is the gas pressure change inside the cavity. Δp_{in} is further related to ΔT by the ideal gas law,

$$p_{in} V = N k T\tag{3-18}$$

where p is the gas pressure, V is the cavity volume, N is the number of molecules inside V , k is the Boltzmann constant and T is absolute temperature in Kelvin. Since ΔL is negligible

compared to L , the volume V remains roughly as a constant. With N also unchanged for a sealed cavity, let

$$\beta = Nk/V \quad (3-19)$$

denote a proportional constant. Then we have

$$p_{in} = \beta T \quad (3-20)$$

and

$$\Delta p_{in} = \beta \Delta T. \quad (3-21)$$

By substituting it into Eq. (3-17), we have

$$\begin{aligned} \Delta L_T &= \alpha L \Delta T + \beta S_p \Delta T \\ &= (\alpha L + \beta S_p) \Delta T \\ &\triangleq S_T \Delta T \end{aligned} \quad (3-22)$$

where S_T is defined as the temperature sensitivity of the sensor.

Measurements of L from 24°C to 513°C are plotted in Figure 3-30. Linearity is seen with fitted slope $S_T = 0.032 \text{ nm}/^\circ\text{C}$ and $0.025 \text{ nm}/^\circ\text{C}$ for sensor 1 and 2, respectively. This is because α is approximately a constant within this temperature range for fused silica, and L and S_p do not change much. Therefore S_T is about constant, leading to the linearity. With known values of L and S_p for both sensors, α and β can be solved as $0.98 \times 10^{-6} /^\circ\text{C}$ and $0.0095 \text{ psi}/^\circ\text{C}$. α is larger than the standard value for fused silica, $0.55 \times 10^{-6} /^\circ\text{C}$, partly as a result of residual doped core in the cavity which has a larger CTE. The effect of thermal expansion can be reduced by using a shorter cavity. From β , the pressure inside the cavity at RT can be derived as $p_{in,RT} = \beta T = 0.0095 \times 297 = 2.8 \text{ psi}$, about one fifth of room pressure (13.7psi), which is a clear indication that the amount of gas trapped inside the cavity is significantly reduced by the splicing arc.

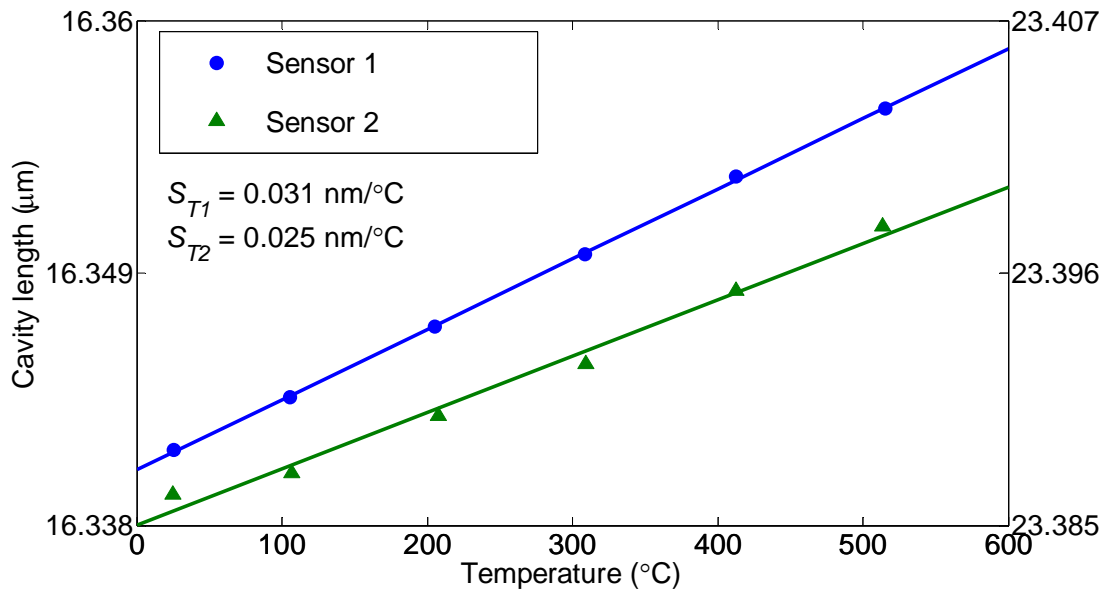


Figure 3-30. Airgap vs. temperature for both sensors.

Assuming the temperature of the arc is 1700°C, slightly higher than the softening point of fused silica, p_{in} is about 2psi by the ideal gas law, which is roughly the theoretical limit by fusion splicing. Optimization of the splicing parameters may allow this limit to be approached. If the sensor is to operate over a wide pressure range or a limited temperature range, the temperature cross-sensitivity is relatively reduced. Otherwise, temperature compensation is generally necessary, as with almost all types of high-temperature pressure sensors.

3.5 Dynamic Pressure Field Test

To further demonstrate the sensor's performance, it was field-tested in an aircraft engine (Garrette TF109 Turbofan Engine). The test was a collaborated effort between CPT and Virginia Tech's Department of Mechanical Engineering who maintains the engine at Virginia Tech

airport. The goal is to investigate sensor's high-frequency dynamic pressure response, along with its reliability and robustness for harsh environment operation.

The dynamic pressure could extend from a few kHz to more than a hundred kHz, reaching beyond the capability of spectrum-based whitelight detection which cannot follow such signal due to long processing time (a few milliseconds to seconds for spectrum capturing and signal demodulation). The best choice is intensity-based detection system, whose speed is only limited by the photodiode and other electronic devices, able to detect very high-frequency signal. In the field test, our system is self-calibrated interferometric intensity-based (SCIIB). Since its development is not the focus in this dissertation research, only the basic principle will be briefly introduced here.

3.5.1 Self-calibrated interferometric intensity-based (SCIIB) system [10]

The system diagram is shown in Figure 3-31. Light from a broadband source propagates through a circulator to the sensor head. The reflected signal is split into two channels by a coupler. The first channel has the same spectral distribution as the source, and hence named wideband channel. The second is further filtered by an inline bandpass filter, thereby named narrowband channel. The signal power of the two channels is then detected by photodiodes. Figure 3-31 also shows the simulated signals. For the wideband channel, when cavity length exceeds its coherent length, interference will diminish and its power tends to stabilize. The narrowband channel, however, possesses a much longer coherent length, which still generates an oscillating signal due to strong interference. This is where the sensor is set to work. So when the cavity length varies around its initial values, the narrowband signal will respond to the change, while wideband channel will remain stable, serving as an excellent power reference.

The system outputs the ratio of the two channels to cancel out power fluctuations from disturbance such as source drift and fiber bending, and is hence self-calibrated. Although SCIIB system does not have perfect linear response, it is advantageous in dynamic measurement with a much higher frequency response compared to the whitelight system. The non-linearity can be corrected by a calibration curve.

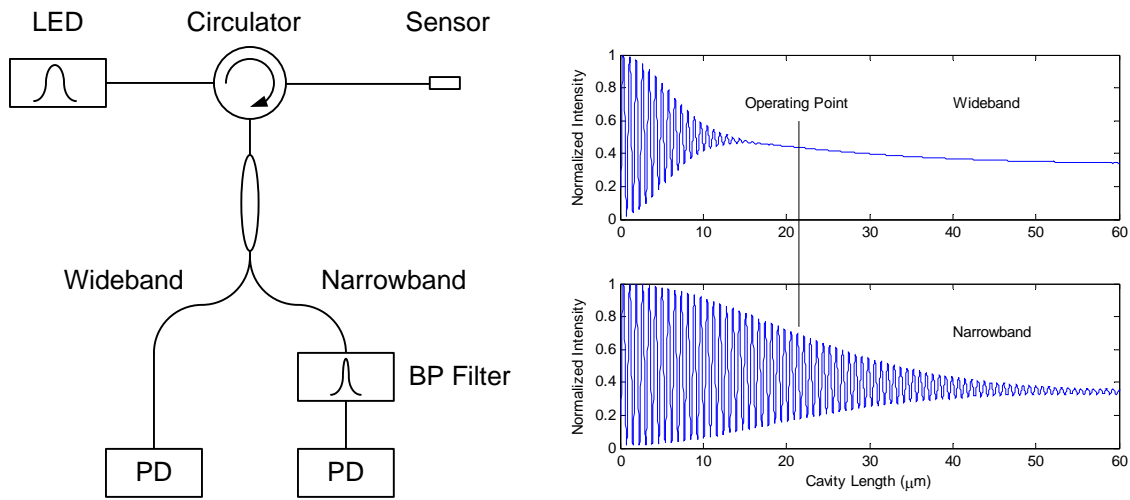


Figure 3-31. Schematic diagram of the SCIIB system (left); simulated wideband and narrowband signals (right).

3.5.2 Sensor packaging

For field applications, sensor packaging is necessary for installation and protection. Packaging of sensors is considered by many as the most challenging task in sensing product development. This is especially true for harsh environment applications. The schematic and photo of sensor package is shown in Figure 3-32. The body is a threaded stainless-steel fitting to be mounted on the engine. Inside the fitting is a metal ferrule, which in turn holds a glass ferrule. Both are for support and alignment of fibers. Sensors are inserted and bonded to the glass ferrule with 1mm protrusion outside the metal ferrule, leaving the entire sensor heads exposed. At the other end of the fitting, tubes are used for fiber tail protection. All these parts are epoxy-bonded together. The miniature size permits multiple sensors in one packaging.

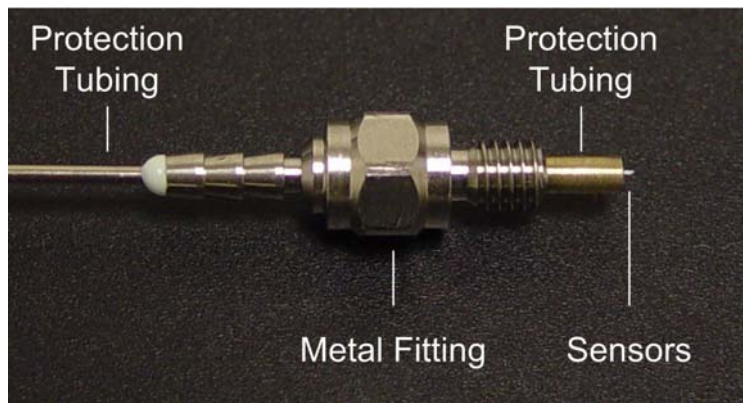
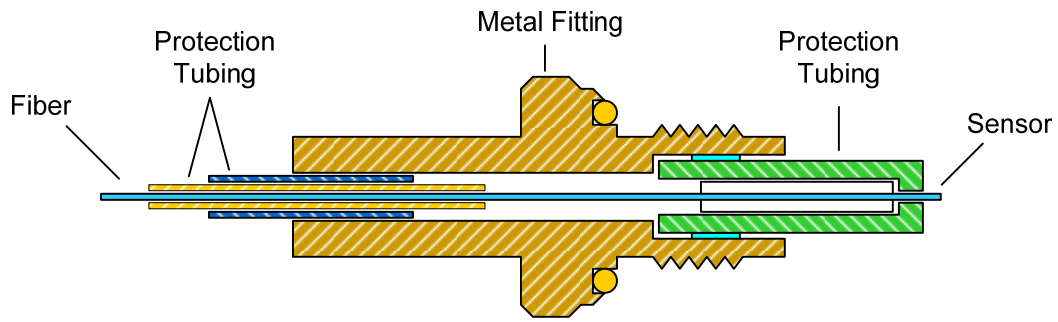


Figure 3-32. Schematic (top) and photo (bottom) of sensor packaging

Figure 3-33 shows the engine and how sensors were mounted on the side wall of its air intake. For pressure reference, a semiconductor Kullite sensor was mounted beside the miniature sensor. Details are further illustrated in Figure 3-34. Flush mount is not used as parts may fall into the engine under strong turbulence. Instead, a reduced opening is machined to allow only the sensors to go through but not the rest of the packaging.



Figure 3-33. Photos of engine with sensors mounted

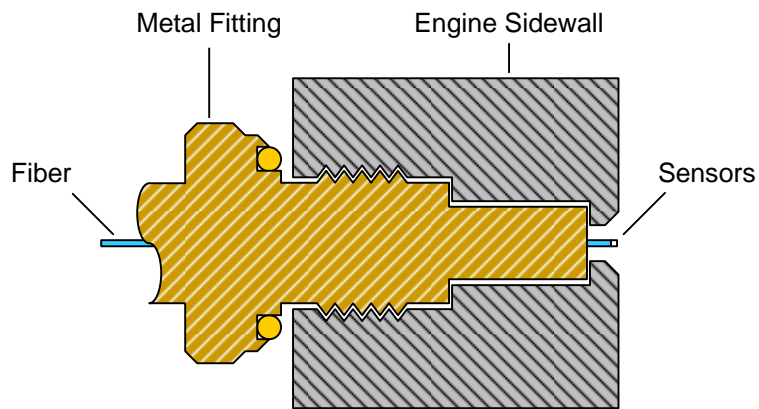


Figure 3-34. Sensor packaging on the side wall

3.5.3 Test Result

Figure 3-35 shows the dynamic outputs and their Fourier transform of both the miniature sensor and Kulite sensor, both resembling each other very well.

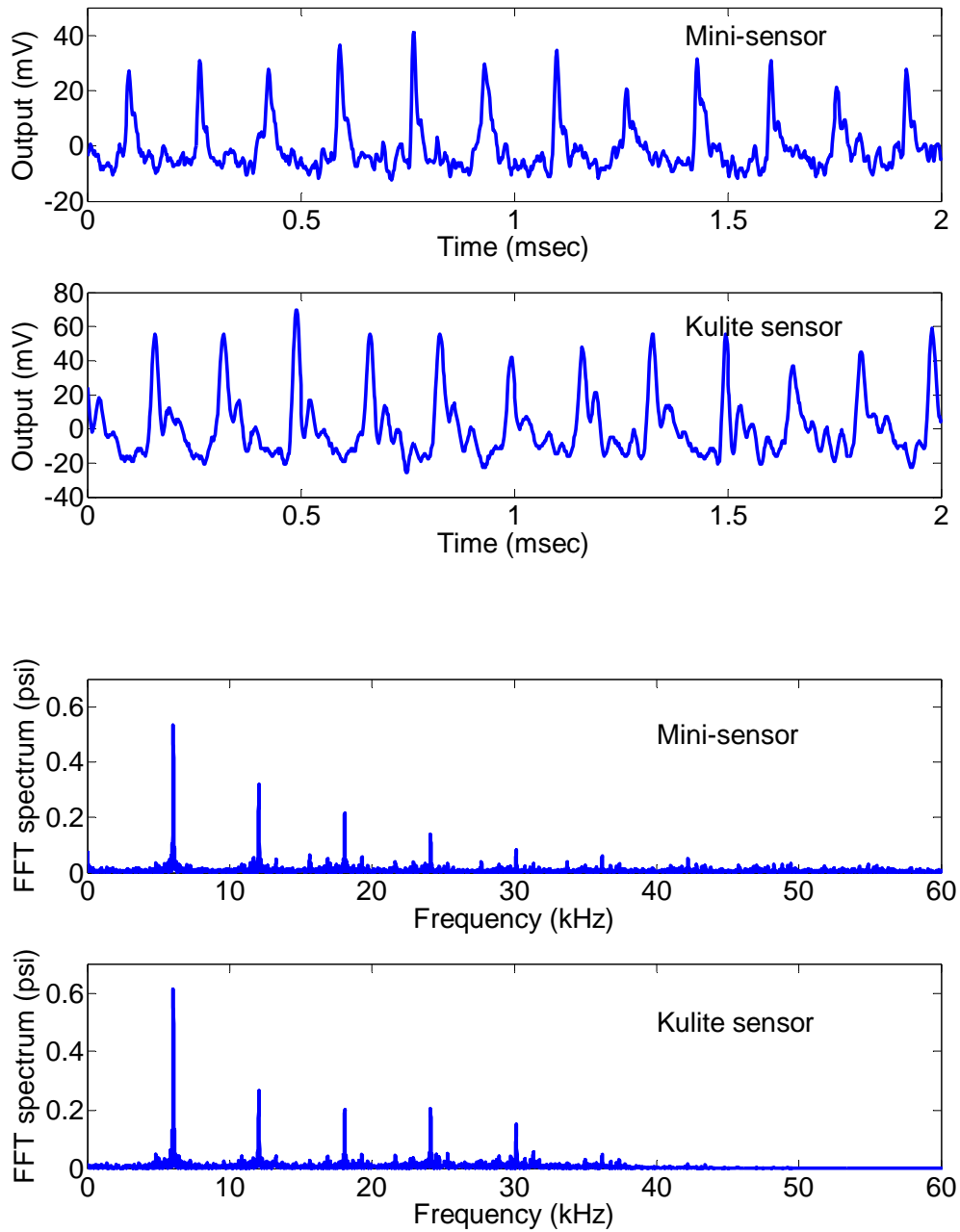


Figure 3-35. Mini-sensor output vs. Kulite sensor output. (top) Time domain signal; (bottom) FFT spectrum

Output voltages clearly show the pressure is periodic, causing by the blades passing by. The Kulite signal trailed the sensor signal because of different mounting position. The FFT reveals a series of harmonics. The frequency and amplitude of up to 6th harmonic for both sensors are listed in Table 3-1. The frequencies for both sensors match very well.

Table 3-1. Frequencies and amplitudes of output harmonics

Peak #	Frequency (kHz)		Amplitude (mV)	
	Mini-sensor	Kulite	Mini-sensor	Kulite
1	6.030	6.030	9.59	20.44
2	12.060	12.060	5.71	8.83
3	18.085	18.090	3.88	6.69
4	24.115	24.120	2.47	6.82
5	30.145	30.145	1.51	5.03
6	36.180	36.175	1.11	1.59

The miniature sensor's dynamic response was calibrated to be about 18 mV/psi. From Figure 3-35, the amplitude of the first harmonic measured by the sensor was about 9.59 mV. So the peak-to-peak pressure change is $2 \times 9.59 \text{ mV} / (18 \text{ mV/psi}) = 1.1 \text{ psi}$.

The Kulite sensor has a sensitivity of 33mV/psi. It measured a dynamic pressure change of 20.44mV in amplitude, which corresponds to a peak-to-peak pressure change of about $2 \times 20.44 \text{ mV} / (33 \text{ mV/psi}) = 1.2 \text{ psi}$.

3.6 Future work: Discussion and preliminary results

The miniature pressure sensor has been proven functional up to 700 °C in static pressure tests. Its dynamic capability and robustness were also demonstrated in engine field test. These are only the starting steps to explore this technology. Further research may reveal its potential for other applications. This section is dedicated to discuss how to improve the technique and how to apply it elsewhere. Specifically, the topic will focus on the sensor's temperature compensation and its biomedical applications. Both theoretical and experimental discussion are presented here as guidance to future research.

3.6.1 Temperature compensation:

Temperature sensitivity has been discussed previously in this chapter. Its impact is non-negligible, raising the question of how to compensate pressure reading for thermal drift. A feasible and effective solution is to integrate a fiber inline temperature sensor into the pressure sensor for simultaneous measurement of both temperature and pressure. This section discusses some preliminary theoretical and experimental results and outlines the future work.

(a). Miniature Temperature (T) and Pressure (P) sensor multiplexing (T+P)

For integration with the miniature pressure sensor, the temperature sensor needs to be equally small. The best approach is the fiber inline temperature sensor, namely intrinsic Fabry-Perot interferometric (IFPI) sensor, which creates multiple reflections within the fiber, in comparison to extrinsic Fabry-Perot interferometer (EFPI) which has such reflection only at the end or outside of the fiber.

Figure 3-36 shows the multiplexing scheme. The pressure sensor, given that the diaphragm is much thinner than the cavity, is simplified as having only two reflections, E_3 and E_4 , with a cavity length of L_2 . The temperature sensor has two reflecting surfaces as well, denoted as E_1 and E_2 and separated by a length of L_1 . It locates at a distance of d away from the pressure sensor.

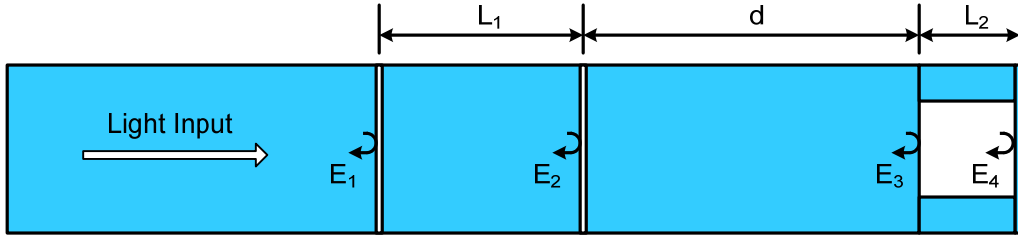


Figure 3-36. Scheme of sensor multiplexing

The total reflected light intensity can be written as follows:

$$\begin{aligned}
 I_{total} &= \left| A_1 + A_2 e^{-j\beta_1} + A_3 e^{-j(\beta_1+\beta_2)} + A_4 e^{-j(\beta_1+\beta_2+\beta_3)} \right|^2 \\
 &= \underbrace{\left[|A_1|^2 + |A_2|^2 + 2 \operatorname{Re}(A_1 A_2^* e^{j\beta_1}) \right]}_{R_1} + \underbrace{\left[|A_3|^2 + |A_4|^2 + 2 \operatorname{Re}(A_3 A_4^* e^{j\beta_2}) \right]}_{R_2} \\
 &\quad + \underbrace{\left\{ \left[A_1 A_3^* e^{j(\beta_1+\beta_2)} + A_1 A_4^* e^{j(\beta_1+\beta_2+\beta_3)} + A_2 A_3^* e^{j\beta_3} + A_2 A_4^* e^{j(\beta_2+\beta_3)} \right] + c.c. \right\}}_{R_{12}}
 \end{aligned} \tag{3-23}$$

where $A_1 \sim A_4$ are complex amplitudes, β_1 , β_2 , and β_3 are the phase shift determined by the cavity length L_1 , d , and L_2 as the following:

$$\beta_1 = \frac{4\pi L_1}{\lambda}, \beta_2 = \frac{4\pi L_2}{\lambda}, \beta_3 = \frac{4\pi d}{\lambda}. \tag{3-24}$$

and R_1 is the signal by the temperature sensor, R_2 is the signal by the pressure sensor, and R_{12} is the interference between surfaces of the temperature and pressure sensor. Each of these signals contains sinusoidal terms whose frequencies are determined by the d , L_1 , and L_2 . The larger the length, the higher the frequency.

R_1 , R_2 , and R_{12} can be readily separated digitally by filters if d , L_1 and L_2 are properly arranged. Given typical values of d , L_1 and L_2 , we would have $d \gg L_1 \gg L_2$, e.g., $d = 3\text{mm}$, $L_1 = 300\mu\text{m}$, and $L_2 = 30\mu\text{m}$. Therefore all terms in R_{12} will locate at higher frequency than R_1 and R_2 and not

interfere with them. To separate R_1 and R_2 , a band-pass filter will be necessary to filter the interference by L_1 as

$$I_{Temp} = 2 \operatorname{Re}(A_1 A_2^* e^{j\beta_1}) \quad (3-25)$$

It contains the temperature sensor signal only. Then a low-pass filter would generate the pressure sensor signal as follows

$$I_{Pressure} = \underbrace{|A_1|^2 + |A_2|^2}_{T \text{ sensor}} + \underbrace{|A_3|^2 + |A_4|^2 + 2 \operatorname{Re}(A_3 A_4^* e^{j\beta_2})}_{P \text{ sensor}} \quad (3-26)$$

Clearly, $I_{pressure}$ is a combination of both the interference from the pressure sensor and a background intensity ($A_1^2 + A_2^2$) from the temperature sensor. This is undesirable because signal change of the temperature sensor could possibly have an impact on the result of the pressure sensor, especially when T signal is stronger than P signal. However, further separation of Eq. (3-26) is impossible. A practical and effective solution would be to reduce the reflection of the T sensor and minimize its impact on the P sensor.

These analyses were further verified in preliminary experiments. Two temperature sensors, sT1 and sT2 with sT1 about 20dB higher in reflection than sT2 as plotted in Figure 3-37, were tested in conjunction with a pressure sensor sP whose spectrum is shown in Figure 3-38.

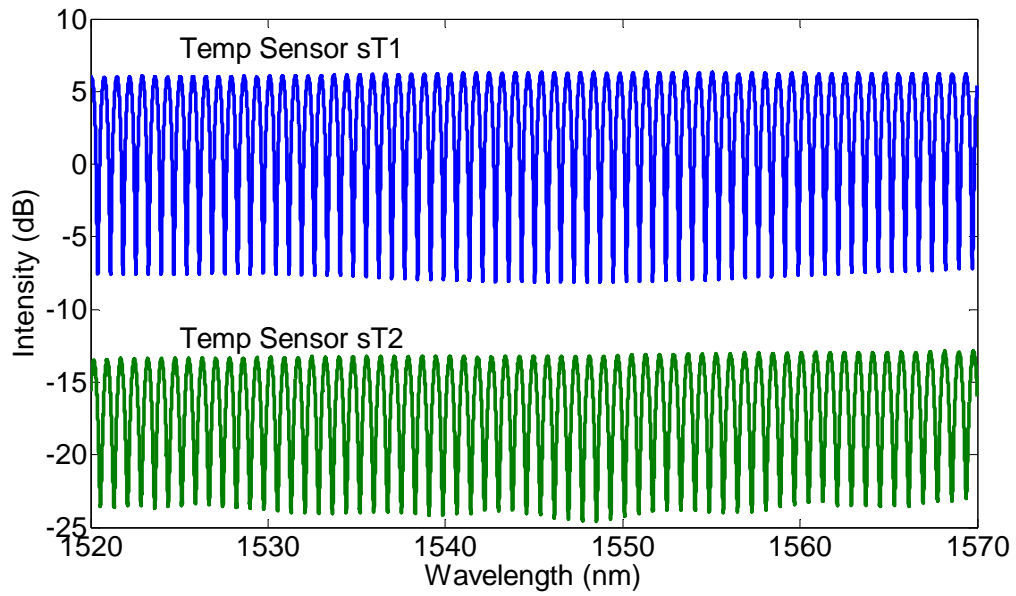


Figure 3-37. Spectra of temperature sensors sT1 and sT2

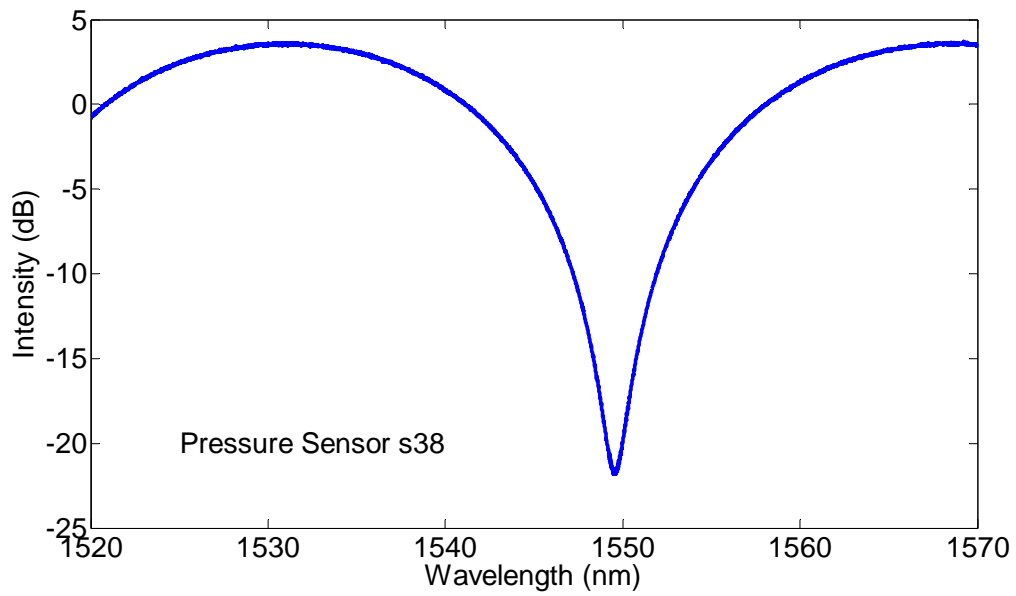


Figure 3-38. Spectrum of pressure sensor sP

The temperature and pressure sensors are spliced together with a large separation d . The spectra of $sT1 + sP$ and $sT2 + sP$ are shown in Figure 3-39 and 3-40, respectively. In Figure 3-39, the high-reflection $sT1$ dominates the spectrum while in Figure 3-40 sP is overwhelming. The latter is the preferred case as discussed previously.

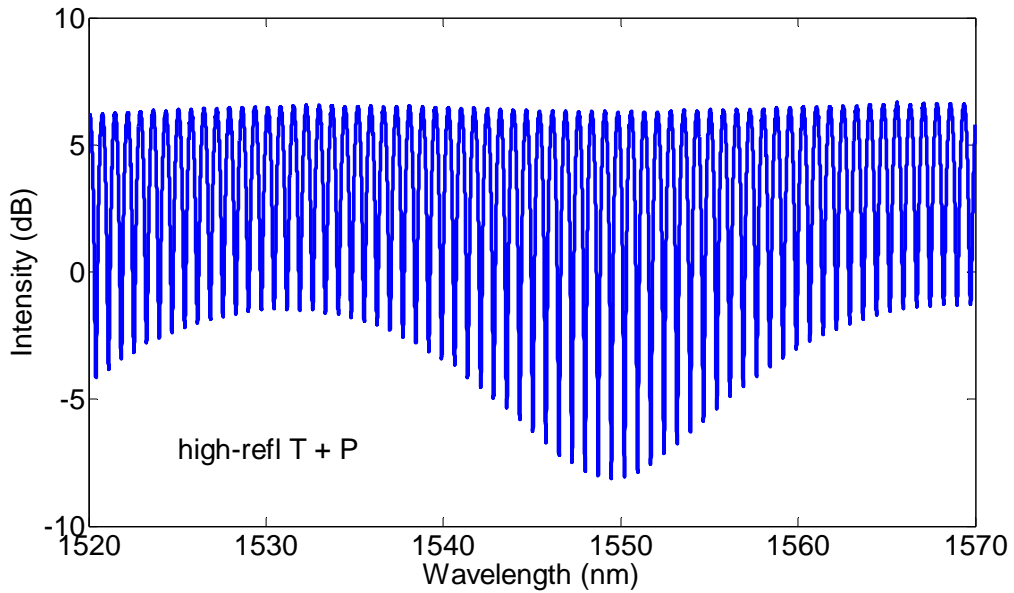


Figure 3-39. High reflection T sensor + P sensor

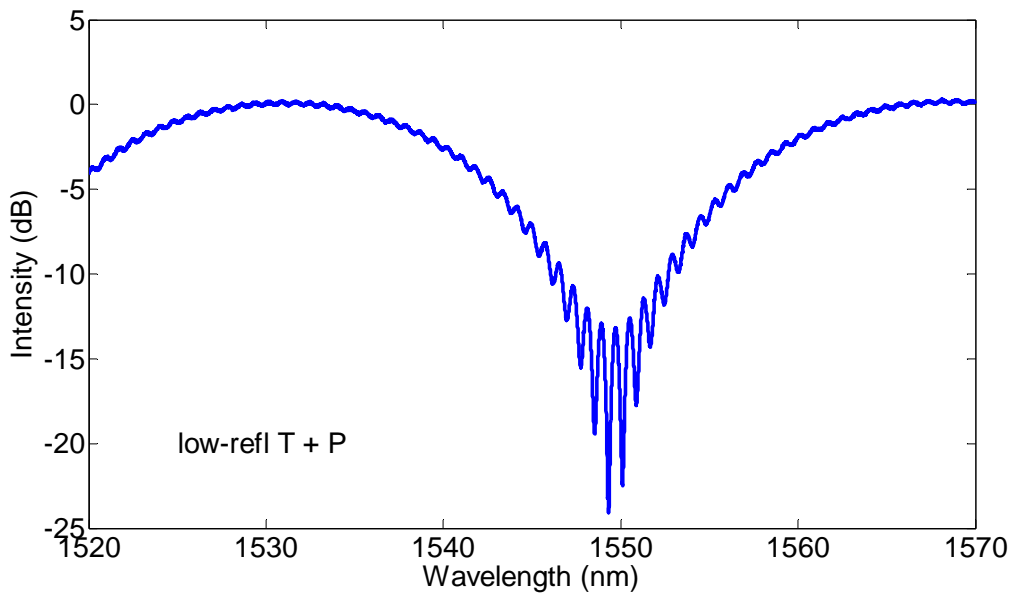


Figure 3-40. Low reflection $sT2 + sP$

These spectra were then processed using digital filters. Figure 3-41 and 3-42 plot the FFT of the spectra in Figure 3-39 and 3-40, respectively. Although seemingly the signal in Figure 3-41 is better than that in Figure 3-42, the latter will have less cross-sensitivity for both T and P sensors.

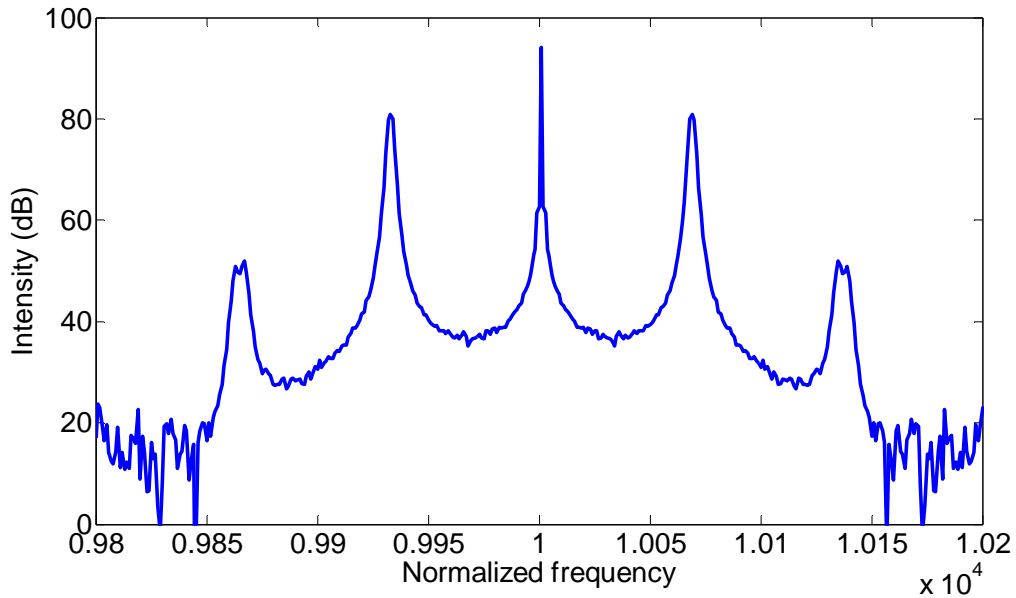


Figure 3-41. FFT of high reflection T + P

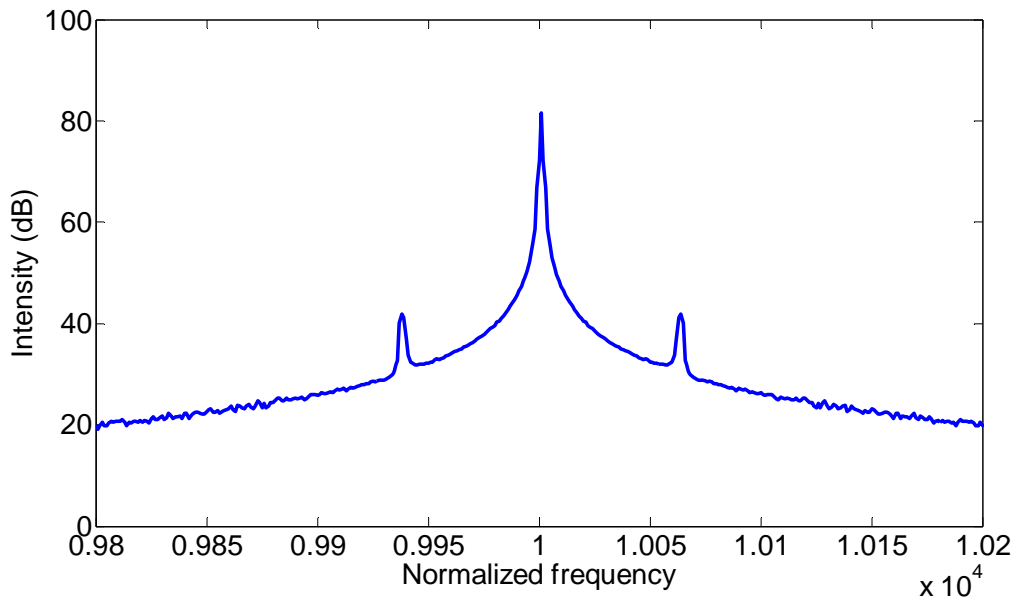


Figure 3-42. FFT of low reflection T + P

The signals for both T and P sensors can be extracted from these spectra. The T sensor signals can be separated from other signals very well without much interference. On the other hand, the P sensor signals, as shown in Figure 3-43 and 3-44, are different in term of the background they have from the T sensor.

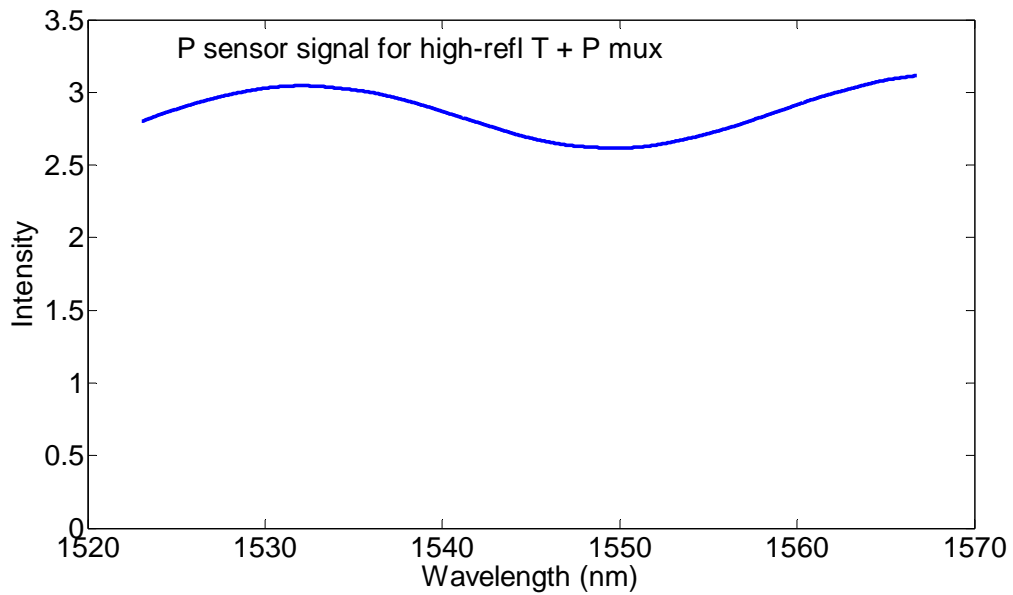


Figure 3-43. Spectra of temperature sensors

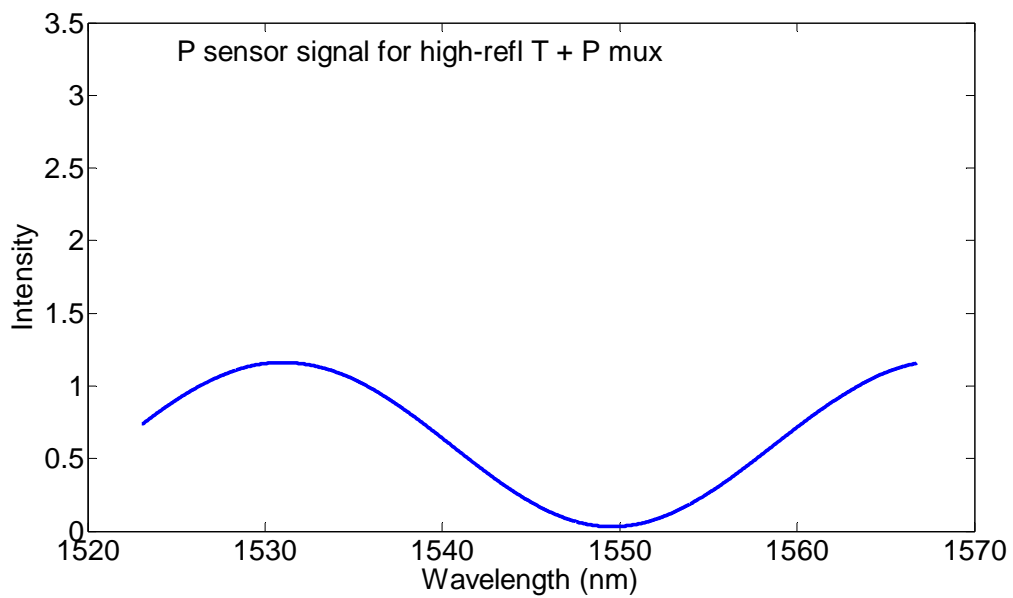


Figure 3-44. Spectrum of pressure sensor

The results verified the previous theoretical calculation that high reflection temperature sensor will have more impact on the pressure sensor signal and therefore is a less preferred approach.

To continue the study, the following tasks will be finished:

- Implement algorithms to separate the sensor signals and calculate the cavity length for each sensor.
- Fabricate the multiplexed temperature and pressure sensors.
- Test the performance for each sensor at different pressures and temperatures.
- Analyze the thermal-compensation capability of this multiplexed scheme.

3.6.2 Biomedical Application

Other than high-temperature harsh environment, size advantage also fit the miniature sensor very well into biomedical applications, where minimally invasive pressure measurement is often desired, such as in vivo blood measurement. This section reviews related issues, discusses solutions and presents preliminary results.

a). Background

Invasive pressure measurements have become increasingly important in biomedical applications and offer the potential for significant patient benefits by providing physicians with real-time information to improve the safety of surgical procedures and assist in timely diagnosis and treatment. Accurate and disposable sensors are needed for applications such as monitoring of arterial or venous pressure, intracranial pressure measurements, balloon angioplasty and numerous others.

Reliable methods are currently lacking for continuous pressure monitoring. At present, a typical physiologic pressure monitoring system includes an intravascular catheter, a liquid-filled tubing system to transmit pressure waves, and an external pressure transducer to convert the information into an electrical signal. The accuracy of such measurements is dependent on the response of the liquid system, the accuracy and frequency response of the transducer, and proper system leveling and zeroing. Hydrostatic leveling to negate the effect of the fluid weight in the tubing is

generally performed by eye, using a carpenter's level, or a laser leveling devices, and can result in significant errors [11]. Additional errors can be introduced by the liquid-filled tubing system. The length of the catheters severely limits the time response for such sensors due to fluid inertia. Accuracy is also degraded by mechanical instability along the catheter and recalibration is needed before each measurement. Commonly, the administration of medications, many of which have a critical impact on blood pressure, requires the blood pressure monitoring system to be disconnected. In addition, its bulky size makes it difficult to apply in small blood vessels or newborns.

Sensor miniaturization will permit in situ measurement and implantable measurement capability for a multitude of clinical sensing requirements, greatly simplifying the mechanical setup by eliminating the need for a liquid column and its associated problems. Direct measurement of pressure at discrete in vivo sites will greatly improve response time and accuracy. Such sensors must clearly be biocompatible and miniaturized, both to fit within a catheter and to minimize the impact of the sensor itself on the pressure measurement.

b). Miniature pressure sensor for biomedical applications

Significant effort has been exerted to fabricate miniature sensors, primarily utilizing microelectromechanical systems (MEMS)[12-14] and optical fiber.

Various MEMS sensing mechanisms have been proposed using capacitive[15-17], piezoresistive [18-20] and optical[21-23] detection. These sensors are suitable for mass production. However, their resolution and accuracy are relatively low compared to fiber optic sensors. In addition, materials for MEMS are mostly bio-incompatible. A number of MEMS sensors have been commercialized for medical applications, yet very few are available for in vivo pressure measurement[24-26]. Most are only to replace the external pressure sensors in the old-fashioned tube-based measurement. That is, the pressure is still transmitted out through catheter liquid column with these cheap and disposable sensors for measurements outside the body.

Relatively few fiber-optic sensors with miniature size have been reported in literature, yet providing attractive alternatives for invasive measurement. The small size and excellent flexibility of the miniature pressure sensor makes it very well suited for catheter-based in-vivo monitoring. Compared to other published results, the sensor described here bears the smallest size. The transducer fits easily through 24 and 26 gauge intravenous catheters (Figure 3-45). Optical fibers are nontoxic, chemically inert, can easily be coated for biocompatibility, and do not suffer from electromagnetic interference (EMI), which will be critical for patient monitoring applications. In addition, fiber optic interferometric techniques offer very high resolution and accuracy.

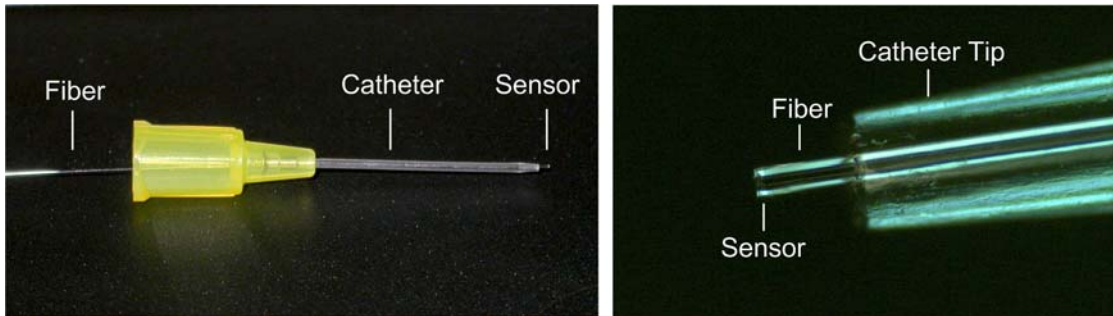


Figure 3-45. Insertion of fiber pressure sensor through a 24 gauge intravenous catheter (left); close-up of fiber protruding from catheter tip (right).

c) Sensing in a fluid

Effect of increased fluid viscosity

When a sensor is immersed in liquid, the diaphragm's vibration characteristics will be significantly altered. Since any movement of the diaphragm will entrain the liquid in contact with it, this entrainment of the liquid effectively constitute extra mass to the diaphragm, called added mass or virtual mass [7]. This added mass, m_a , will increase the parameter m in Eq. (3-11), consequently reducing the ω_n of the diaphragm. Let $m_a = \beta m$, then the altered natural frequency has the form [6]

$$\omega_n' = \frac{\omega_n}{\sqrt{1+\beta}} \quad (3-27)$$

β is a mode-related constant. For fundamental mode, $\beta = 0.669 \frac{\rho_L R}{\rho h}$, where ρ_L is the density of the liquid. Since $\rho_L \approx 1.05 \text{ g/cm}^3$ for human blood [27], $\beta \approx 5.27$, i.e, the added mass is more than five times the effective mass of the diaphragm. Therefore the diaphragm with parameters given above will have a reduced natural frequency $\omega_n' = 0.4\omega_n$ and $f_n' = 2 \text{ MHz}$. This is still extremely high compared to the frequency of the pressure seen in blood vessels, which is usually a mere several Hz. Hence the frequency response will almost remain unchanged.

The effect of fluid viscosity is to add an extra term in the damping factor c in Eq. (3-9), which determines the peak width and only has small impact on the natural frequency. As can be seen from Figure 3-20, this factor will change the peak height and width but will not change the response at very low frequency.

Effect of deposition on the diaphragm

The effect of the deposition on the diaphragm is also to increase its effective mass. Assume this extra mass is five times the diaphragm mass (this is a large deposition), plus the added mass by the liquid ambient, this will give $\omega_n' = 0.3\omega_n$ and $f_n' = 1.5 \text{ MHz}$. Therefore the deposition will not significantly alter the sensor response, either.

Though this is a much simplified model, it still can reveal some very important aspects of the system behavior. Based on these semi-quantitative analysis, we can expect minimal impact of the fluid, its viscosity and deposition on the performance of the sensor.

Temperature cross-sensitivity

In Figure 3-30 the temperature sensitivity of sensor 1 is $0.031\text{nm}/^\circ\text{C}$. The sensor's pressure sensitivity is $1.56\text{nm}/\text{psi}$. For a 300mm Hg (5.8 psi) pressure change, the pressure-induced cavity length change is $1.56*5.8 = 9.05\text{ nm}$.

Human body temperature will fluctuate. If, for the same patient during one measurement, the body temperature variation is 2°C , the total temperature-induced cavity length change is $0.032*2 = 0.064\text{ nm}$. This corresponds to about $0.064\text{nm}/9.05\text{nm} = 0.71\%$ full scale change or 2.1mm Hg . If the actual body temperature variation during one measurement is less than 2°C , we will expect to see better results.

Temperature variation from patient to patient will be larger. In this case, a calibration curve (cavity length vs. pressure) can be obtained at a specific temperature (e.g. 37°C) and then for each patient a correction factor based-on sensor's temperature sensitivity and the patient's own temperature can be added for compensation. High accuracy and resolution can be achieved this way.

Sensor's temperature sensitivity depends on the thermal expansion of the material, cavity length and the amount of residual air inside the cavity. One important topic here related to the sensor fabrication is to study the optimized splicing parameters to reduce the residual air. Other means such as reducing the cavity length and increasing the pressure sensitivity will also help.

Sensor isolation coating

A metal coating will optically isolate the sensor from ambient while maintaining good interference fringes. Figure 3-46 shows a sensor's spectrum from 1300nm to 1700nm as well as a simulated spectrum when it is coated with Titanium (Ti) thin film on the outer surface of the diaphragm. Parameters at silica/Ti interface, namely the reflectance and the phase with respect to

wavelength, are calculated by thin film software Essential Macleod. After the coating, the signal level is significantly raised. Meanwhile, the interference is still very good.

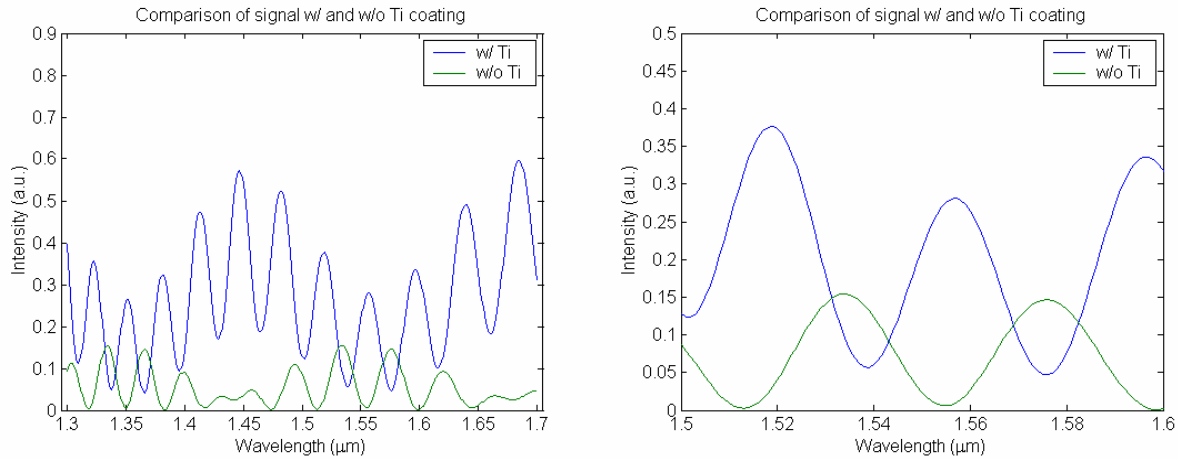


Figure 3-46. Sensor signal with and without a Ti coating, full spectrum (left); spectral range of interest (right).

3.7 Conclusion and Discussion

In this chapter, we have demonstrated the high-temperature operation of a miniature fiber-optic pressure sensor up to 710°C. Pressure-induced cavity length change was accurately determined by tracing the spectrum shift. Sensor performance was analyzed in detail and is very promising for various high-temperature applications. Field test results in a jet engine was presented and analyzed. Also discussed are the future directions of research and the sensor’s potential applications in other fields.

Future improvement is possible for the fabrication process. The fibers used are not optimized but chosen for their availability. Rather than graded index 62.5 μm fiber, step-index would be preferred, with a higher dopant concentration for faster etching. The fluorine-doped 105 μm fiber could be replaced by a 125 μm fused silica fiber rod.

3.8 References

- [1] T. Katsumata, Y. Haga, K. Minami, and M. Esashi, "Micromachined 125 μm diameter ultra miniature fiber-optic pressure sensor for catheter," *Trans. IEE Jpn., Part E*, vol. 120-E, pp. 58-63, 2000.
- [2] E. Cibula, D. Donlagic, and C. Stropnik, "Miniature fiber optic pressure sensor for medical applications," in *Proc. of IEEE Sensors 2002, First IEEE Int. Conf. on Sensors*, Piscataway, NJ, 2002, vol. 1, pp.711-714.
- [3] D. C. Abeysinghe, S. Dasgupta, J. T. Boyd, and H. E. Jackson, "A novel MEMS pressure sensor fabricated on a optical fiber," *IEEE Photon. Technol. Lett.*, vol. 13, pp. 993-995, Sep. 2001.
- [4] T. Pangaribuan, K. Yamada, S. Jiang, H. Ohsawa, and M. Ohtsu, "Reproducible fabrication technique of nanometric tip diameter fibre probe for photon scanning tunneling microscope," *Jpn. J. Appl. Phys.*, vol. 31, pp. 1302-1304, 1992.
- [5] E. Cibula, D. Donlagic, and C. Stropnik, "Miniature fiber optic pressure sensor for medical applications," in *Proc. of IEEE Sensors 2002, First IEEE Int. Conf. on Sensors*, Piscataway, NJ, 2002, vol. 1, pp.711-714.
- [6] M. Di Giovanni, *Flat and corrugated diaphragm design handbook*. New York: M. Dekker, 1982.
- [7] C.M. Harris, and A.G. Piersol, *Harris' Shock And Vibration Handbook* (McGraw-Hill, New York, 2002).
- [8] B. Qi, G. R. Pickrell, J. Xu, P. Zhang, Y. Duan, W. Peng, et al., "Novel data processing techniques for dispersive white light interferometer," *Opt. Eng.*, vol. 42, pp. 3165-3171, 2003.
- [9] M. Fukuhara, and A. Sanpei, "High temperature-elastic moduli and internal dilational and shear frictions of fused quartz," *Jpn. J. Appl. Phys.*, vol. 33, pp. 2890-2893, 1992.
- [10] A. Wang, H. Xiao, J. Wang, Z. Wang, W. Zhao, and R. G. May, "Self-calibrated interferometric-intensity-based optical fiber sensors," *J. Lightwave Technol.*, vol. 19, pp. 1495-1501, 2001.
- [11] W.P. Rice, E. G. Fernandez, D. Jarog and A. Jensen, "A Comparison of Hydrostatic Leveling Methods in Invasive Pressure Monitoring", *Critical Care Nurse* **20** (2000)

- [12] M. Esashi, MEMS technology: optical application, medical application and SOC application, Symposium On VLSI Technology Digest of Technical Papers pp. 6-9 (2002).
- [13] N. Maluf, D. Gee, K. Petersen and G. Kovacs, Medical applications of MEMS, Wescon Conference Record 1995, 95CB35791 Los Angeles, CA, pp. 300-306 (1995).
- [14] Y. Haga, T. Mineta and M. Esashi, Active catheter, active guide wire and related sensor systems, Robotics, Manufacturing, Automation and Control. Vol.14. Proceedings of the Fifth Biannual World Automation Congress (WAC 2002) ISORA 2002, ISIAC 2002 and ISOMA 2002 pp. 291-6 (2002).
- [15] D. Goustouridis, P. Normand and D. Tsoukalas, "Ultraminiature silicon capacitive pressure-sensing elements obtained by silicon fusion bonding", Sensors and Actuators A, A68 269-274 (1998).
- [16] C. Hierold, B. Clasbrummel and D. Behrend, "Low power integrated pressure sensor system for medical applications", Sensors and Actuators A, 73 58-67 (1999).
- [17] S. Chatzandroulis, D. Goustouridis, P. Normand and D. Tsoukalas, "A solid-state pressure-sensing microsystem for biomedical applications", Sensors and Actuators A, 62 551-555 (1997).
- [18] P. Melvås, E. Kälvesten, P. Enoksson and G. Stemme, "A free-hanging strain-gauge for ultraminiaturized pressure sensors", Sensors and Actuators A 97-98 75-82 (2002).
- [19] J. Goosen, D. Tanase and P. French, Silicon sensors for use in catheters, Proceedings of 1st Annual International IEEE-EMBS special topic conference on microtechnologies in medicine & biology, pp. 152-155.
- [20] P. Melvås, E. Kälvesten and G. Stemme, "Media protected surface micromachined leverage beam pressure sensor", J. Micromech. Microeng. 11 617-622 (2001).
- [21] T. Katsumata, Y. Haga, K. Minami and M. Esashi, "Micromachined 125 μ m diameter ultra miniature fiber-optic pressure sensor for catheter", Trans. Inst. Electrical Eng. Jpn. Part E 120E 58-63 (2000).
- [22] D. Abeysinghe, S. Dasgupta, J. Boyd and H. Jackson, "A novel MEMS pressure sensor fabricated on a optical fiber", IEEE Photon. Technol. Lett. 13 993-995 (2001).
- [23] S. Dasgupta, J. Zhou and J. Wolff, "Design and fabrication of optical-MEMS pressure sensor arrays", Proceedings of SPIE on MOEMS and Miniaturized Systems 372-378 (2000).
- [24] <http://www.millarinstruments.com>
- [25] <http://www.adinstruments.com/products/datasheets/MLT0380.pdf>
- [26] <http://www.rjcenterprises.net/HTML/sysspec2.htm>
- [27] H.G. Hinghofer-Szalkay, and J.E. Greenleaf, "Continuous monitoring of blood volume changes in humans," J. Appl. Physiol. **63** 1003-1007 (1987)

CHAPTER 4

Sapphire-Wafer-Based Temperature Sensor

In previous chapter, the all-fused-silica pressure sensor has been demonstrated operable up to 700 °C. To reach even higher temperature, single crystal sapphire is the best option, as explained in Chapter 1. In this chapter, we will focus on the design and fabrication of temperature sensors for ultra-high temperature range, as well as its field application for harsh environment. The sensor is fabricated with a single-crystal sapphire fiber as the lightguide and a sapphire wafer as the sensing element. Temperature is determined by measuring the thermal dependence of the wafer's optical thickness using white-light interferometry. A prototype sensor was tested to 1600°C, demonstrating excellent repeatability. An accuracy of $\pm 0.2\%$ full scale was achieved. Besides, the sensors and the system were field-tested inside a burning coal gasifier in a Florida power plant and have continued to operate for as long as 7 months, proving its robustness and reliability for harsh environments. The sensor is simple, small and flexible, with advantages of batch fabrication and easy calibration

This chapter is organized as follows. Section 4.1 introduces the background of high-temperature temperature sensing and the design concept. Section 4.2 discussed the sensor fabrication techniques. System setup and signal analysis are presented in Section 4.3 and 4.4, respectively. In Section 4.5 its laboratory high-temperature performance is investigated. The preparation and results of the field tests are given in Section 4.6. Summary can be found in section 4.7.

4.1 Background of high-temperature temperature sensing

Over the past two decades, fiber-optic high-temperature sensors have seen many applications in a wide range of industries. Numerous schemes have been proposed based on various technologies, as introduced in Chapter 1. While silica-fiber-based temperature sensors usually cannot exceed 1000°C due to degraded mechanical strength and the thermal diffusion of the germanium dopant [1], crystalline optical fibers have received extensive attention, owing to their compact size and excellent mechanical and optical properties at elevated temperature. Among all of them, only single-crystal sapphire fiber is commercially available and has been used and researched extensively. In addition, sapphire is highly corrosion-resistant and chemically inert. However, the following technical difficulties have prevented its wide application for temperature sensing.

D1) Weak interference signal

Sapphire fiber is highly multimode due to its large diameter and numerical aperture (NA), and interferometric sensors made by MM fibers are extremely difficult to generate good interference signals, which are very sensitive to the smoothness, the flatness, the distance and especially the parallelism of the two interfering surfaces [2]. It was reported an angle on the order of 10^{-2} degree could significantly reduce the fringe quality [3].

D2) Difficult system integration

There have been no fiber-optic components made from sapphire fibers. All of them, such as light source, coupler, filter and circulator, are based on silica fibers. To be functional, sapphire-fiber-based sensors have to be integrated into silica-fiber-based systems. Some use focusing lens to guide light into and out of the sapphire fiber. Another scheme is to splice the sapphire fiber to a silica fiber with low temperature glass [4]. However, none of them have proved optically effective in terms of light coupling efficiency, and their robustness has not demonstrated for field operation.

Similar to what we did with the miniature pressure sensor, we again start the design by trying to solve these difficulties.

- S1). Use high-quality and highly parallel surfaces for the Fabry-Perot cavity. This will solve D1.
- S2). Develop a robust, effective coupling scheme between silica and sapphire fibers.

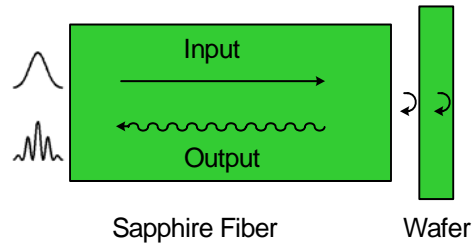


Figure 4-1. Wafer-based interferometric sensing structure

To meet S1, a well-polished wafer seems the best solution, as shown in Fig 4-1, and a piece of sapphire wafer will be compatible with high-temperature applications. Since high surface quality and excellent parallelism can be readily achieved in the wafer lapping/polishing industry, interference fringes can be easily generated even for highly multimode sapphire fiber.

To have the desired coupling in S2, experience in miniature sensor fabrication, particularly special splicing, provides helpful design insight, as discussed later in the chapter.

4.2 Sensor Fabrication

4.2.1 Materials

To reduce the above concept into practice, necessary materials include single-crystal sapphire fiber, sapphire wafer, a support to hold them together, and proper adhesives as well.

Optical-grade sapphire fibers have been commercially available for more than ten years, grown either by Edge-define Film-fed Grown (EFG) method or Laser Heated Pedestal Growth (LHPG) method. LHPG sapphire fibers are generally considered of better optical quality than EFG fibers. A number of publications have been generated on manufacture and characterization of sapphire fibers [5-6].

Unsuitable for mass production, sapphire fiber costs much more than silica fiber. It exhibits greater loss (1~10 dB/m) as well, even within its optical transmission window (0.5 ~3.5 μ m). Diameter as thin as 60 μ m with length up to 2 meters can be manufactured. And most of them are C-cut, i.e., the C-axis is along the fiber length. Grown as very thin and long rod with a refractive index around 1.76, sapphire fiber has no cladding, allowing a large modal volume. It has a hexagonal shape, reflecting sapphire's crystalline structure. Optically polished sapphire wafers, with C-plane, A-plane or R-plane orientation, are more readily available as commercial product.

Holding the fiber and the wafer together requires a mechanical support which can withstand high-temperature operation. An ideal choice would be a high purity alumina (99.8%) tube with 0.71mm OD and 0.13mm ID. High-temperature alumina-based adhesive was applied for bonding these parts.

4.2.2 Fabrication

The sensor head configuration is schematically shown in Figure 4-2. A 59 μ m-thick C-plane sapphire wafer of 1mm \times 1mm size is placed in front of a 15cm-long 75 μ m-diameter C-cut sapphire fiber, both bonded to a 99.8% alumina tube (OD: 0.71mm) and high-temperature adhesive. The C-plane wafer is to avoid birefringence. The sapphire fiber is angle-polished to prevent multi-beam interference. Its length can vary for different applications. Longer fiber will suffer higher loss and has to be carefully accounted for in power budget.

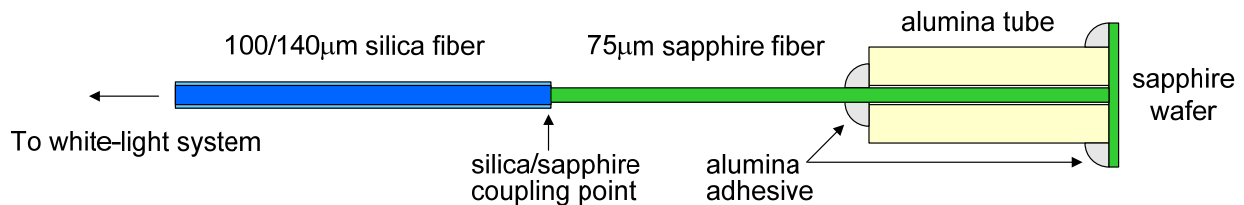


Figure 4-2. Sensor head structure

4.2.3 Fusion splice

The coupling between the silica and sapphire fibers was made through arc fusion splicing, inspired by experience in miniature sensor fabrication. Different from the previously reported splice based on aluminosilicate glass as interlayer [4], it is adhesive-free, originated from the fact that Ge-doped core of the silica fiber softens at a much lower temperature than the undoped cladding, something similar to the difference between Borosilicate glass and fused silica glass. Under carefully controlled arc duration and power, the core will turn viscous while the cladding, as well as the sapphire fiber, will remain solid. Prior to arcing, the sapphire fiber is brought to close proximity of the silica fiber. Both are then heated by the spark, and sapphire fiber will elongate for its large thermal expansion, resulting in a protrusion into the silica fiber's molten core to make the connection. Multiple arc strikes may be necessary depending on its power and duration.

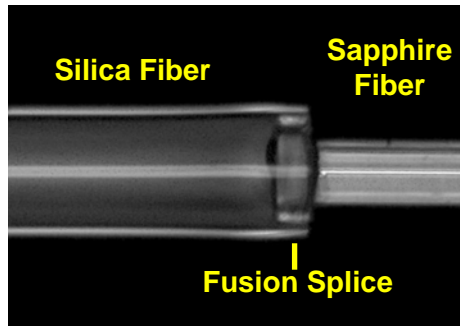


Figure 4-3. Fusion splice between silica fiber and sapphire fiber

In Figure 4-3, the splice joints a 100/140 μm silica fiber and a 75 μm sapphire fiber. Figure 4-4 plots the reflected power against the number of arcs. The power is mainly from two sources, the reflection from the coupling point, r_{couple} and the reflected signal from the sapphire fiber end, r_{signal} . The power first drops and then stabilizes with more arcs. In Figure 4-4, a total of 5dB loss was recorded for entire process, much of which, however, comes from the decrease of r_{couple} . This is because the initial contact of silica and sapphire is not complete under low arc power and duration, which leaves small high-reflecting air bubbles during the first few strikes. As the arcing continues, the air will be driven out to let the two fibers come into better physical contact, which

reduces and stabilizes the reflection. Since r_{couple} can be removed by signal processing, its absolute amplitude is not critical. Of more importance is the loss of r_{signal} , which will partially determine the signal-to-noise ratio. To measure the loss, the intensity differential of r_{signal} , Δr_{signal} , is measured before and after immersing the sapphire fiber end into an index matching oil ($n = 1.522$). Δr_{signal} is proportional to r_{signal} by a constant factor k , i.e. $\Delta r_{\text{signal}} = k r_{\text{signal}}$. k is decided by refractive indices of the sapphire fiber, the matching oil and air. By comparing Δr_{signal} before and after the splice, power loss as low as 0.5dB has been measured and can be regularly achieved. Further reduction of loss is limited by the deformation of the 100/140 μm fiber which may scatter the light out of the coupling point. This method eliminates the use of adhesives to produce a clean, simple and robust joint.

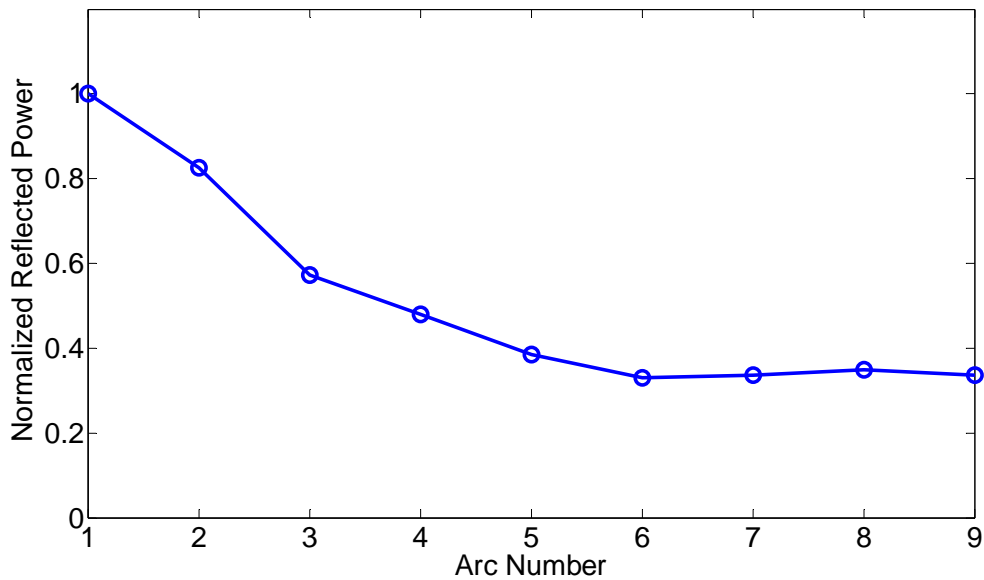


Figure 4-4. Reflected power vs. number of arcs

It is also successful splicing 100- μm diameter sapphire fibers but fails for larger ones due to the apparent silica fiber core size limitation.

4.3 Interrogation System and signal processing

4.3.1 White-light based interrogation system

The sensor is interrogated by a conventional spectrum-domain white-light system, as in Figure 4-5. Light from an 850nm LED is launched into the 100/140μm multimode (MM) fiber and propagates to the sensor head through a 3dB coupler. The sapphire fiber is fusion-spliced to the 100/140μm fiber. Interference spectrum generated by wafer returns to be detected by a miniature spectrometer (OceanOptics Inc., USB2000).

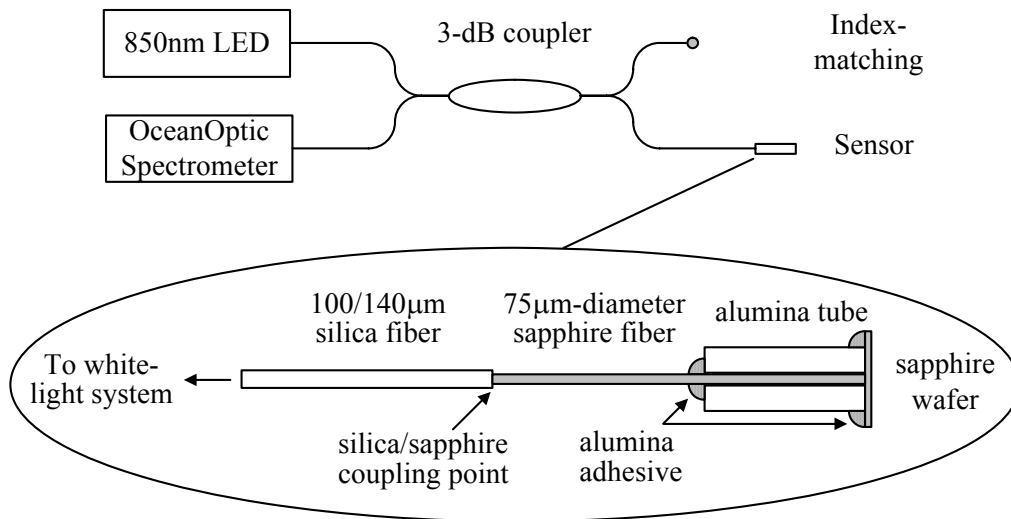


Figure 4-5. Schematic of the sensor and the system

4.3.2 Signal Processing

The total intensity of light received at the spectrometer can be written as

$$\begin{aligned}
 I_{total}(\lambda) = & I_B(\lambda) + I_D(\lambda) + I_{LED}(\lambda)(r_{couple} + r_{end}) \\
 & + I_{LED}(\lambda) \left[r_{s1} + r_{s2} - 2V\sqrt{r_{s1}r_{s2}} \cos \frac{2n(T)d(T)}{\lambda} \right]
 \end{aligned}
 \tag{4-1}$$

where $I_B(\lambda)$, $I_D(\lambda)$ and $I_{LED}(\lambda)$ are the intensity of the blackbody radiation, the dark current of the spectrometer and the LED, respectively, r_{couple} , r_{end} , r_{s1} and r_{s2} are reflectance at each of the following surface along the path: the silica/sapphire fiber coupling point, the end face of the sapphire fiber, the first and second surfaces of the sapphire wafer, respectively, n is the refractive index of sapphire, d is the thickness of the wafer, V is the fringe visibility, λ is the wavelength and T is the temperature.

In Eq. 4-1, it assumed that there is no interference between the sapphire fiber end and the wafer. This is sometimes found not true especially when the fiber end is polished perpendicular to the axis and parallel to the wafer. The distorted spectrum can cause signal processing difficulty but can be completely avoid by angle-polishing the fiber by about 1.5 degree. Figure 4-6 shows normal spectra at 25°C and 1597°C. The background intensity is significantly raised at 1597°C by the blackbody radiation, which is emitted or collected by the sapphire fiber.

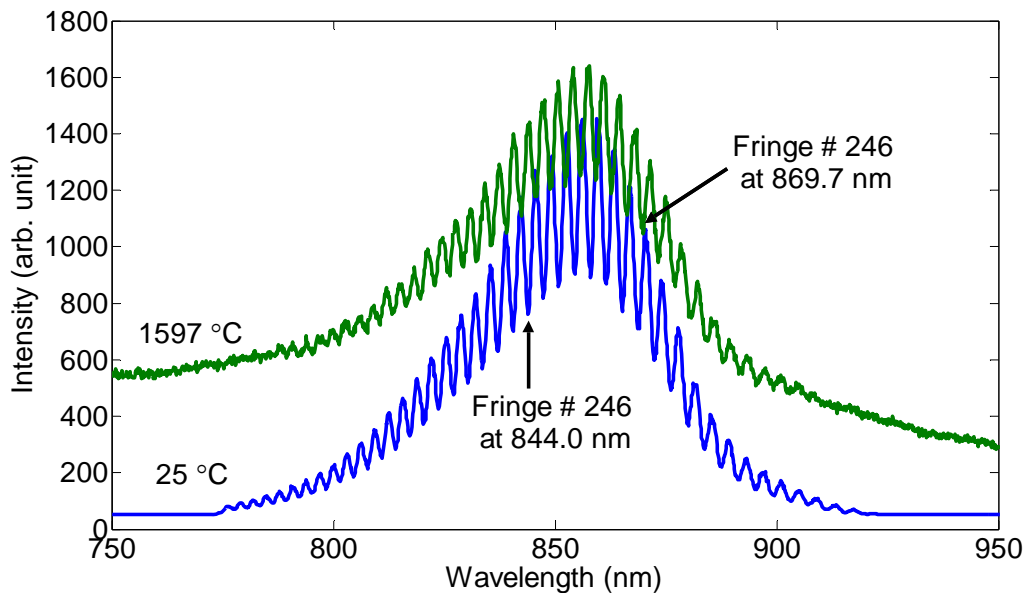


Figure 4-6. Sensor spectrum at different temperature

In Eq. (4-1), $I_B(\lambda)$, $I_D(\lambda)$ and $I_{LED}(\lambda)$ are all slow-varying compared to interference signal. Consequently, in the Fourier transform of the spectrum, Figure 4-7, all other terms will reside around zero frequency except the cosine term (interference signal),

$2V\sqrt{r_{s1}r_{s2}}I_{LED}(\lambda)\cos\frac{2n(T)d(T)}{\lambda}$, which can be filtered out following the signal processing approach discussed in Chapter 2.

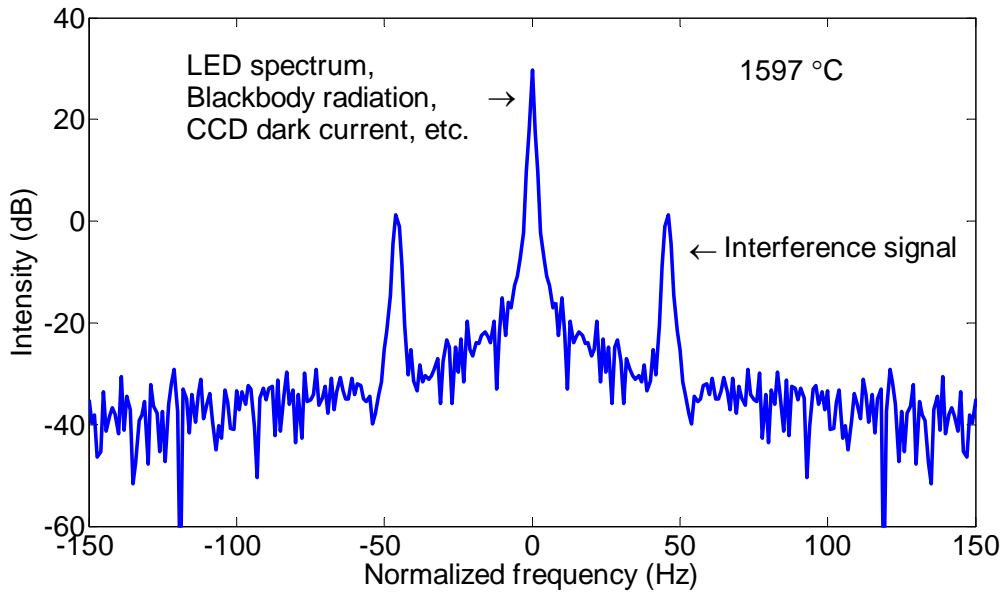


Figure 4-7. FFT of spectrum

Since we choose the thickness of the wafer to be relatively large, the cosine term locates far away from the $I_{LED}(\lambda)$ spectrum. They practically have no overlap. Therefore $2V\sqrt{r_{s1}r_{s2}}I_{LED}(\lambda)$ can be extracted by Hilbert transform and results only $\cos\frac{2n(T)d(T)}{\lambda}$, from which, the optical thickness (OT) of the sapphire wafer, $n(T)d(T)$, can be determined by fringe-tracing algorithm.

The OT and the spectrum vary with temperature as indicated in Figure 4-6, where the same valley (interference minima #248) moves from 844.0 nm at 25 °C to 869.7 nm at 1597 °C. The

relatively large cavity length greatly simplifies the signal processing in that it not only separates the interference spectrum from blackbody radiation and other irrelevant signals, but also makes it very easy to remove the LED profile.

4.4 Laboratory Test Results

For temperature tests, the sensor head, including 4cm-long sapphire fiber, was placed in to a furnace (DeITech, Inc.) along with a B-type thermocouple (Omega, Inc.) as reference.

In the test, the furnace was run from 230°C to 1600°C at a ramping rate of 3°C/min for three times. The change of optical thickness with respect to temperature by the B-type thermocouple is plotted in Figure 4-8. A 4th order polynomial was used to fit the data and convert each measured optical thickness of the wafer to a temperature. Figure 4-9 shows the measurement difference between the sensor and the thermocouple, which varies from -3°C to 3°C, corresponding to a ±0.2% full scale accuracy. This should be largely due to the measurement accuracy of the thermocouple, which has a specification of ±0.5% full scale over 800°C.

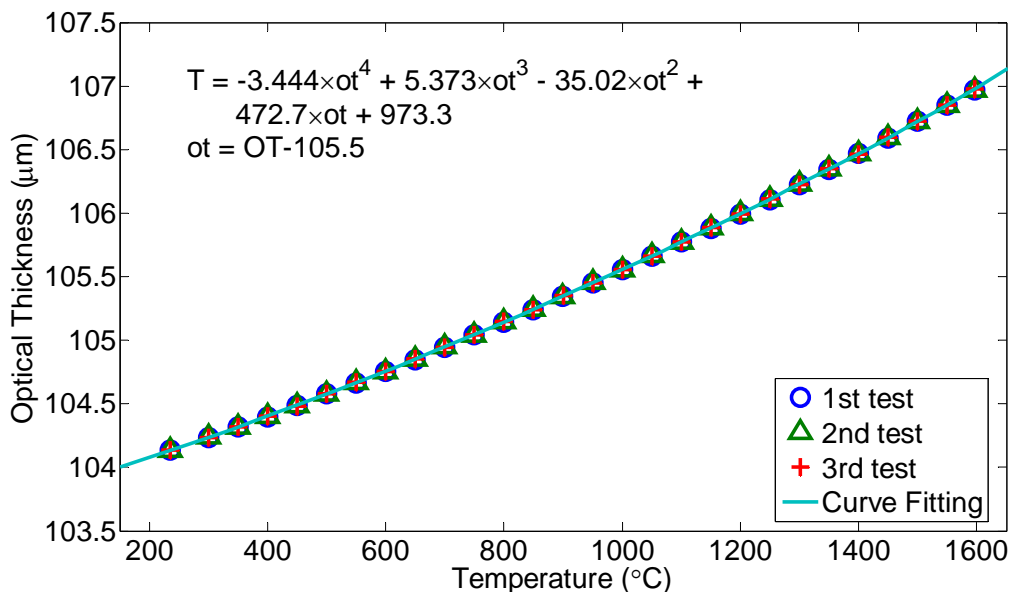


Figure 4-8. Optical thickness vs. temperature for three tests

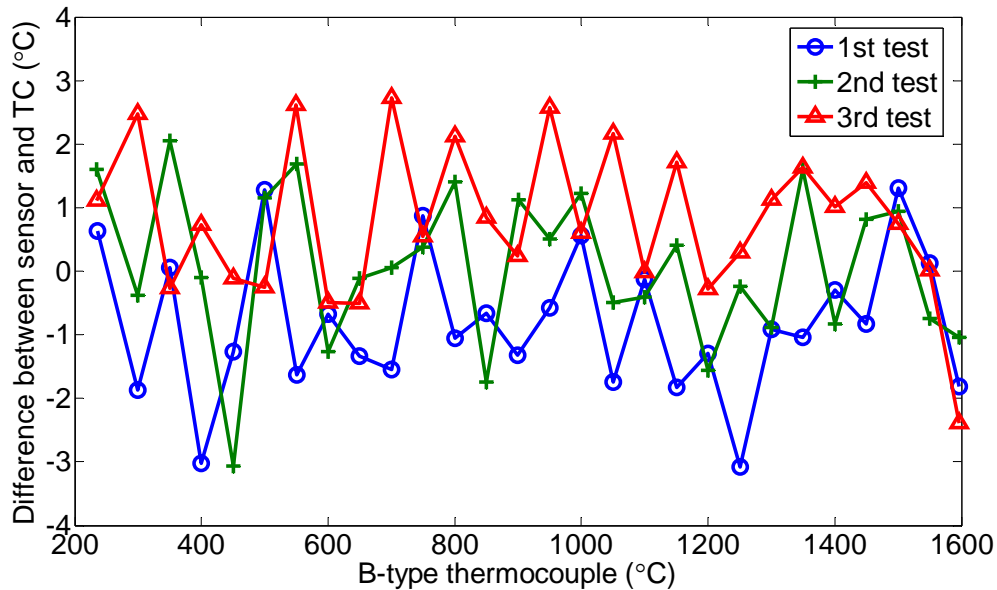


Figure 4-9. Temperature difference between sensor and thermocouple

4.5 First Field test results

In-lab tests have demonstrated the sensor’s excellent performance. To further explore its capability, it was selected for field tests at Polk Power Station of Tampa Electric, Corp (TECO), Florida. The station is a state-of-the-art integrated coal gasification combined-cycle (IGCC) power plant, producing 250-megawatt electricity for 75,000 homes. Built as next generation clean coal technology, the plant is able to remove more than 98 percent of the sulfur in coal and more than 90 percent of nitrogen oxide, enlisting it as one of the world’s cleanest. The heart of the plant is a coal gasifier where coal slurry and oxygen are mixed and burned to produce high-temperature high-pressure syngas for power generation. There has long been a need for temperature measurement inside the coal gasifier for operation monitoring and efficiency improvement.

The test goal is to install three properly packaged sensors in the coal gasifier at TECO, monitor them through white-light system and computer also placed on site, and remotely control the

system operation at Virginia Tech through internet. In the following sections, we will introduce the field test from system design, sensor fabrication, to installation and operation.

4.5.1 System Design

Figure 4-10 illustrated the system, which consists of three parts: a) Sensing probe and its housing, which are installed on the coal gasifier. b) Interrogation system, which contains all the optical components, including light source, detector and spectrometer, and is mounted near the probe. c) Signal processing unit, which includes a desktop computer and other communication electronics, and is placed inside a ground station. Part b) gets the optical signals from Part a) through fiber cables and then delivers to Part c) through communication cables upon computer's request.

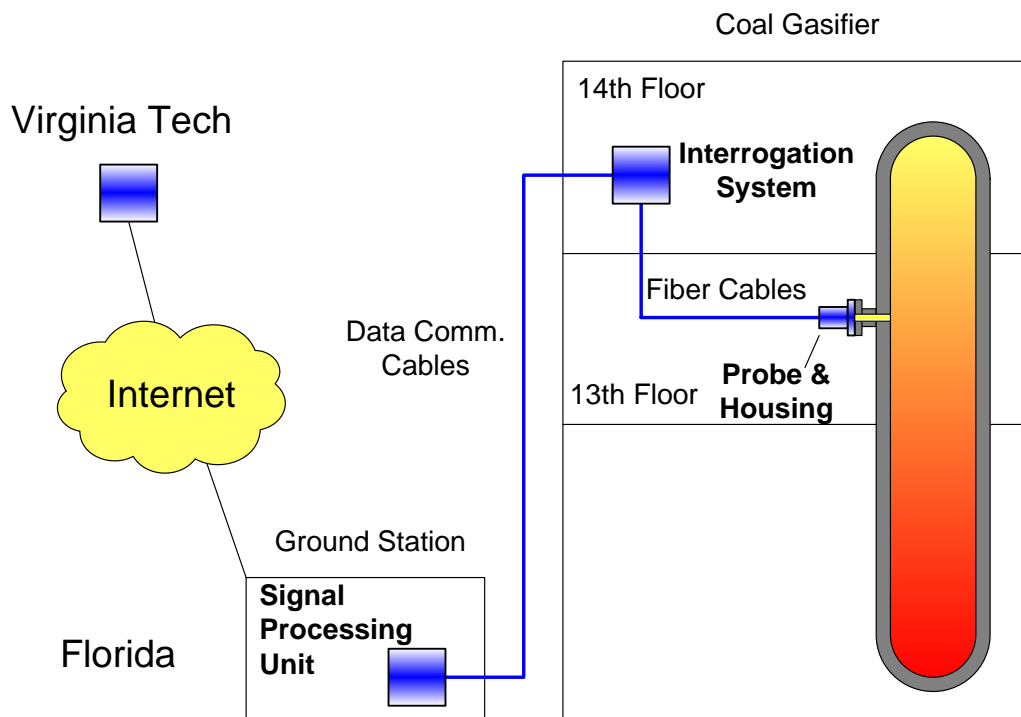


Figure 4-10. Design of coal gasifier temperature monitoring system

The probe consists of a series of alumina and sapphire tubes for sensor protection (See Figure 4-11). The innermost is a small alumina tube 1 with its sensor end close. Two sapphire tubes (2 and 3) were used for extra corrosion resistance. To prevent tube 3 from cracking due to thermal expansion induced stress, it is surrounded by a buffer of tightly stuffed high-temperature bulk fiber. Any stress from the outer tubes (4 and 5) will hence not transfer to inside, guaranteeing the sapphire tubes could properly protect the sensors. Between tubes 4 and 5, there is a section of dense refractory material at the sensor end, and all other space was stuffed with bulk fiber. When the probe assembly was completed, the sensors were loaded into it and fixed. The position of the first sensor is 2" to the end of the assembly. Each other sensor has a recess of 1 more inch to the first sensor.

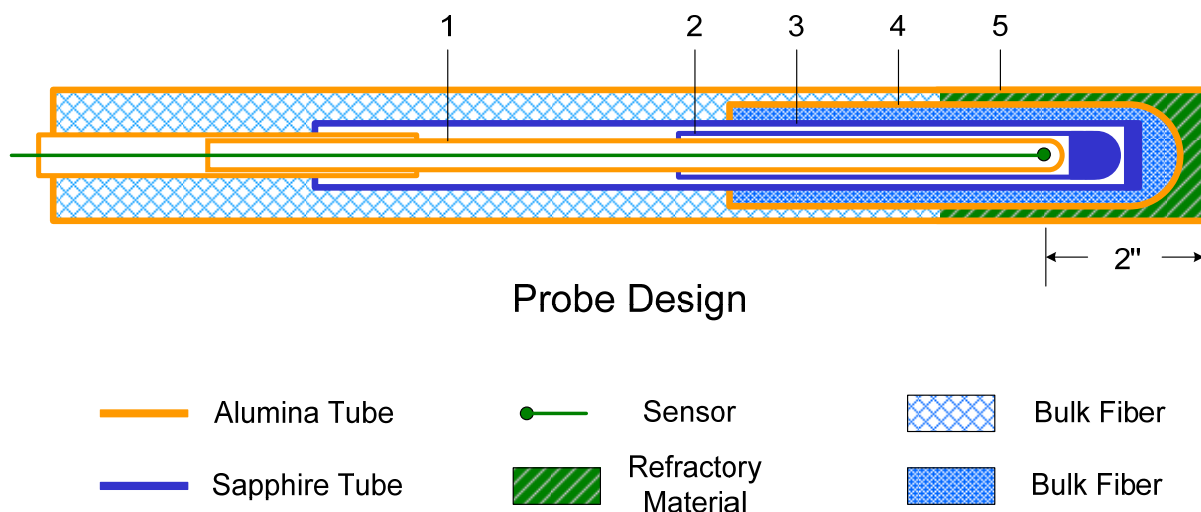


Figure 4-11. Schematic of sensing probe design

Figure 4-12 illustrates how the probe is mounted into the gasifier's refractory wall. Figure 4-13 show the three fabricated sensors and the laboratory test setup.

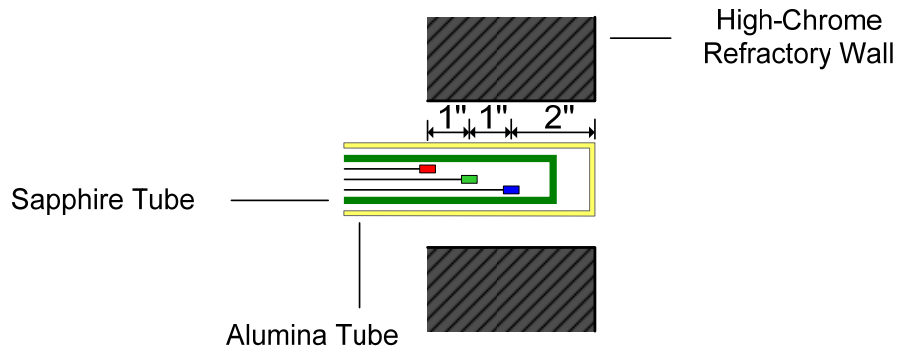


Figure 4-12. Probe mounting position

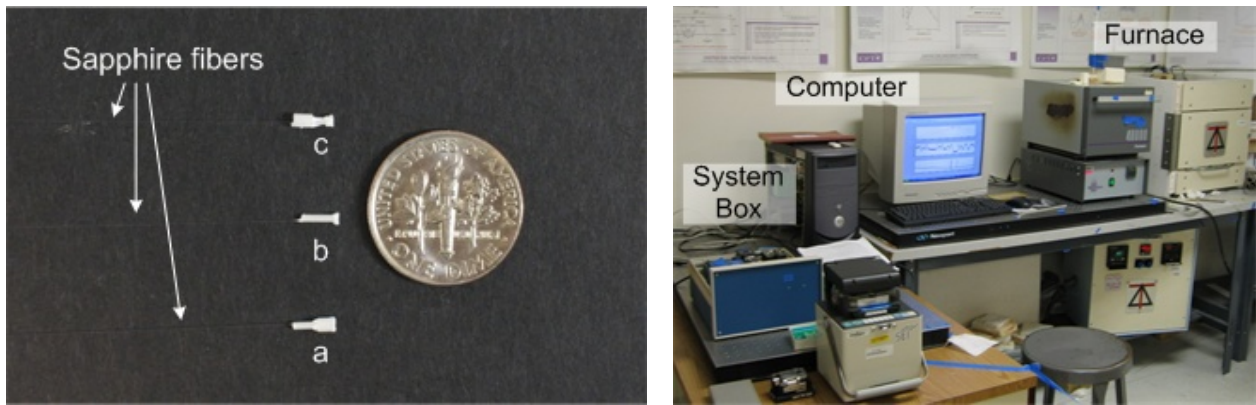


Figure 4-13. Left: photo of sensors; Right: sensor test setup

4.5.2 Calibration

Sensors were tested in high-temperature furnace for calibration, as in Figure 4-13. In the test, the sensors were put very close to each other, along with a B-type thermocouple, all within millimeters of distance. Therefore, the thermocouple reading will be the temperature of all sensors. Figure 4-14 plots the sensors' temperature responses, i.e., optical path difference (OPD) vs. temperature. It is evident that their OPDs are all different. In other words, the wafers have difference thickness.

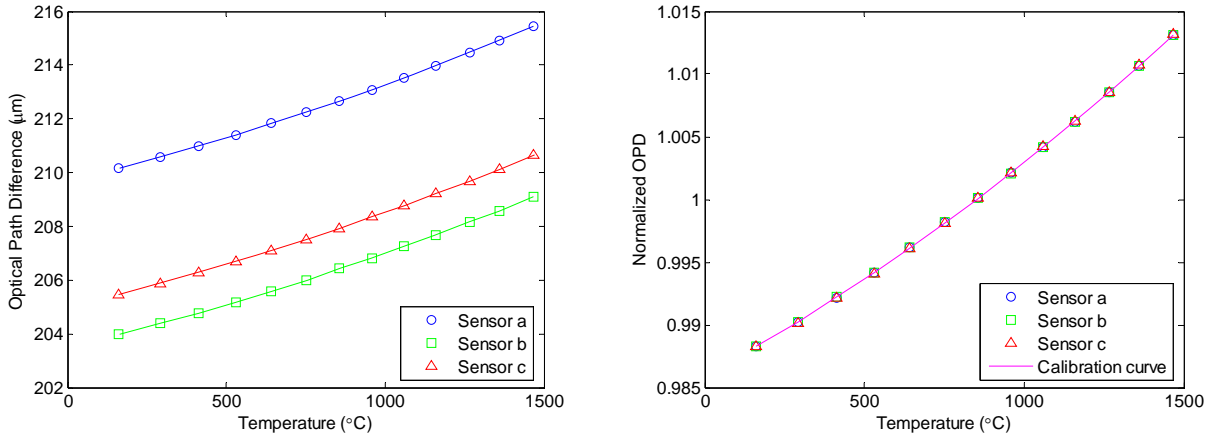


Figure 4-14. Temperature responses (left) and normalized temperature response (right)

In Figure 4-14 (left), the three temperature curves were normalized to their values at 850°C, producing almost overlapping data sets. This is expected and a major advantage of this sensing principle: all wafers, regardless of their thickness, will have the same normalized temperature response as long as their materials are the same. Therefore one curve works for all sensors. There is no need to calibrate each individual sensor.

This can be understood through the following equation.

$$\begin{aligned}
 OPD &= 2n(T)d(T) \\
 &= 2n_0F(T)d_0G(T) \\
 &= 2n_0d_0F(T)G(T) \\
 &= 2OPD_0F(T)G(T)
 \end{aligned} \tag{4-2}$$

where OPD is the optical path difference, n is the refractive index, d is the wafer thickness, T is temperature, n_0 and d_0 are n and d at a certain temperature. $G(T)$ is a function of temperature only and determines the thermal expansion of the material. Similarly, $F(T)$ control the thermal changes of refractive index. Therefore when normalized to OPD_0 , we have

$$\frac{OPD}{OPD_0} = F(T)G(T) \tag{4-3}$$

which is a curve dependent only on T. For our sensors, this calibration curve, shown in Figure 4-14, is fitted as

$$\frac{OPD}{OPD_0} = 1.54 \times 10^{-5} t^3 + 2.37 \times 10^{-3} t^2 + 1.64 \times 10^{-2} t + 1 \quad (4-4)$$

where $t = T/850 - 1$.

4.5.3 System Installation

The following photos show the three parts of the system after installation.

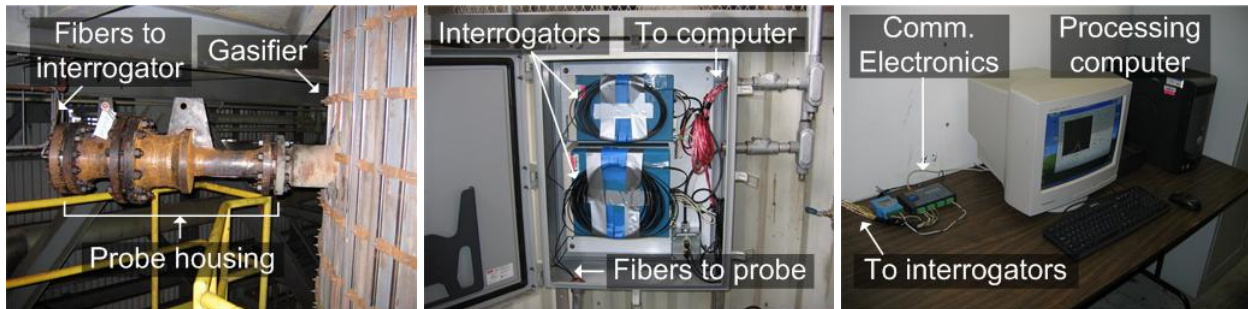


Figure 4-15. Installed probe and housing (left); optical interrogators (middle); and signal processing unit (right).

4.5.4 Results

The system ran for about seven months from the installation till the failure of the last sensor. The first two sensors lost signals in about week after the coal gasifier started up. The reasons of failure are to be analyzed after the probe is retrieved. In the following figure, the temperature curves recorded by the sensors are plotted together with those by the thermocouples. To protect the operating parameters as requested by TECO, the temperature curves are arbitrarily normalized and the dates are replaced by the number of days the system has been running.

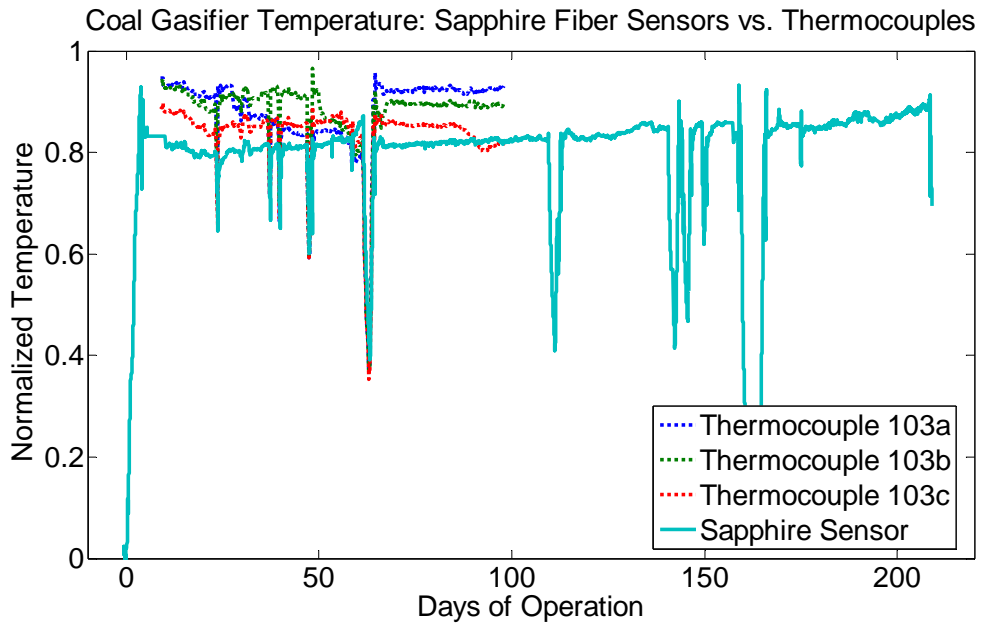


Figure 4-16. 72-day temperature results

4.6 Surface-mount sapphire-wafer-based temperature sensor

The sensing structure described in this chapter can be improved and simplified. This section introduces how this can be achieved by angle-polishing the sapphire fiber, as shown in Figure 4-17.

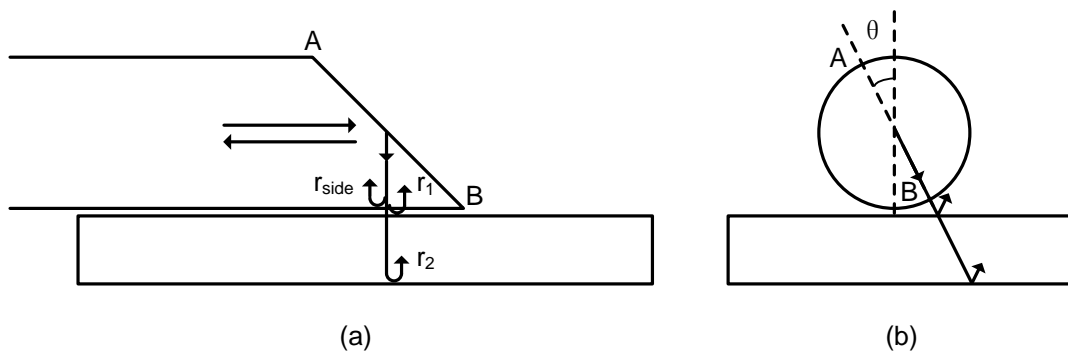


Figure 4-17. Sensor head structure

At 850nm, sapphire has refractive indices around 1.76 for both the o- and e-rays, translating to a 34.6° critical angle for total internal reflection. Different guided modes in the sapphire fiber have different incident angles at the polished surface, but all within a certain range around 45°. Given that 34.6° is far less than 45°, the majority of the incoming modes and energy is expected to be bent toward the wafer by the 45°-polished end. This is supported by experiments where visible light is injected into the sapphire fiber and at the polished end it can be observed that light is bent 90° by the polished surface and comes out of the fiber perpendicular to it with a certain divergence angle. From other directions, there is practically no light observed. Figure 4-18 shows a typical sensor spectrum at room temperature, whose interference is very clear as compared to that of a polished fiber end without the wafer.

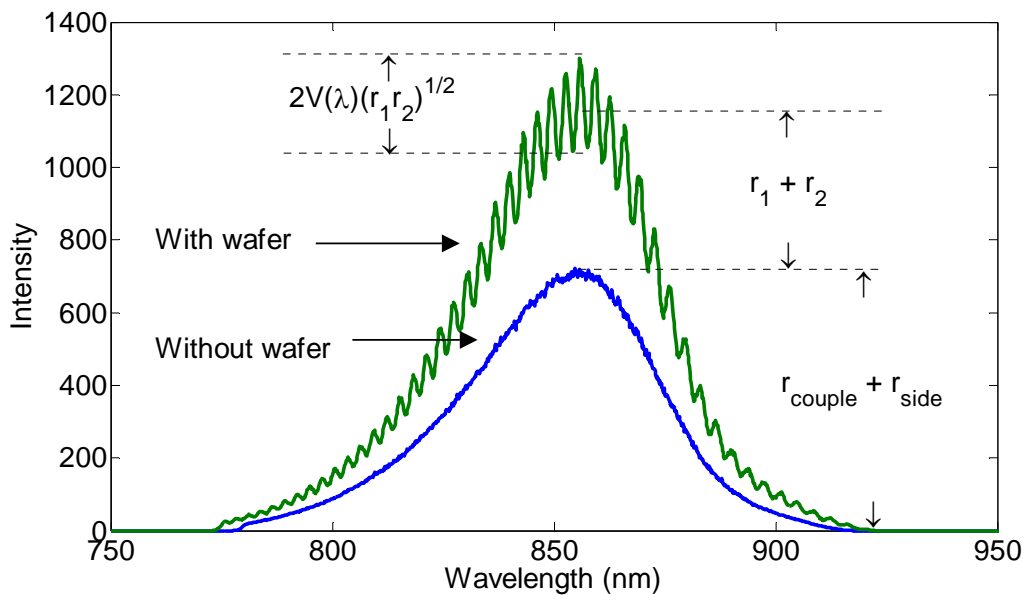


Figure 4-18. Sensor spectrum

Unlike most other fiber-optic sensors, this surface-mount structure aligns the fiber in the wafer plane, not only suitable for temperature measurement, but opening possibilities for other high temperature surface measurement such as strain as well.

The rest of the sensing system and the signal processing algorithm are the same as used for previously discussed sensor.

The sensor's temperature response was tested in a furnace (Thermolyne 48000, maximum temperature 1200°C) from 24°C to 1170°C. A S-type thermocouple is used for temperature reference. Figure 4-19 plots the change of optical thickness (open circles) with respect to temperature measured by the S-type thermocouple.

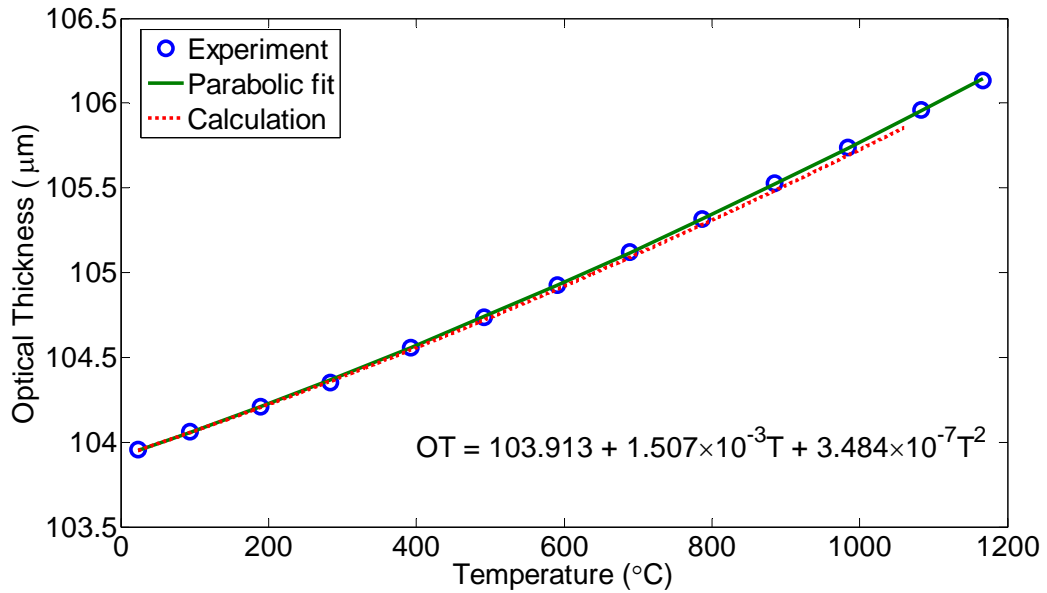


Figure 4-19. Temperature response

The data is fitted by a parabola as the following

$$\begin{aligned}
 OT &= n(T)d(T) \\
 &= 103.913 + 1.507 \times 10^{-3}T + 3.484 \times 10^{-7}T^2 \quad (\mu\text{m})
 \end{aligned}
 \tag{4-2}$$

and shown in Figure 4-19 (solid curve). Also plotted is the calculated temperature response (dotted line) from published data of sapphire's thermal expansion and its refractive index. The recommended values of C-axis thermal expansion of sapphire can be written as [7]

$$d(T) = (1 - 0.192 + 5.927 \times 10^{-4} T + 2.142 \times 10^{-7} T^2 - 2.207 \times 10^{-11} T^3) d_0 \quad (4-3)$$

where T is the absolute temperature in Kelvin, $d(T)$ is the thickness at T and d_0 is the initial thickness at 293 K (20 °C).

For the temperature dependence of the refractive index of the ordinary ray in sapphire, $n(T)$, Tapping *et. al.* has measured this value from 24 °C to 1060 °C for wavelengths of 633 nm and 799 nm,[8] as given by

$$n(T)_{633nm} = 1.76565 + 1.258 \times 10^{-5} T + 4.06 \times 10^{-9} T^2 \quad (4-4)$$

and

$$n(T)_{799nm} = 1.75991 + 1.229 \times 10^{-5} T + 3.10 \times 10^{-9} T^2 \quad (4-5)$$

where T is temperature in degree Celsius. By linear extrapolation from these two equations, a good estimation of $n(T)$ for 850 nm can be obtained as the following.

$$n(T)_{850nm} = 1.75815 + 1.220 \times 10^{-5} T + 2.81 \times 10^{-9} T^2 \quad (4-6)$$

Based on Eq.(4-3) and (4-6), a theoretical prediction of the optical thickness is given as the dotted line in Figure 4-19. The calculation shows a reasonable match to the experimental data.

Sensitivity

Eq. (4-2) indicates the optical thickness increases with temperature in the form of a convex function. Therefore the sensitivity of the sensor, defined as the slope of the temperature response curve, increases with temperature as well. From Eq. (4-2) the sensitivity S can be obtained as

$$\begin{aligned}
S &= \frac{d}{dT}[n(T)d(T)] \\
&= 1.507 \times 10^{-3} + 6.968 \times 10^{-7} T \quad (\mu\text{m}/^\circ\text{C})
\end{aligned}
\tag{4-7}$$

Therefore S increases with temperature from 1.524 nm/°C at 24°C to 2.322 nm/°C at 1170°C. Unlike the fluorescence-type sensor whose sensitivities can vary by orders of magnitude over large temperature range, the sensitivities of this sensor remain at similar level. Hence one can expect similar performance throughout the entire temperature range.

Resolution

The resolution of the sensor is the smallest temperature change the sensor could resolve. Even under the same temperature, the sensor output (optical thickness) would statistically fluctuate due to system noises. A temperature change is discernible only when it is larger than this fluctuation, to determine which, the sensor's optical thickness was recorded for 15 minutes at room temperature (24°C). Figure 4-20 shows the result and the statistical distribution. It is then determined that the standard deviation δ of these data is about 0.3 nm. Therefore the resolution of the sensor at room temperature is

$$\begin{aligned}
R_{RT} &= \frac{2\delta}{S_{RT}} \\
&= \frac{2 \times 0.3 \text{ nm}}{1.524 \text{ nm}/^\circ\text{C}} = 0.4 \text{ } ^\circ\text{C}
\end{aligned}
\tag{4-8}$$

where 2δ is taken as the smallest discernible temperature change. Better resolution can be achieved by taking spectrum average. Since S remains at similar level throughout the temperature range, R will remain at similar level as well. This means the sensor has more uniform performance over the entire temperature range and thus a larger dynamic range, as compared to fluorescence-based sensors.

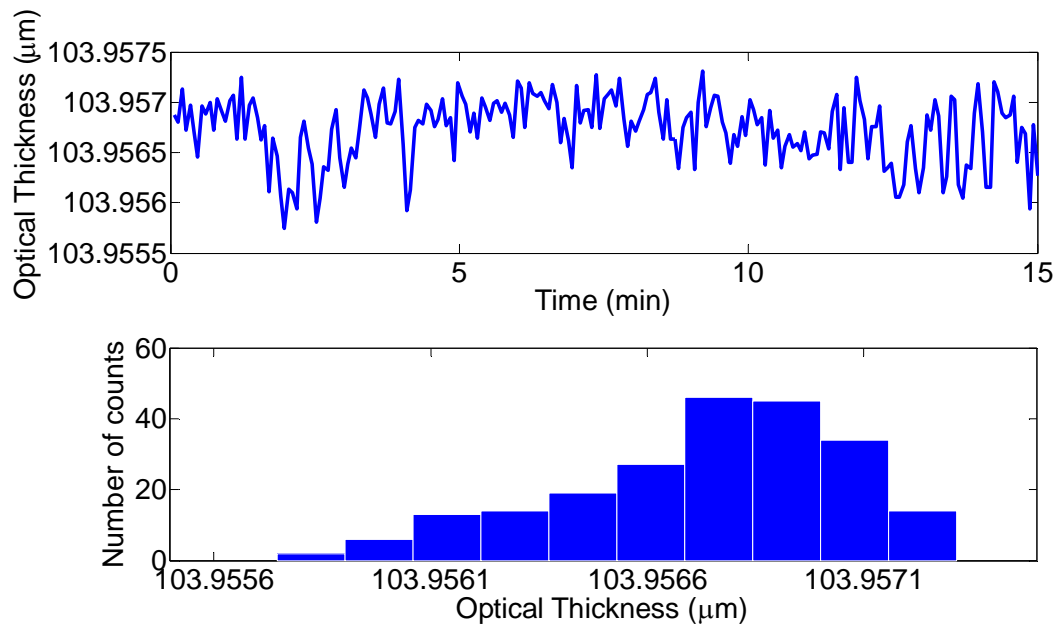


Figure 4-20. Sensor resolution at room temperature

4.7 Conclusion

This chapter discusses the design, fabrication and testing of a sapphire-wafer-based high-temperature sensor. Laboratory tests demonstrate its excellent high-temperature performance and field test further proved its reliability and robustness in a seven-month field operation. The results show the sensors are more reliable and stable than thermocouples. The sensor's other advantages, namely the ease of calibration and potential for mass production, were also demonstrated by experiments. Also, a surface-mount structure was proposed and demonstrated. It has similar performance but greater potential for further miniaturization.

4.8 References

- [1] A. Wang, S. Gollapudi, K. A. Murphey, R. G. May, and R. O. Claus, "Sapphire-fiber-based intrinsic Fabry-Perot interferometer," *Opt. Lett.* 17, 1021-1223 (1992)
- [2] R. E. Wagner, and C. R. Sandahl, "Interference effects in optical fiber connections," *Appl. Opt.* 21, 1381-1385 (1982)

- [3] F. Pérennès, P. C. Beard, and T. N. Mills, "Analysis of a low-finesse Fabry-Perot sensing interferometer illuminated by a multimode optical fiber", *Appl. Opt.* 38, 7026-7024 (1999)
- [4] A. Wang, S. Gollapudi, R. G. May, K. A. Murphey, and R. O. Claus, "Advances in sapphire-fiber-based intrinsic interferometric sensors," *Opt. Lett.* 17, 1544-1546 (1992)
- [5] R.K. Nubling, and J.A. Harrington, "Optical properties of single-crystal sapphire fibers," *Appl. Opt.* 36, 5934-5940 (1997).
- [6] G.N. Merberg, and J.A. Harrington, "Optical and mechanical properties of single-crystal sapphire optical fibers," *Appl. Opt.* 32, 3201-3209 (1993)
- [7] Y.S. Touloukian, R.K. Kirby, R.E. Taylor, and T.Y.R. Lee, *Thermophysical Properties of Matter, Vol. 13, Thermal Expansion Nonmetallic Solids* (Plenum, New York, 1977)
- [8] J. Tapping and M. L. Reilly, "Index of refraction of sapphire between 24 and 1060°C for wavelengths of 633 and 799 nm," *J. Opt. Soc. Am. A* 3, 610-616 (1986).

CHAPTER 5

Summary

In this research, we developed an all-fused silica fiber-tip pressure sensor and a sapphire-wafer-based temperature sensor. Besides their miniature sizes which rank them among the smallest in each category, both have been demonstrated with excellent response, reliability and robustness in laboratory tests and real-world applications. The pressure sensor was able to function beyond the current limit of pressure sensing technologies and operate into the 600~700 °C range. This was made possible by the development of fiber micro-machining processes. The temperature sensor can reliably operate for ultra-high temperature measurement as high as 1600 °C. This effort will provide more insights into sapphire fiber's high temperature properties and could possibly lead to novel designs of pressure sensor for beyond 1000 °C.

Based on this Ph.D. research, a series of publications have been generated, part of which is listed as follows:

- Y. Zhu, and A. Wang, "Surface-mount sapphire interferometric temperature sensor," ,” *Appl. Opt.* 45, 6071-6076, 2006
- X. Wang, J. Xu, Y. Zhu, K.L. Cooper, and A. Wang, "An all fused silica miniature optical fiber tip pressure sensor", *Opt. Lett.* 31, 885-887, 2006
- Y. Zhu, K.L. Cooper, G.R. Pickrell, and A. Wang, "Miniature fiber-tip pressure sensor for high-temperature applications," *J. Lightwave Technol.* 24, 861-869, 2006
- Y. Zhu, Z. Huang, F. Shen, and A. Wang, "Sapphire-fiber-based white-light interferometric sensor for high-temperature measurements," *Opt. Lett.* 30, 711-713, 2005

- Y. Zhu, and A. Wang, “Miniature fiber-optic pressure sensor,” *Photon. Technol. Lett.* 17, 447-449, 2005
- Y. Zhu, G.R. Pickrell, X. Wang, J. Xu, B. Yu, M. Han, K.L. Cooper, A. Wang, A. Ringshia, and W. Ng, “Miniature fiber-optic pressure sensor for turbine engine,” in *Proc. SPIE Sensors for Harsh Environments*, vol. 5590, pp. 11-18, 2004.
- Y. Zhu, Z. Huang, M. Han, F. Shen, G.R. Pickrell, and A. Wang, “Fiber-optic high-temperature thermometer using sapphire fiber,” in *Proc. SPIE Sensors for Harsh Environments*, vol. 5590, pp. 19-26, 2004.

Related issued or pending patents are as follows:

- Y. Zhu, X. Wang, J. Xu, and A. Wang, “Optical fiber pressure and acceleration sensor fabricated on a fiber endface,” U.S. patent No. 7,054,011, issued on May 30, 2006
- International PCT patent, application No. PCT/US2004/028535, pending
- Y. Zhu, and A. Wang, “Method for low-loss adhesive-free coupling between silica fiber and sapphire fiber,” US provisional patent application No. 60/836,127, pending
- Y. Zhu, and A. Wang, “A fiber-optic interferometric sensor for high-temperature applications,” US provisional patent application No. 60/836,128, pending